University of Nottingham
UK | CHINA | MALAYSIA

Understanding high redshift Active Galactic Nuclei activity through infrared variability

Karel A. Green

REDACTED

Thesis submitted to the University of Nottingham
for the degree of Doctor of Philosophy

September 2024

Leaving the quote as surprise >:D

– –

Supervisors:	Prof. Omar Almaini	
	Prof. Michael Merrifield	
Examiners:	Prof. Andrew Lawrence	(University of Edinburgh)
	Prof. Alfonso Aragón-Salamanca	(University of Nottingham)
Submitted:	30 September 2024	
Examined:	TBD	
Final version:	????	

Contents

Abstract

Abstract

Acknowledgements

I’ll leave this as a surprise :D

Equality Diversity and Inclusion

Published works

Material presented in this thesis has already been published in — or is in preparation for submission to — a journal as the following works:

I **Green K.**, Elmer, E., Maltby, D., Almaini, O., Merrifield, Hartley W. G., 2024, MNRAS, 531, 2: *'Increasing AGN sample completeness using long-term near-infrared variability'*.

II **Green K.**, Elmer, E., Maltby, D., Almaini, O., Merrifield, Hartley W. G., 2024, MNRAS, in preparation: *'Investigating the origin of infrared variability in AGN'*.

The vast majority of work presented here was carried out by the author, with advice from the paper authors above. Where the work contains the product of larger collaborations, this is mentioned in the relevant chapter.

Chapter 1

Introduction

1.1 Extragalactic Astronomy

The general goal of astrophysical research is to understand how the Universe evolved into what we see today. Though it is now well understood that the Milky Way is just one of many galaxies in the Universe, the fact that other galaxies exist was a major scientific breakthrough in of itself. One of the earliest recorded observations of galaxies beyond the Milky Way can be seen in the *'Book of fixed stars'* by Iranian Astronomer Abū al-Ḥusaīn al-Ṣūfī in 964AD. Here the Andromeda galaxy was identified, and it was noted that it had a smeared appearance, which was unlike other celestial bodies in the sky (Hafez, 2010). These bodies largely remained a mystery until the philosopher Immanuel Kant presented the idea of "island universes", meaning other galaxies, as an explanation for the observed "nebulae of unknown nature". This theory of other galaxies was a major argument in the *'Great Debate'* (Curtis, 1988) and was finally confirmed by the early 20^{th} century, when Hubble measured the distance to one such spiral nebulae and proved it was truly extragalactic in nature (Hubble, 1925). This confirmation that objects exist beyond the edge of the Milky Way opened up the extragalactic research field, as the nature of these objects would need to be understood before new models of the Universe could be suggested.

As the number of galactic surveys increased, it was quickly found that galaxies have a range of properties. Edwin Hubble classify these galaxies based on their visual morphology in increasing complexity, and this resulted in the first iteration of the Hubble sequence (Hubble, 1926). This sequence was then completed by Allan Sandage after Hubble's death (Sandage, 1961), which built the Hubble Tuning Fork classification scheme that is popular today (Figure1.1). Beyond morphology, measurements of extragalactic spectra found that spectral lines were shifted compared to galaxies are not static, but have a velocity relative to the Milky Way. The radial velocity was of Andromeda was first measured by Slipher 1913, who used the blueshift of the galaxy's spectrum to calculate the speed of approach. This idea was then extended in Hubble 1929 where it was noticed that the more distant a galaxy, the faster its speed of recession. This marked the development of Hubble's law as well as providing empirical evidence for the expanding Universe theory.

Amongst these discoveries, it is important to note that a class of galaxies with peculiar visual and spectral features were observed. These galaxies are now known as 'active

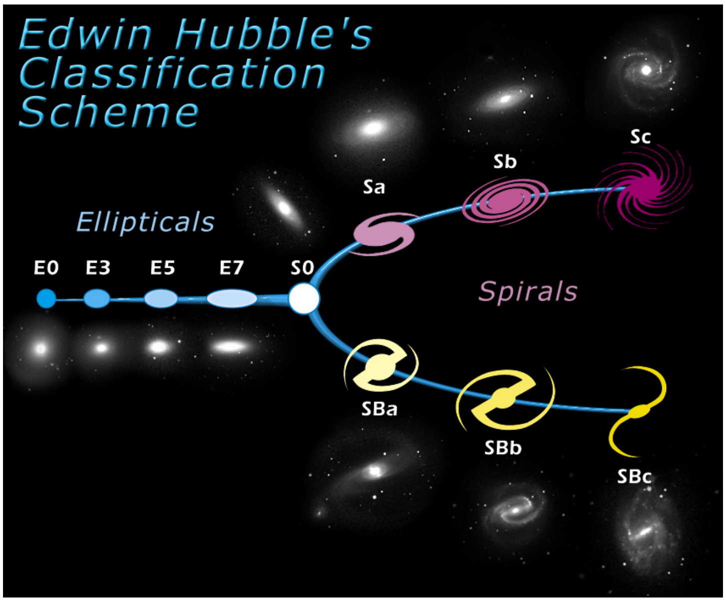

Figure 1.1: The Hubble sequence as devised by Hubble 1926 and updated by Sandage 1961. Image taken from information@eso.org (1999). Galaxies are ordered according to their visual complexity, progressing from elliptically (left) to lenticulars in the centre. Spiral galaxies form the right of the diagram, with barred-spirals on the bottom and non-barred, "normal", spirals at the top.

galaxies' and it is this galaxy group we explore in the following section.

1.2 Galaxies

In order to understand the active galaxies, we must first explore the general features of galaxies. In modern astrophysics, galaxies are generally recognised to be structures where a collection of matter is bound in orbit to a supermassive black hole (SMBH). As discussed in Section 1.1, there galaxies can have a range of properties, however it is believed that most, if not all galaxies contain a supermassive black hole (SMBH) in the centre. Many relations have been reported between black holes and the properties of the host galaxy that implies the formation and evolution of the two are heavily linked, and active galaxies are no exception to this. The accretion of matter onto a black hole is the current leading theory for the emission observed from active galaxies and as such understanding black holes is required to understand active galaxies in general.

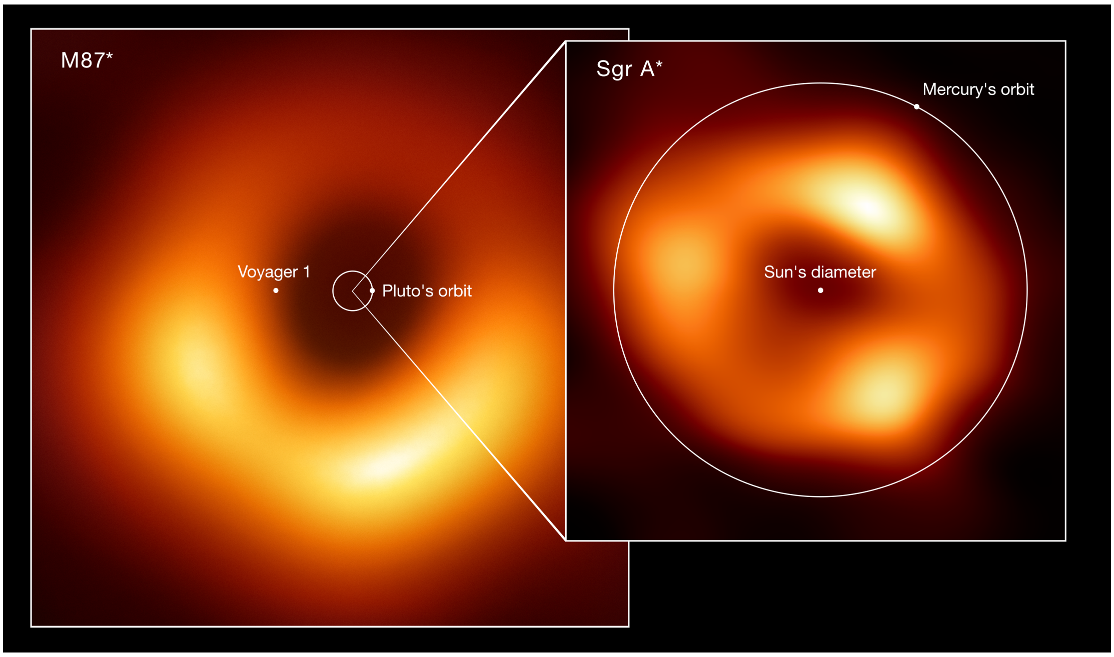

Figure 1.2: Image of the event horizon about the black hole in the galaxy Messier 87 (left) as well as the event horizon of Sagittarius A* (right). Various properties of Solar System objects are shown on the images to illustrate the relative scales of the black holes (Collaboration et al. 2019; Collaboration et al. 2022).

1.2.1 Black Holes

Black holes are defined as regions of spacetime so dense that nothing, not even light, can escape. A simplistic model places a singularity - a point of infinite density and zero volume - at the centre of the black hole, and the Schwarzschild radius defines the region around it where information cannot escape. The idea of black holes can be seen as early as Michell 1997, who used Newtonian physics to show that, if a star was dense enough, it's escape velocity would be greater than the speed of light. Though the idea of massive, invisible stars is an exciting theory, the interest in this did not last, as the wave-like properties of light were discovered and it's assumed-zero mass lead scientists to believe it would be largely unaffected by gravity.

The concept of black holes became relevant again in the early 20^{th} century when Einstein developed his theory of general relativity (GR; Einstein 1916, eng. translation: Einstein et al. 1920). His field equations described gravity as a bending of space-time which could therefore impact light, and Schwarzschild quickly discovered a solution to these equations defining the a region from a singularity where light could not escape

(Schwarzschild 1916, eng. translation: Schwarzschild 1999). The exact nature of the resulting surface formed by the Schwarzschild radius remained a mystery until 1958, where physicist David Fienkelstein described it as 'a perfect unidirectional membrane' where influences could only pass beyond the surface in one direction, indicating that particles could not escape it (Finkelstein, 1958). The edge of space, just beyond the Schwarzschild radius, is now known as the black hole event horizon (Rindler, 1956) and this is the closest one can get to observing a black hole directly. As such, it is the interaction of gravitationally bound matter as well as the bending of light that allows for the study of black holes.

Outside of theory predictions, there is a wealth of evidence for the existence for black holes including:

1. The X-ray binary system Cygnus X-1 is one of the brightest and well studied X-ray sources in the night sky (Webster & Murdin, 1972). Here, the mass of the non-stellar source has been estimated to be on the order of $10M_{\odot}$, well above the upper limit for a neutron star. From this it is widely believed that the binary pair is comprised of a black hole and a star (Herrero et al., 1995).

2. Measurements of the proper motion of stars about the galactic centre of the Milky Way was used to estimate the mass of Sagittarius A^* in Ghez et al. 1998 and Genzel et al. 2010. Based on mass and radius estimates, the authors concluded that Sagittarius A^* is a black hole.

3. In September 2015, gravitational waves were detected at the Laser Interferometer Gravitational-wave Observatory (LIGO). It was concluded that the waves originated from a merger of a pair of black holes, as the measured shape matched the GR prediction for such an event (LIGO Scientific Collaboration and Virgo Collaboration et al., 2016).

4. One of the most recent and compelling arguments for the existence of black holes comes from the images of multiple black hole event horizons. The first image released was of the event horizon for the black hole in active galaxy Messier 87 (M87). The second ever image of an event horizon was taken of Sagittarius A^*, the black hole in the centre of the Milky Way. These are pictured in Figure 1.2 (Collaboration et al. 2019, Collaboration et al. 2022).

5. Finally, in the following sections we detail the discovery and structure of active galaxies. Active galaxies are distinguished from inactive or "regular" galaxies by the presence of an active galactic nuclei (AGN). AGN are thought to be powered by black hole accretion which results in the observed coherent changes in flux across the electromagnetic spectrum. The existence of AGN, and more specifically the observed variability in their emission, is arguably the most convincing evidence for the existence of black holes as outside of black hole accretion, it is difficult to reproduce this observed feature (Rees 1984; Green et al. 1993).

Having explored black holes as a key feature of galaxies, we now return to the specifics of active galaxies.

1.3 Active Galaxies

1.3.1 Discovery of Active Galactic Nuclei

Active galaxies are galaxies that host an active galactic nucleus (AGN). Active galaxies are extremely powerful systems, being one of the few objects to emit across the entire electromagnetic spectrum (e.g., Edelson & Malkan 1987; Collier & Peterson 2001; Cackett et al. 2021), and the central AGN engine is believed to be powered by accretion onto a supper massive black hole (Salpeter 1964; Kormendy & Richstone 1995).

As previously stated, AGN emission causes active galaxies have different visual and spectral features compared to an inactive galaxy. For this reason, though it was not know, AGN emission has been observed as early as the beginning of the 20^{th} century. In Fath 1909, 'spiral nebulae' were being observed to determine if their spectra was truly continuous, as commonly claimed at the time. Amongst the objects studied, NGC 1068 stood out, as it showed both absorption and emission lines compared to other objects which had little to no emission lines in their spectra. Similarly, in measuring the spectrum of NGC 1275, Humason 1932 noted that the nuclear component of the galaxy appeared near-stellar compared to other objects that did not show excess light in the centre. Finally, Seyfert produced his now seminal paper, Seyfert 1943, where he measured the properties of a unique class of objects that would eventually be known as "Seyfert galaxies". He noted that, in agreement with Humason 1932, the nucleus of these galaxies appear bright and point-like, but also showed unique spectral properties, having broad emission lines with the width of seemingly correlating with the luminosity of the nucleus as well as the nuclear-to-host light ratio. These studies formed the early history of AGN discovery and proved that active galaxies formed a different group of galaxy compared to inactive galaxies in the Universe.

Completing the history of the AGN observational timeline, it was only with the discovery of high energy, radio-loud quasars that the historical measurements of active galaxies were popularised and AGN physics became a real area of interest. In Baade & Minkowski 1954, discussion of discrete radio sources found that the spectrum of Cygnus A, a radio-loud galaxy, to be similar to the spectrum of NGC 1275, one of the six original Seyfert galaxies. Following this, Schmidt 1963 identified the radio-loud active galaxy 3C 273. The authors state that 3C 273 is extragalactic in nature, and appears as a star-like nucleus with a radio jet outflow and as more of these extra-galactic 'quasi-stellar' radio sources were identified, they were given the name 'quasars' in the literature. Over time, it was realised that quasars and Seyfert galaxies are likely the same type of object emitting at different energy ranges, and in generalising these objects the active galaxy theory was formed, with Seyferts and quasars forming specific sub-classes of active galaxies.

1.3.2 AGN and the evolution of the Universe

Beyond understanding how they work, active galactic nuclei activity has been used as a key component in describing the evolution of the Universe.

In the early universe it is believed that AGN activity drove helium reionisation. The epoch of reionisation beings when the first stars (population III stars) produce photos that are energetic enough to ionise neutral hydrogen in the Universe (Dayal et al., 2020). Though population III stars are largely thought to drive the earliest emission in the Universe, active galactic nuclei activity is credited as being the main driver of the subsequent ionisation of Helium (Volonteri & Gnedin 2009; Eide et al. 2020).

The effects of AGN emissions can also be see in large scale structure within the Universe. In galaxy clusters, the brightest cluster galaxy is more likely to be a radio loud AGN than an inactive galaxy at the same stellar mass. This forms an important observation as the feedback from the radio jets from such galaxies is the current most accepted solution to the cooling flow problem observed in galaxy clusters (Best et al., 2007).

Outside of the solutions AGN emission poses to structures within the Universe, there have been many observations between the properties of black holes the properties of the galaxies they exist in, implying the evolution of the two are linked despite the different physical scales they exist on.

The first is the known Mbh-Mbulge - observations

AGN accretion - SFR history - observations

Mph-sigmabulge - observations

1.3.3 AGN structure

Having described the historical observations of AGN, we now address modern views of the underlying structure and emission from active galaxies.

In the contemporary view, an AGN consist of a black hole that is actively accreting material from its surroundings (Alloin et al., 2006). From the central black hole outwards, the accreting material takes the form of an accretion disk and surrounding both the disk and black hole is an electron plasma moving at relativistic speeds. Beyond this electron corona are clouds of gas bound to the system, which produce broad and narrow emission lines depending on their proximity to the black hole, and at the edges of the system there is a surrounding dusty, torus-like object that feeds into the accretion disk. The final component is a pair of relativistic jets, anti-parallel to each other, however these are only observed in $\sim$10% of AGN. A diagram of an AGN system can be seen in Figure 1.3.

In addition to the physical structure of the system, one of the defining observational features of AGN is their broad-band radiation. The flux from inactive galaxies is dominated by stellar emission, and as such the spectra of these galaxies typically consists of a superposition of blackbody spectra, over a relatively narrow wavelength range. AGN, on the other hand, have a range of distinct observational features (Dermer & Giebels 2016; Padovani et al. 2017) and are one of the few known objects to have been observed in every waveband in the electromagnetic spectrum (See Figure 1.4). Though

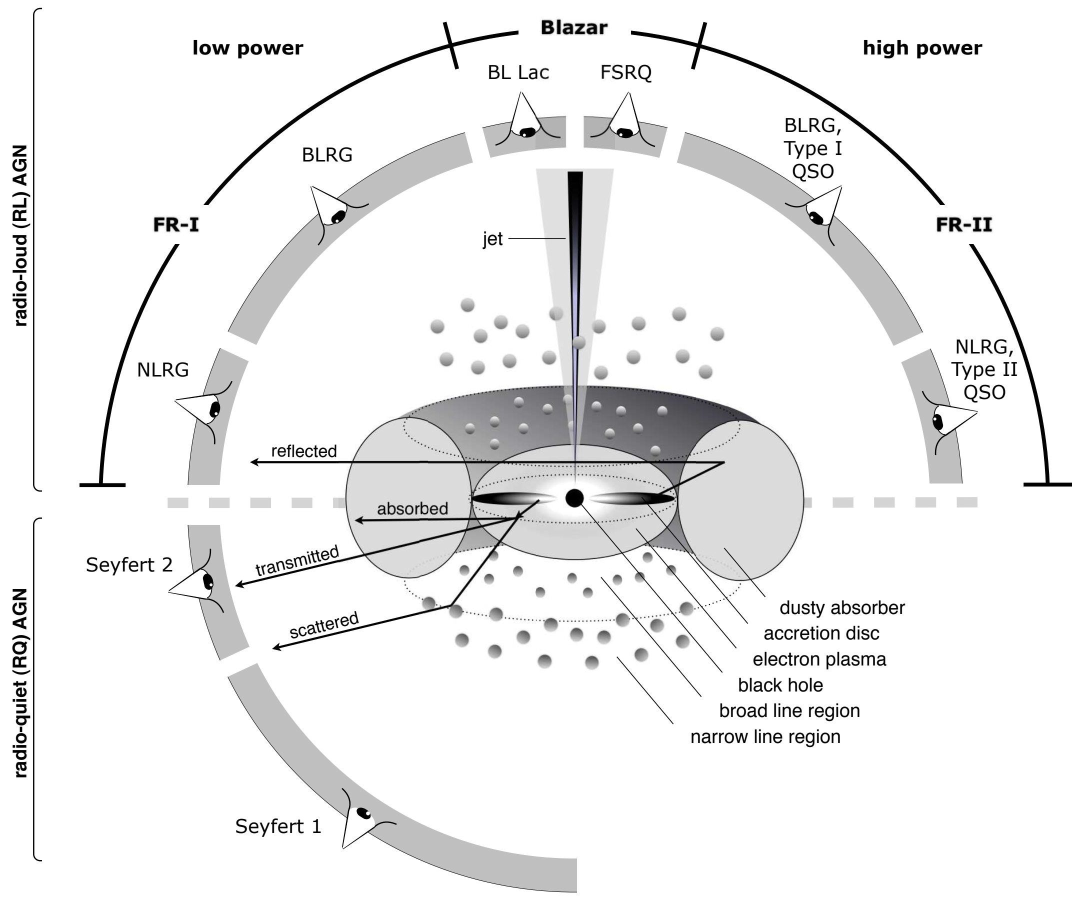

Figure 1.3: Diagram of the main components of an AGN, taken from Beckmann & Shrader (2013). Note that jets in radio-loud AGN are thought to be symmetric and the true shape of the dusty absorber is not confirmed to be a perfect torus.

the processes that drive multi-wavelength AGN emission is still not fully understood, Antonucci 1993 provided the current leading model for AGN structure and emission. This unified model states that all AGN are driven by the same black hole accretion process, however the observed differences in AGN types is due to different viewing angles between a given active galaxy and the observer. This theory suggests plausible structures for the nuclear regions of an active galaxy as well as reproduces broadband AGN emission.

Connecting components of an AGN to the radiation produced, the bulk of AGN emission is attributed to the accretion disk (Salpeter, 1964). Here, surrounding matter falls towards the central supermassive black hole and this matter takes the form of an optically thick

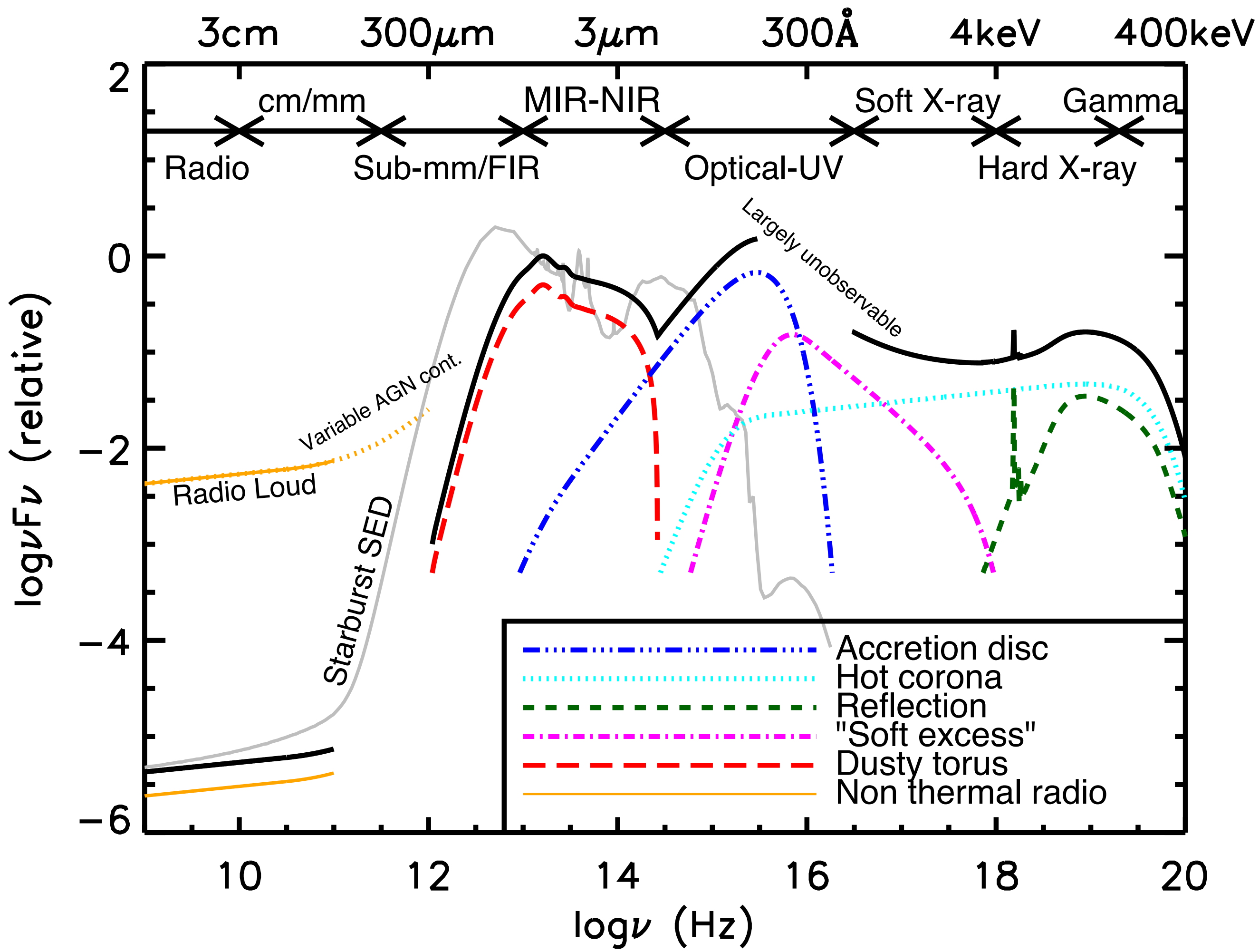

Figure 1.4: An AGN spectral energy distribution (SED), taken from Harrison 2014 and Hickox & Alexander 2018. Here the black solid line shows the overall emission and the coloured curves show individual components. The coloured curves have been offset from the total-emission curve for clarity.

(light is readily absorbed) but geometrically thin (small width or thin in the vertical direction) disk. The accretion disk is viscous enough that the differential rotation of the material induces shearing at adjacent radii. Angular momentum and gravitational energy is converted into electromagnetic (EM) radiation as well as kinetic energy, and the heated matter is blown out as accretion disk as "winds". The EM radiation of disk is typically in the optical/UV frequency range, and this forms the "big blue bump" of the AGN SED (Netzer 2013; Panagiotou et al. 2022).

Following from the accretion disk, optical and UV photons travel to the electron plasma, and are inverse Compton scattered to X-ray wavelengths. This interaction produces X-ray radiation and forms the X-ray corona of the AGN. Moving further out the system, the broad line region (BLR) is reached. Here clouds of gas are bound to the black hole and orbit at extremely high speeds. As such, any emission lines from this region is widened due to Doppler broadening, and the production of these broad-emission-lines gives the region its name. Further out from the BLR is the narrow line region (NLR). Also comprised of clouds of gas, these clouds exist at a lower density and orbit at a higher radius from the black hole. Their lower orbital speed leads to little or no broadening of the emitted radiation from these clouds, resulting in standard emission lines at specific wavelengths.

The edges of the AGN system is formed by a surrounding dusty obscurer/absorber. The specific shape of this object is still up for debate, as it is unlikely to be a perfectly smooth and rounded torus, however it is likely to exist in a ring around the accretion disk. This dusty object, referred to from now as the dusty torus, is comprised of dust that is heated by the nuclear-produced photons of the accretion disk, which is then absorbed and reprocessed into the infrared (IR).

About 10% of AGN are observed to be radio-loud, and in these cases the AGN are thought to have a pair of anti-parallel, relativistic jets that also serve as an explanation for gamma-ray emission in the galaxy. Radio emission originates from the synchrotron process within the jets, where relativistic electrons radiate EM radiation in the form of radio waves as they accelerate through a magnetic field. Jet activity also gives rise to gamma ray production in AGN, as "seed" photons from the accretion disk, dusty torus, BLR and NLR clouds or the synchrotron emission in the jet itself is inverse Compton scattered to gamma ray wavelengths by the jet-bound electrons (Madejski & Sikora, 2016).

Finally, to conclude this section we revisit the AGN unification theory (Antonucci, 1993), where it is stated that all types of AGN have effectively the same structure, but the viewing angle, presence of jets, as well as the power of the AGN itself determines the type of active galaxy that is ultimately observed. In type I active galaxies, the AGN is viewed from the "top-down" such that the dusty torus does not intervene between the observer and all AGN emission is unobscured. In contrast to this, type II active galaxies are viewed "through" the dusty torus, and as such areas closer to the core such as the broad line region are not observable, leading to only the narrow lines of these objects to be measurable.

The multiple processes within the unified theory of AGN emission interconnect to reproduce the wide range of wavelengths observed from the objects, but in addition to this the mechanisms are flexible enough to allow for variability in the radiation. Irregularity in flux is a quality that is intrinsic to AGN emission and it is this characteristic that is described in Section 1.4.

1.3.4 AGN detection methods

1.4 Variability

A key feature of the broad-band emission from AGN is that it is not static, but varies in flux in every wavelength in which it has been observed (e.g., Fitch et al. 1967; Sánchez et al. 2017). This variability has been studied in detail since their discovery (e.g., Smith & Hoffleit 1963), and has been found to be aperiodic in nature. Hypotheses into the origin of variability point to stochastic processes within the AGN itself, with UV and optical variability originating from instabilities in the accretion disk, which has a knock on effect causing irregularities in the X-ray output of the corona as well as IR emission in the dusty torus. Variability in radio and gamma-rays however, likely arise from jet-related processes as well as uneven seed photons production from the accretion disk (Netzer 2013; Bianchi et al. 2022).

Despite the high power output and range of emission wavelengths AGN produce, the small physical size of an active galaxy's central engine means that accretion and emission occurs on scales many orders of magnitude smaller than that of the host galaxy.

Consequently, resolving the central nucleus is simply not feasible for galaxies outside our local neighbourhood (e.g., Padovani et al. 2017) making AGN difficult to study. The difficulty in unpicking AGN emission from that of its host galaxy also poses a significant barrier in understanding the structures present within an AGN, and the impacts of the accretion process on the surrounding region (Grogin et al. 2005; Gabor et al. 2009; Pierce et al. 2010; Fan et al. 2014). As such, AGN variability is an important tool in the study of active galaxies, as variability observations are limited by light-travel times, allowing for small scales to be indirectly probed.

Since the speed of light in a vacuum is a known physical quantity, the timescale that AGN variability takes place on can be used to characterise the emitting region of the system. Such variability studies have produce key pieces of evidence for AGN emission theories, such as mass and radius estimates favouring black holes over other object as the nuclear body in the emission process (Green et al., 1993). Variability timescales have also been found to increase with wavelength, for example, emission at higher frequencies, such as X-rays, vary within hours, while UV and optical variations take days to weeks. The longer wavelengths, such as infrared (IR), typically vary on timescales of months or years (e.g., Berk et al. 2004). Since this variability is coupled to structures within the AGN itself, it allows for the study of AGN on the relatively tiny scales they span compared to the size of a galaxy.

Infrared variability is uniquely useful in the study of AGN, as IR measurements probe the dusty torus-like structure on the edges of the AGN system as material from it feeds the accretion disk as well as being able to probe dusty galaxies and rest-frame optical emission for galaxies at higher redshift. Unfortunately, the timescale of variability in the IR is several months to years, and this time cost has limited the research in this regime compared to variability in higher frequency wavebands. The Ultra Deep Survey (UDS, Chapter 2), however, provides a solution to the obstacles preventing IR variability studies, as it has 8 years of deep, near-IR imaging. The $\sim 1\text{deg}^2$ imaging has collected the time-intensive data required for significant IR variability to be observed and these deep observations provide the perfect dataset for the study of infrared variability in active galaxies.

AGN emission is invoked across many aspects of galaxy evolution to help explain observed phenomena, but this activity, and the underlying mechanisms that drive it, is still not fully understood. As a result, despite many theories within the literature, there is no firm consensus on the potential trigger (or triggers) that activates an AGN. Furthermore, we are currently unable to observe any given galaxy and know with certainty how and why it is, has been, or will become, active in its lifetime. In order to determine robust answers for these questions, a complete census of active galaxies in the Universe is necessary to allow for the study of the cosmic evolution of AGN and a complete understanding of the active galaxy system in of itself must be known.

1.4.1 X-ray

1.4.2 UV and Optical

1.4.3 Infrared

1.4.4 Gamma and Radio

1.5 The host galaxies of active galactic nuclei

1.6 Thesis Structure

The research presented in this thesis selects a sample of active galaxies based purely on their near-infrared variability. It then compares the properties of this sample to active galaxies selected through X-ray emission, which is a technique more commonly used in scientific research. The variability detected active galaxies are then further grouped, based on the IR waveband of detection, and the properties of these are investigated to deduce possible structures in active galaxies as a whole.

In Chapter 2, we describe the data used in this research. We make use of the UKIDSS UDS, which was taken on The UKIRT Wide Field Camera (WFCAM). We detail the multi-wavelength catalogues of the field as well as how redshifts and stellar masses were calculated. We also describe the X-ray imaging of the UDS field and its comparative coverage.

In Chapter 3 we explain the method used to select AGN based on their NIR variability in the J and K-bands. We describe the cleaning of the dataset after selection, as well as how variability amplitudes are measured and how detection limits of the survey are calculated.

Chapter 4 consists of a comparison between the properties of active galaxies selected through NIR variability, and active galaxies selected by X-ray emission.

In Chapter 5 we split the NIR variable active galaxies based on their variability in the J and K-bands. We then investigate if the properties of the galaxies are different depending on the band they are variable in.

Chapter 6 - AGN variability + host galaxy properties

Finally, in Chapter 7, we summaries the results and present the overall conclusions of the work.

Much of the method described in Chapter 3 and the research shown in Chapter 5 is published in Paper I. The work presented in Chapter 5 and the accompanying method described in Section 3.5 is in preparation to be submitted in Paper II. All magnitudes stated are AB magnitudes. We use a Λ cold dark matter (ΛCDM) cosmology, with H_0 = 70 kms^{-1}Mpc^{-1}, Ω_Λ = 0.7 and Ω_m = 0.3.

Chapter 2

Data

In this work, we make use of data from multiple deep surveys: the UKIDSS Ultra Deep Survey (UDS; Almaini et al., in prep); combined with the *Chandra* Legacy Survey of the UDS field (X-UDS; Kocevski et al. 2018). A plot of the extent of the fields is shown in Figure 2.1.

2.1 UDS

The UDS is the deepest of the UKIDSS surveys (Lawrence et al., 2007) and the deepest NIR survey over $\sim 1\,\mathrm{deg}^2$. Its JHK band imaging was taken over an 8 year period from 2005–2013 using the WFCAM instrument at UKIRT (Casali et al., 2007). Although not primarily designed to study variability, the collection of the data spread over eight years offers a powerful resource for long-term infrared variability studies. In addition to this, the field is well studied and as such has additional imaging in many other wavebands including:

- u'-band imaging from the Canada–France–Hawaii Telescope (CFHT) MegaCam.
- B, V, R, i' and z'-band optical imaging from the Subaru *XMM-Newton* Deep Survey (SXDS; Furusawa et al., 2008).
- Y-band imaging from the VISTA VIDEO survey (Jarvis et al., 2013).

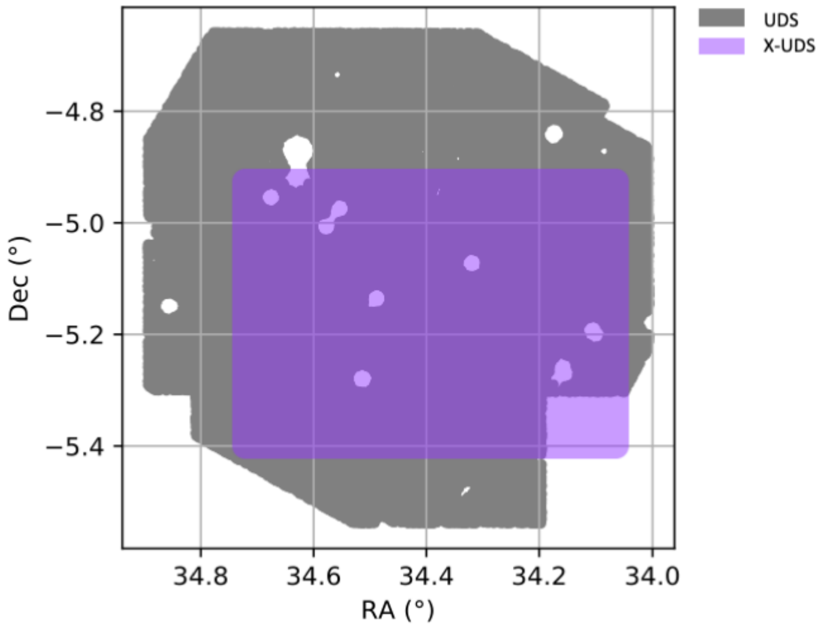

Figure 2.1: The survey region of the Ultra Deep Survey (UDS) and the *Chandra* Legacy Survey of the UDS field (X-UDS). The grey shaded area shows the subset of the ground-based UDS field where there is reliable photometry in all 12 photometric bands, and the purple shaded area shows the coverage from the *Chandra* X-UDS imaging.

- 3.6 μm and 4.4 μm mid-infrared (MIR) IRAC imaging from the *Spitzer* UDS Legacy Programme (PI: Dunlop).

The DR11 is the latest data release from the Ultra Deep Survey (UDS). This data release has 296,007 K-band detected sources and 5σ limiting depths of J = 25.6, H = 24.8 and K = 25.3 (AB in 2-arcsec diameter apertures; Almaini et al. 2017; Almaini et al., in prep). From this data release we make use of the '*best galaxies*' subset which covers 0.62 deg^2, and comprises objects identified in unmasked regions of the field with reliable photometry in all 12 bands, the deepest IRAC imaging, and with galactic stars removed. Masked regions correspond to boundaries of the science image, artefacts, bright stars and detector cross-talk. The *best galaxies* subset contains 202,282 K-band detections.

2.1.1 Redshifts

Of the 202,282 galaxies, 6558 have secure spectroscopic redshifts provided by complementary spectroscopic surveys (e.g., UDSz, VANDELS; Bradshaw et al., 2013; McLure et al., 2013; Maltby et al., 2016; McLure et al., 2018; Pentericci et al., 2018). For non-variable objects, spectroscopic redshifts are used (where available); otherwise, photometric redshifts are adopted.

Photometric redshifts for non-variable objects were calculated according to the methodology described in Simpson et al. (2013). For this, the 12-band photometry was fit using a grid of galaxy templates constructed from the stellar population synthesis models of Bruzual & Charlot (2003), and used the publicly available code EAZY (Brammer et al., 2008). These photometric redshifts have a typical accuracy of $\frac{\Delta z}{(1+z)} \approx 0.018$. Additional properties used in this work (e.g. stellar mass and luminosity; Almaini et al., in prep), are based on these redshifts and are entirely adequate for our purposes.

In this paper, we identify IR-variable objects (see Section 3.1). For these objects, spectroscopic redshifts were used (where possible) over photometric determinations. For the variability detected sources for which spectroscopic redshifts were not available, inaccuracies in the photometric redshifts are a potential concern due to the AGN emission not being accounted for. To address this, we have recalculated the photometric redshifts for these objects via the EAZY redshift fitting code. Here additional reddened and unreddened AGN templates were included in the fitting. Comparing the median absolute deviation of $\frac{\Delta z}{(1+z)}$ before and after including the recalculated photometric redshifts, indicates the redshifts improve only marginally from $\sigma_{\rm MAD} = 0.10$ to $\sigma_{\rm MAD} = 0.098$. This demonstrates the initial photometric redshift values to be largely robust. Regardless, the recalculated redshifts for the IR-variable active galaxies are used throughout this work, though we note that using the original photometric redshifts made no significant difference to our analysis or conclusions.

2.1.2 Stellar Masses

Stellar masses (Almaini et al., in prep), were calculated using the method described in Simpson et al. (2013). Here, the 12-band photometry was fit to a grid of synthetic SEDs from the stellar population models of Bruzual & Charlot (2003) with a Chabrier (2003) initial mass function. Typical uncertainties in these stellar masses are of the order ±0.1 dex. The redshift-dependent, 90 per cent stellar mass completeness limits were calculated using the method described in Pozzetti et al. (2010). A second order polynomial was fit to the resulting completeness limits across a wide redshift range to give a 90 per cent mass completeness curve of the form $\log_{10}(M_*/\mathrm{M}_\odot)$ = -0.04z^2 + 0.67z + 8.13.

2.2 X-UDS

The X-UDS survey is a deep X-ray survey of a sub-region of the UDS field carried out by the *Chandra* X-ray Observatory's Advanced CCD Imaging Spectrometer (ACIS). It comprises a mosaic of 25 observations of 50 ks exposure, totalling 1.25 Ms of imaging. It covers 0.33 deg^2 in total (Kocevski et al., 2018) and has a flux limit of $4.4\times10^{-16}\,\mathrm{erg\,s^{-1}cm^{-2}}$ in the full band (0.5–10 keV). In total, 868 point sources were identified.

This data set was matched to the UDS DR11 K-band catalogue using the methodology described in Civano et al. (2012), which adopted the maximum likelihood method described in Sutherland & Saunders (1992). Through this analysis, we find that 710 of these point sources are associated with K-band–selected galaxies in the UDS DR11.

2.3 CANDELS

[GalfitM data needs to go here]

Chapter 3

Quantifying AGN variability

3.1 Selecting AGN based on their IR variability

IR-variable AGN are selected from the UDS DR11 using the technique first developed and used in Elmer et al. (2020). Here, the authors were able to construct NIR light curves from multiple flux measurements that spanned 7 semesters in the K-band. Errors on the flux measurements were self-calibrated, based on the population variance in flux of the non-variable objects, as this provided a better fit to the data than the errors generated by SExtractor (see Figure 3. in Elmer et al. 2020). To do this, the authors began by convolving each semester stack of images with a Gaussian kernel to match the stack with the poorest quality PSF. This ensured that the differences in flux measurements were due to intrinsic AGN variability and not changes in the point spread function from semester to semester. A preliminary χ^2 analysis was then performed to remove the most variable sources and the remaining light curves were normalised and split into bins based on flux, epoch and quadrant. From this the standard deviation of the binned flux values provided the photometric error on the measurements for the objects in that bin.

After the publication of Elmer et al. 2020, additional J-band imaging was incorporated into the dataset. First an updated catalogue of galactic stars was developed for the UDS DR11 release, none of which were included in the initial K-band sample selection. These stars were used to improve the PSF images prior to convolving the data to match the semester with the poorest PSF (see Section 2.2 of Elmer et al. 2020), allowing for an improved sample selection in the K-band. Furthermore, the 2006B semester in the J-band had sufficient observations to allow it to be included in the light curves. This gives the J-band a total of 8 epochs for study.

We further select only objects with reliable (unmasked) photometry in all 12 bands, to ensure the most reliable photometric redshifts. Objects identified as galactic stars were excluded, as were any galaxies close to cross-talk detector artefacts. We also exclude any objects with formally negative flux values in any individual semester, as described in Elmer et al. (2020). This final step largely excluded very faint galaxies at $K > 25$, close to or beyond the formal detection limit of the survey. Inspecting this faint subgroup reveals that all would be excluded by the eventual J-band magnitude cut described in Section 3.4, so have no impact on our analysis. Overall, these rejection criteria yield a final sample of $114,243$ light curves for this study.

Errors on the flux measurements were self-calibrated, based on the population variance in flux of the non-variable objects at the same apparent magnitude, as this provided a better fit to the data than the errors generated by SExtractor (see Figure 3 in Elmer et al. 2020). A full description of this process can be found in Section 2.2 of Elmer et al. (2020).

IR-variable AGN were selected using a χ^2 analysis applied to the IR light curves based on the null hypothesis that flux measured from the object is constant with time. Thus we calculate

$$\chi^2 = \sum_i \frac{(F_i - \bar{F})^2}{\sigma_i^2}, \tag{3.1}$$

where for each semester i, F_i is the flux of an object, σ_i is the corresponding uncertainty and $\bar{F}$ is the mean flux of that object across all imaging epochs. A threshold of $\chi^2 > 30$ was used for the K-band and we use $\chi^2 > 32.08$ for the J-band. The differing χ^2 limits give the same p-value for both χ^2 distributions based on the J and K-band light curves, accounting for the different number of imaging epochs and therefore differing degrees of freedom. If a galaxy satisfies either or both conditions, it is classed as hosting a variable AGN.

Utilising this method to select significantly variable objects via the χ^2 analysis, we are able to identify a sample of 705 candidate active galaxies for study (430 from K-band variability, 471 from J-band variability, with 196 detected by both). We recover all of the 393 K-band selected AGN found in Elmer et al. 2020, with a modest increase due to the improvements in the data analysis since the publication of that work. From the initial data set of 114,243 galaxies with IR light curves, we would expect a total of 4 false positives based on a χ^2 distribution with this number of degrees of freedom.

To search for potential supernovae in the sample, tests were carried out according to Section 5 of Elmer et al. 2020. We identified 36 of the 471 J-band variables (7.6 per cent) for which the variability is largely driven by one epoch. Inspection of both the J and K-band imaging and comparing epochs revealed no obvious signs of supernovae (e.g., off-nuclear sources). No additional supernova candidates were identified among the new K-band variables not analysed by Elmer et al. 2020. Removing this small number of galaxies had no influence on any of the key conclusions presented in this work.

3.2 Galaxies on the edge of the science image

Visual inspection revealed a suspicious sample of 104 variable objects located very close to the detector edges. These objects were inspected individually within each epoch, and approximately ∼33 per cent were identified as potentially fake variables. All objects were found to be real galaxies, but in many cases false variability could be attributed to problems with background subtraction at the detector edges. As such, we re-ran all analysis both with and without this sub-sample of galaxies, and found no significant change in the overall reported trends. Therefore, we removed these edge objects entirely from the analysis to ensure robust results. The remaining sample consists of 601 galaxies.

We note that the pattern of false variables occurred only at the outer edges of the UDS imaging. There was no evidence for false positives close to the internal WFCAM chip boundaries in the UDS mosaic.

3.3 Measuring real variability: maximum likelihood

For any measurement of an active galaxy light curve, we know that the observed dispersion in flux (σ_{obs}) is due to a combination of the intrinsic magnitude variations due to the active galactic nucleus (σ_{Q}) and the measurement noise (σ_{noise}) such that

$$\sigma_{\mathrm{obs}}^2 = \sigma_{\mathrm{Q}}^2 + \sigma_{\mathrm{noise}}^2. \tag{3.2}$$

Consequently, if we are to measure the properties of the AGN, we have to be able to separate out these two effects.

As such, to calculate the fractional variability amplitude due to AGN emission (σ_{Q}), we make use of a maximum likelihood technique. This method, developed in Almaini et al. (2000), allows for an estimate of the noise-subtracted intrinsic fractional variance (σ_{Q}) of the AGN, within the observed variability (σ_{obs}). We first take any given AGN light curve and generate a likelihood function

$$L(\sigma_{\mathrm{Q}} \,|\, x_i, \sigma_i) = \prod_{i=1}^{N} \frac{\exp[-(x_i - \bar{x})^2/2(\sigma_i^2 + \sigma_{\mathrm{Q}}^2)]}{(2\pi)^{1/2}(\sigma_i^2 + \sigma_{\mathrm{Q}}^2)^{1/2}}. \tag{3.3}$$

To generate each point in the likelihood curve, we normalise each galaxy light curve such that the average flux ($\bar{x}$) is unity. We then step through possible values of fractional AGN variability (σ_{Q}) using the measurement of the flux in each semester (x_i) and its corresponding measurement error (σ_i). To get the final likelihood measurement, we take the product of the N values that have been calculated where N is the number of flux measurements in a given light curve.

In order to determine the most likely value of σ_{Q} for each active galaxy, we simply select the value of σ_{Q} that maximises the likelihood function, as seen in Figure 3.1. Here the 1σ errors are calculated by assuming the likelihood curve has a Gaussian shape.

3.4 Variability detection limit

The χ^2 detection method is inevitably sensitive to photometric errors, and thus in fainter galaxies we can only expect to detect variability at higher fractional amplitude. We can attempt to quantify this effect, to estimate our completeness in identifying variable AGN with a range of intrinsic variability amplitudes (σ_{Q}), and over a range of apparent magnitudes. To begin, we remove any active galaxies via their IR variability or X-ray emission from the initial sample of 114,243 galaxies and then split the remaining inactive galaxies into bins based on apparent magnitude. Then, to simulate variability in the inactive galaxies, we artificially introduce variability to their light curves assuming a Gaussian distribution of variations. We require this (variable) component to have a mean of zero and a standard deviation equal to the degree of variability we are simulating, and add this distribution to the normalised inactive galaxies light curves. We then re-run the χ^2 and maximum likelihood analysis on the 'new' light curve for each galaxy, which now contains simulated variability. This allows us to determine if it is now classed as hosting a significantly variable object by the χ^2 analysis and to ascertain the most likely amplitude of simulated variability using the maximum likelihood technique. This procedure is repeated for a range of variability amplitudes and for each apparent magnitude bin. The results are then used to determine, for a given apparent magnitude, the minimum fractional variability amplitude required for an AGN to be consistently detectable. This also allows us to compare the known simulated variability amplitude

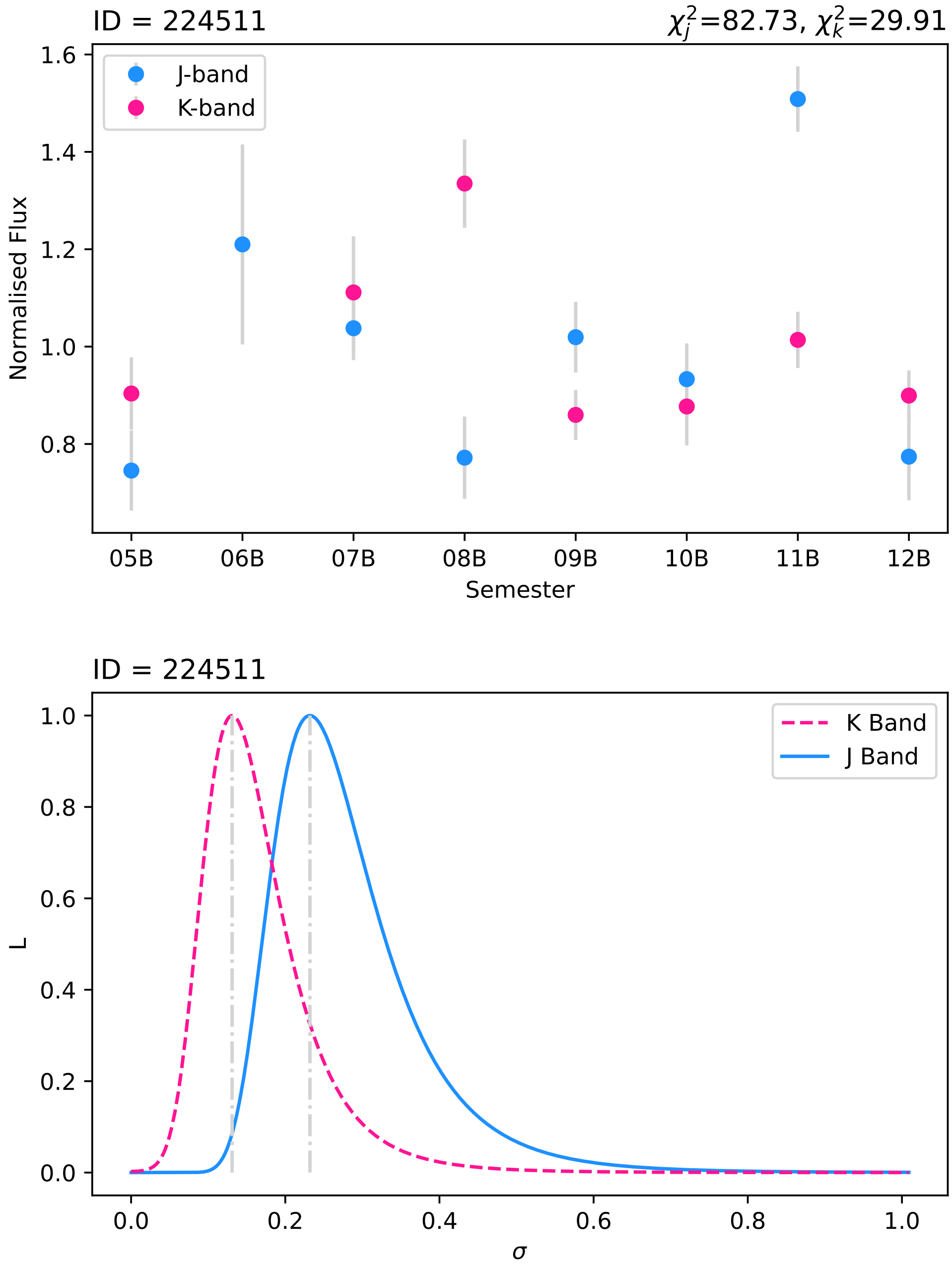

Figure 3.1: Example light curves for a variable galaxy candidate in both the J and K-band (top panel) and the corresponding normalised likelihood curves (bottom panel). The threshold for recovery of AGN variability from a given light curve is $\chi^2_K > 30$ and $\chi^2_J > 32.08$. As shown by the grey lines in the bottom panel, the variability amplitude is determined by selecting the corresponding value for σ_Q that maximises the likelihood function. This galaxy is only classified as formally variable in the J-band (blue), as shown by the value of the χ^2.

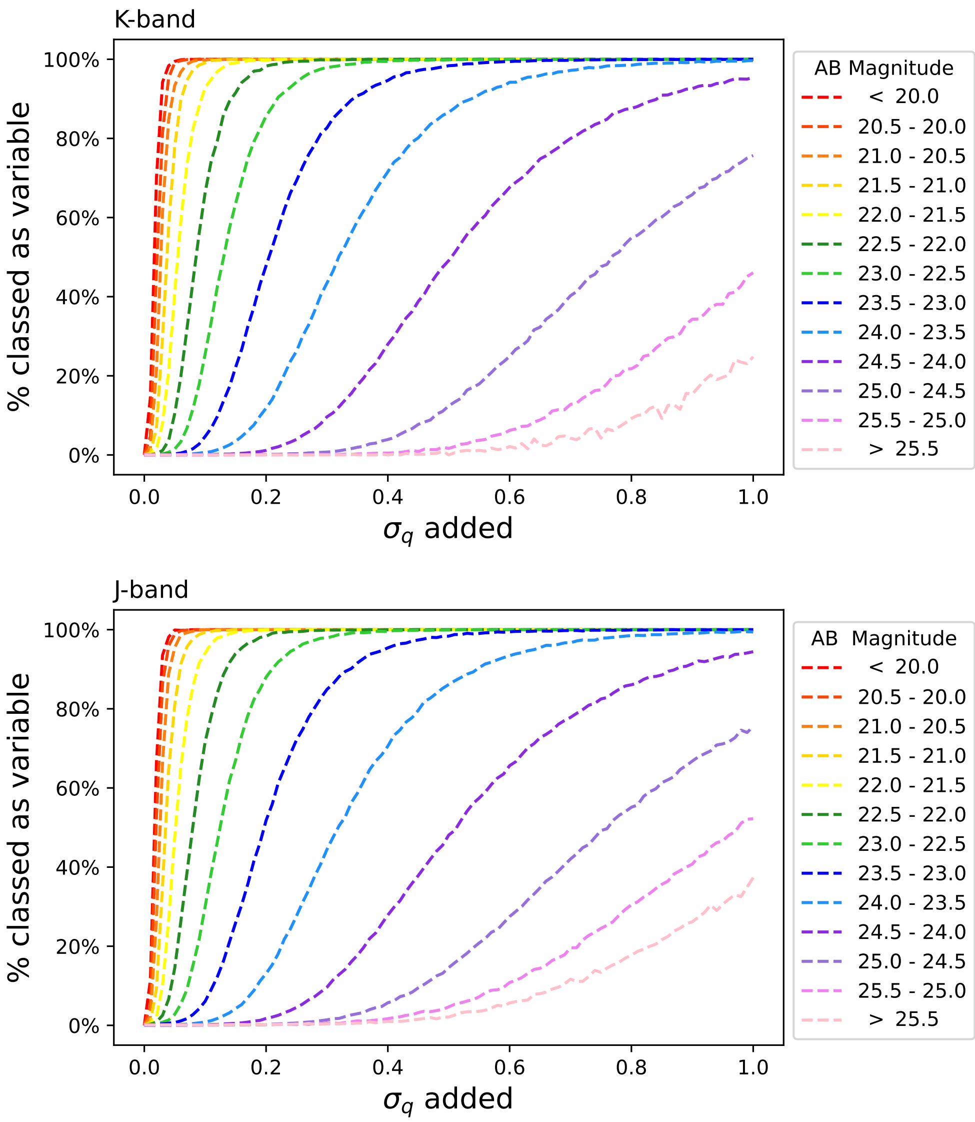

Figure 3.2: The fraction of galaxies classed as hosting variable AGN compared to the level of artificial variability added to the inactive galaxy light curves. Results are shown for the *K*-band (top panel) and *J*-band (bottom panel). Each dashed line represents a different apparent magnitude bin. In the brightest bins, lower uncertainties on measurements allow for low amplitudes of variability to be recovered. However, larger variability amplitudes are required for AGN to be detected in the faintest galaxies.

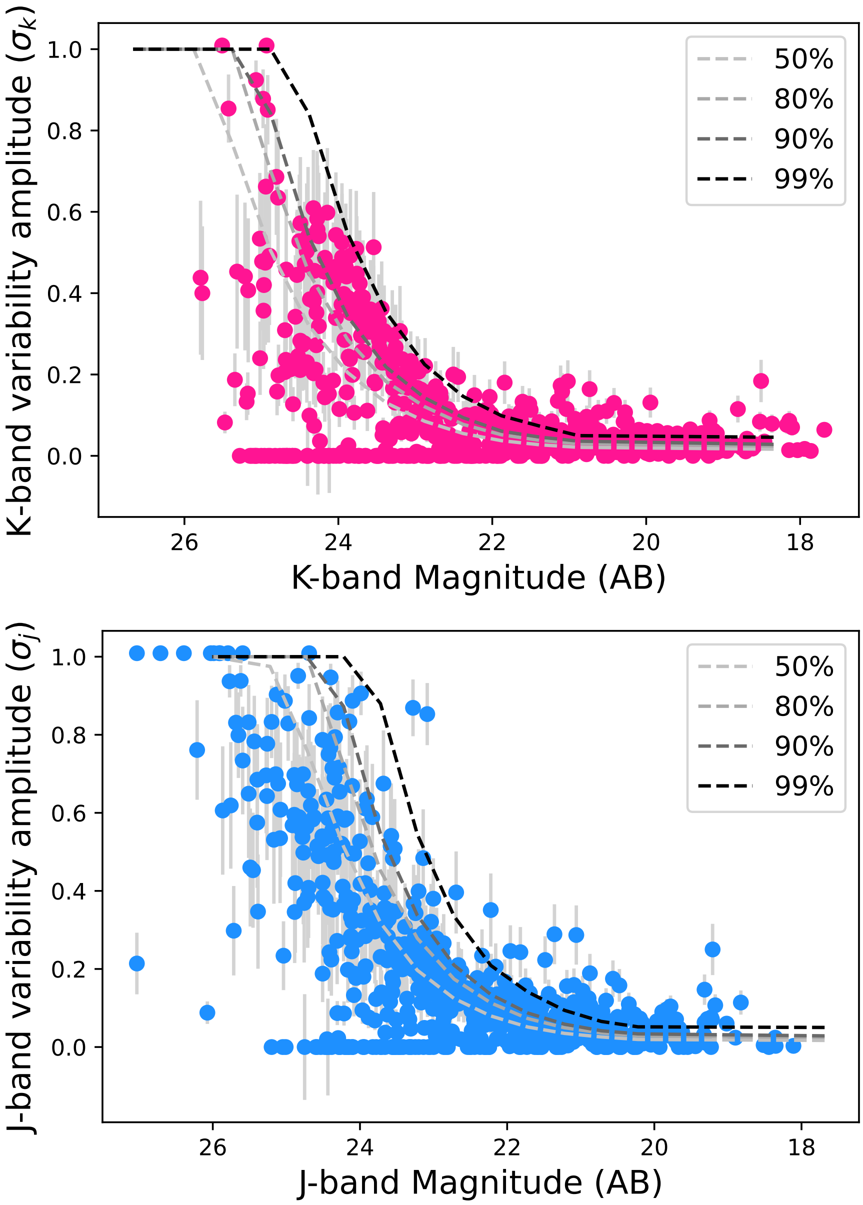

Figure 3.3: AB magnitude vs. variability amplitude for the *real* variable active galaxies. Pink points indicate galaxies selected as hosting variable AGN in the K-band (top panel), while blue points show the same data but for the J-band (bottom panel). Grey 1σ errors are based on assuming a Gaussian fit to the likelihood curves. Overlaid are detection limit curves for different levels of completeness. We use the 90 per cent curve as this threshold provides a high level of completeness without over-reducing the sample size.

to the amplitude recovered via the maximum likelihood method.

We find that the maximum likelihood technique accurately recovers the amplitude of input AGN variability. Sampling galaxies from each magnitude bin, the average difference in variability amplitude is consistently of the order of 1 per cent. Using these simulations, we are also able to calculate the fraction of galaxies classed as hosting an AGN for every value of simulated $\sigma_{\rm Q}$ in each magnitude bin (see Figure 3.2). This provides a suitable estimate for the completeness of our NIR variables, as a function of both apparent magnitude and variability amplitude.

As seen in Figure 3.3, for a given value of an AGN's fractional variability amplitude and a selected completeness level, we can determine the apparent magnitude required for that selected variability amplitude to be consistently detected to the desired completeness. Throughout this work, we adopt the 90 per cent completeness threshold for a variability amplitude of 20 per cent or higher. From the J-band curve in Figure 3.3, we find this requires our galaxies to have apparent magnitudes of $m_J \leq 22.66$.In the K-band, the same limit requires an apparent magnitude of $m_K \leq 23.25$. We use the J-band limit in this work as it is stricter, and removes all galaxies excluded by the K-band limit.

3.5 Modified monthly variability amplitude

We can also probe variability on different timescales, which allows us to determine possible NIR emission mechanisms, as different processes occur on different timescales. The timescale variability takes place on also allows for insight into the NIR power spectrum of the variability in the active galaxies. To compare the timescale that variability takes place on, we calculate a modified monthly variability amplitude measurement in addition to the year/semester timescale measurements of fractional variability amplitude. These measures will be used in Chapter 5, where we analyse if and how the properties of the AGN differ depending on the band they were detected as significantly variable in.

To begin, we use the infrared light-curves built in Elmer et al. 2021, where flux measurements were taken between September 2005 and November 2012 on month timescales. The mean flux of the overall, unaltered light curve is calculated ($\overline{F}$) and we then group the flux measurements based on the date they were taken, with flux measurements being

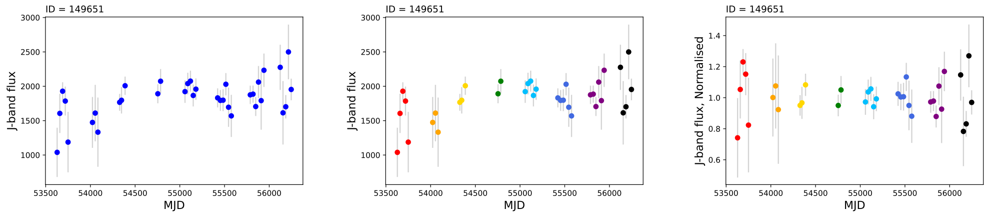

Figure 3.4: Example of the month light curve modification process in the J-band. In all plots, circular points denote flux measurements and grey lines are error bars. Left is the unaltered light curve comprised of flux measurements on month timescales and in the centre we show the group selection, where measurements within 120 day of each other are grouped together. The right plot shows the final modified light curve, after long-term (year scale) trends are subtracted from the flux measurements and each group is normalised such that the mean is unity. The process for K-band modification is identical, with K-band data being used in place of J-band measurements.

required to be within 120 days of each other to be grouped together. For each group in the light curve, the average is computed ($\overline{F}_{group}$), the difference between it and the overall mean is taken ($\overline{F}_{group}$ - $\overline{F}$) and this value is subtracted from the corresponding group's average to remove the effects of long-term (year scale) variations in the month-scale flux measurements. Each group is then normalised such that the average flux is unity. Finally, the maximum likelihood measurement as described in Section 3.3 is applied to the modified light curve to calculate what we refer to as the modified fractional variability amplitude on month timescales.

An illustration of this process is presented in Figure 3.4, which shows how the overall trends on year timescales are removed whilst preserving any month-scale variability that may occur within an AGN system. We also note that whilst we refer to the value measured in this process as a modified month-scale variability amplitude, it is only the month-scale light curves used that are changed, with the procedure by which the variability is measured (i.e. the maximum likelihood technique) remaining unaltered.

Chapter 4

Long-term near-infrared variability

In this work we compare the properties of the 601 NIR variability selected active galaxies in Chapter 3 to a sample of 710 X-ray detected active galaxies from the X-UDS (Chapter 2). We then investigate if and how the properties of active galaxies differ depending on the detection method. This work was published in Paper I.

4.1 Introduction

Variability has been shown to be a useful tool in selecting AGN, being able to complement other selection methods by succeeding where they fail. X-ray emission, for example, is commonly thought to have a high probability of selecting the most complete sample of active galaxies (e.g., Suh et al. 2019, Pouliasis et al. 2019), but this method is intrinsically biased against X-ray-faint objects. In Trevese et al. (2008), a study of low-luminosity AGN found that only 44 per cent of their optical-variability–selected active galaxies have associated X-ray emission. Pouliasis et al. (2019) also selected AGN via optical variability and X-ray emission, but additionally employed the use of IR colour selection. They find that 23 per cent of their variable sample have associated X-ray emission, and only 12 per cent of their variable sample satisfies the IR colour selection criteria for the presence of an AGN. More recently, Lyu et al. (2022) used a wide combination of selection techniques, including radio emission, X-ray detection, variability, UV–IR SED analysis, optical spectroscopy, and IR colour selection in an attempt to find a complete sample of active galaxies in the GOODS-S field. They concluded that no single method was able to select a complete sample of galaxies, and the overlap in the AGN found by different techniques was small.

AGN variability is a relatively unexplored property at infrared wavelengths due to the time required to observe it, but one which is believed to provide significant insight into the nature of the outer edges of the AGN system. In principle, this technique may also provide an advantage in identifying heavily-obscured and/or high-redshift AGN, which may be missed by optical/UV selection techniques. Furthermore, deep wide-field imaging can allow us to study thousands of galaxies simultaneously.

Until recently, studies of IR variability either focused on a handful of individual objects (Cutri et al. 1985, Lira et al. 2011, Lira et al. 2015), observed AGN selected by other means (Kouzuma & Yamaoka 2012, Sánchez et al. 2017, Son et al. 2022), or studied light curves that are not well sampled (Edelson & Malkan, 1987) or constructed from observations from multiple different surveys (Neugebauer et al., 1989). However, Elmer et al. (2020) were the first to select AGN in large numbers based purely on their NIR variability using a single deep data set, and it is this sample we build upon in this work.

In this paper, we investigate the properties of active galaxies selected using NIR variability. We use J-band light curves to select significantly variable AGN in addition to the K-band light curves and method described in Elmer et al. 2020. We then compare the properties of these galaxies to a sample of AGN selected via X-ray selection, to determine if and how the properties of active galaxies differ depending on the detection method. We make use of nearly a decade of IR observations provided by the Ultra Deep Survey (UDS; Almaini et al., in prep); the deepest component of the UKIRT (United Kingdom Infra-red Telescope) Infrared Deep Sky Survey (UKIDSS; Lawrence et al., 2007). We use this data to select 601 active galaxies between $0 < z \leq 5$ based purely on their IR variability using the technique developed, as well as the data constructed, in Elmer et al. (2020). We then compare the properties of these active galaxies to those found using X-ray emission from the X-UDS survey (Kocevski et al., 2018), as well as a control sample of inactive galaxies.

4.2 X-ray faint active galaxy populations

We applied the AGN variability detection method described in Section 3 to the UDS DR11, and compared the results to the full-band (0.5–10 keV) *Chandra* X-UDS catalogue described in Section 2.2. If we limit the UDS and the X-UDS to the same survey area (see Figure 2.1, for reference), the samples are largely separate. Of the 601 variability detected active galaxies, 292 lie within the *Chandra* imaging region. The percentage of these that are dual-detected AGN (i.e. X-ray detected and variable in the NIR) is only ∼37 per cent (107 / 292).This represents ∼15 per cent of the X-ray detected sample (107 / 710).

One possible explanation for this result is that NIR-variable AGN have X-ray emission that is too faint to be detected at the depth of the X-UDS survey. X-ray emission from AGN has long been known to correlate with optical/UV emission (e.g., Tananbaum et al. 1979,Avni & Tananbaum 1986). Therefore, to address this issue, we compare the observed X-ray–to-optical luminosity ratios to determine if the variability-detected AGN are unusually X-ray quiet (for galaxies that reside within the X-UDS survey region). In Figure 4.1, we compare the monochromatic luminosities at 2 keV and 2500 Å, compared with the expected ratios assuming point-to-point spectral slopes with $\alpha_{ox} = 1$ and $\alpha_{ox} = 2$, corresponding to the typical range observed for quasars (e.g., Steffen et al. 2006).

We note, however, that in our work we make no corrections for host galaxy contributions, dust reddening, or X-ray absorption. We are comparing the observed X-ray to optical ratios, to determine if the objects selected by variability show similar ratios to those selected with deep Chandra observations.

Here, monochromatic luminosities at 2500 Å are derived from the observed optical/UV SEDs, given the source redshift, interpolating the flux between the nearest observed wavebands. The monochromatic X-ray luminosities are determined from the 0.5-10 keV X-ray flux, assuming an X-ray photon index $\Gamma = 1.9$ for all sources, as used in Elmer et al. (2020). X-ray upper limits from Kocevski et al. (2018) are used for X-ray non-detections. Overall we find that many variable active galaxies have similar optical luminosities to X-ray bright active galaxies, but the majority have only upper limits in our X-ray imaging. Based on the data available to us, the variable AGN appear systematically fainter in the X-rays.

One possible explanation is that the variable AGN are more obscured in the X-ray waveband, but deeper X-ray data will be needed to test that hypothesis. Overall, the implication is that near-infrared variability appears to detect a set of active galaxies that are largely missed by X-ray surveys at these depths.

4.3 Active Galaxy Properties

4.3.1 Stellar mass distributions and quasar contamination

In addition to there being limited overlap in AGN selected using NIR variability and X-ray detection, we find a difference in the stellar mass ranges of active galaxies selected via X-ray detection and NIR variability. Examining the mass distribution with redshift

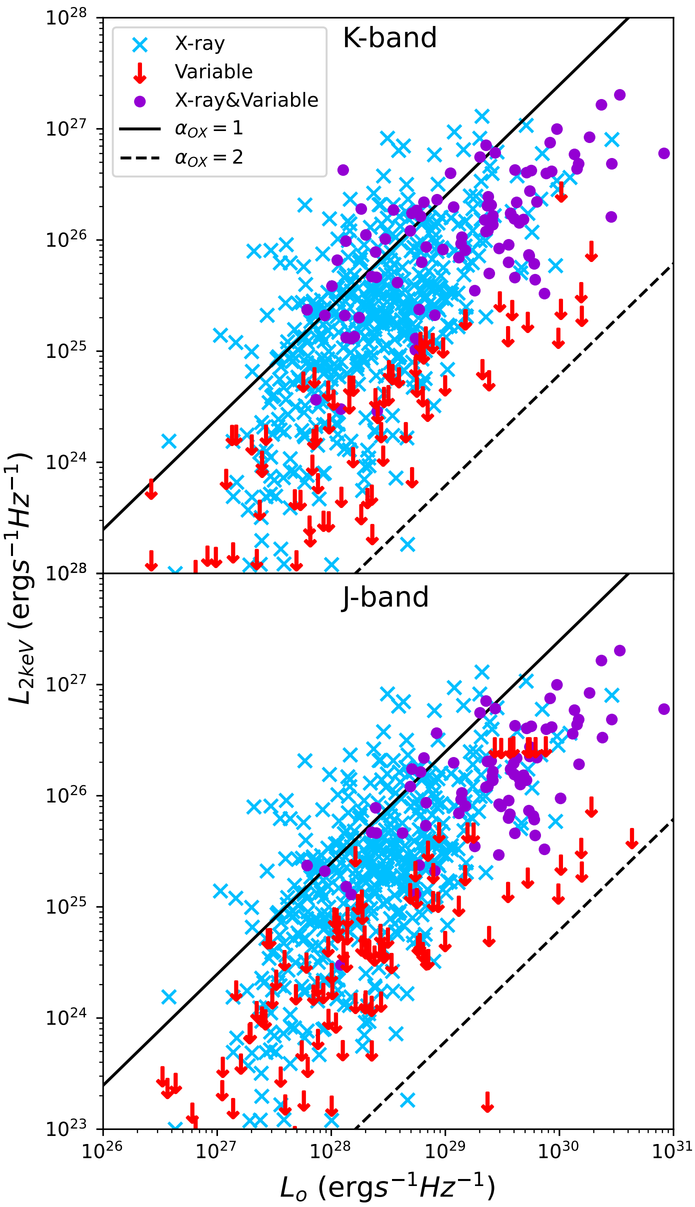

Figure 4.1: Monochromatic 2 keV X-ray luminosity vs. rest-frame optical luminosity at 2500 Å for objects imaged within the *Chandra* region of the UDS field. X-ray bright active galaxies are denoted by blue crosses and AGN detected by both NIR variability and X-ray emission are highlighted as purple dots. Upper limits are used for variability-detected active galaxies without X-ray detections, and are shown by red arrows. The top plot shows K-band detected active galaxies and the bottom plot shows J-band detected active galaxies. Black lines indicate the slopes corresponding to a spectral index ($\alpha_{\rm ox}$) of $\alpha_{\rm ox}$=1 (solid) and $\alpha_{\rm ox}$=2 (dashed), where $\alpha_{\rm ox}$ is the spectral index between the optical and the X-ray.

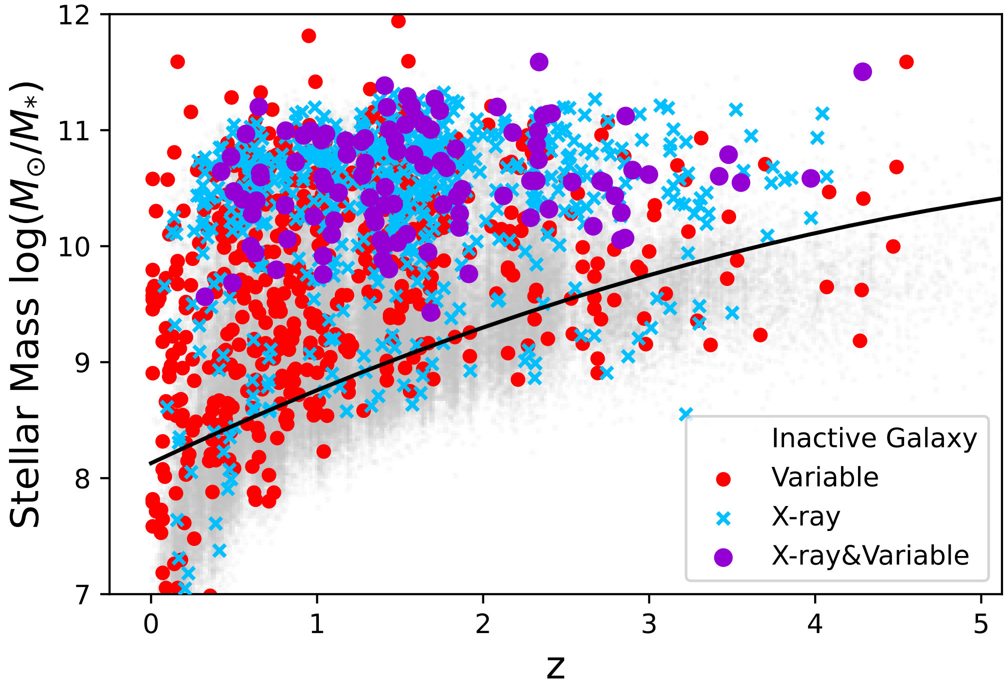

Figure 4.2: Stellar mass vs. redshift distribution for the galaxies in this study. X-ray bright active galaxies are shown as blue crosses, red circles denote variability-detected active galaxies, and purple circles show dual-detected active galaxies. Grey points are inactive galaxies, and the black curve shows the 90 per cent stellar mass completeness limit as a function of redshift.

in Figure 4.2, X-ray emission probes AGN in high-mass galaxies across all redshifts considered, with a majority of X-ray selected active galaxies having stellar masses $\geq 10^{10}\,\mathrm{M}_\odot$. This is in contrast to the active galaxies selected through variability, which show no obvious bias towards high-mass galaxies.

To illustrate these differences, in Figure 4.3 we plot the distribution of the stellar mass of the active galaxies, separated by detection method.

We find a clear distinction between any X-ray detected AGN, which are much more likely to exist in high-mass galaxies, and NIR variability detected AGN, which show a much more extended mass distribution.

One caveat to these results, however, is the potential for the contamination by non-stellar light, which may bias the stellar masses for the brightest AGN. To investigate this issue, we plot the measured stellar mass against the J-band absolute magnitude for all galaxies

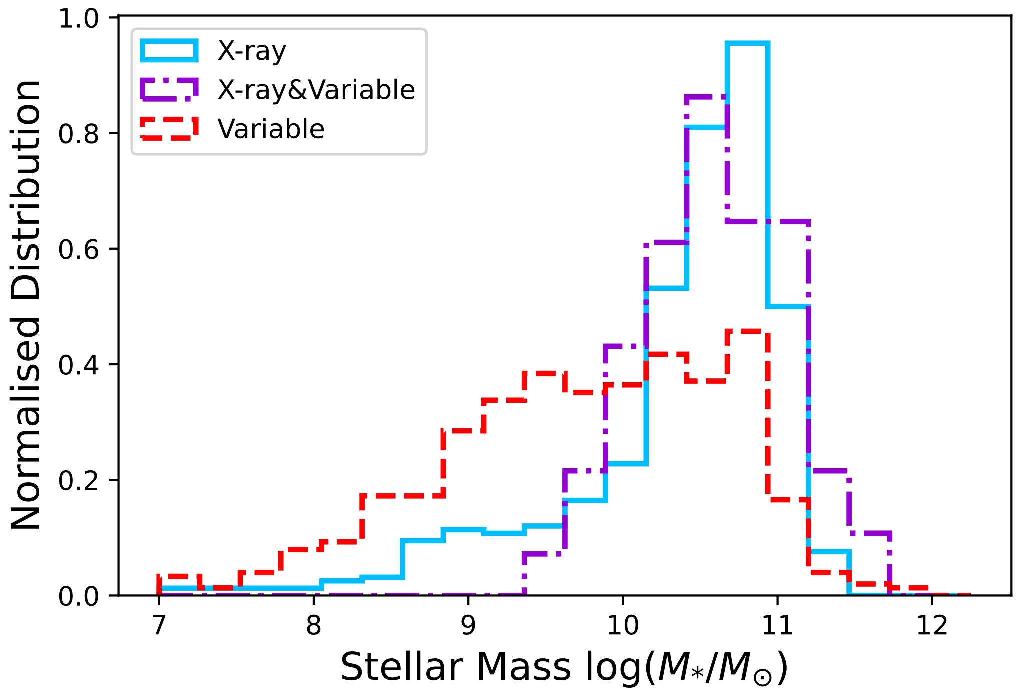

Figure 4.3: Normalised histograms showing the distribution in stellar mass of active galaxies in the sample. Galaxies are separated according to detection method, where the blue solid-lined histogram represents X-ray selected active galaxies, the red-dashed histogram shows objects classified as hosting variable AGN only, and the purple-dotted histogram shows objects that were detected using both methods. A Kolmogorov-Smirnov test confirms that the variability detected sample has a significantly different distribution in stellar masses compared to the X-ray population, rejecting the null hypothesis that they are drawn from the same underlying mass distribution with a significance of > 99.99 per cent.

in the field in Figure 4.4.

Here we find the active galaxies to broadly exist in two regimes: one where the measured magnitude of the galaxy is much brighter than inactive galaxies of a similar mass, and one where the measured magnitude of the galaxy is similar to inactive galaxies of a similar mass. From this bimodality, we can assume that the observed light from the active galaxies that lie within the locus formed by the inactive galaxies are dominated by the hosts' stellar light, and as such the measured host galaxy parameters are minimally impacted by the presence of an AGN. On the other hand, active galaxies that are much brighter than their inactive counterparts of similar mass likely have emission that is dominated by the AGN, suggesting the presence of a quasar.

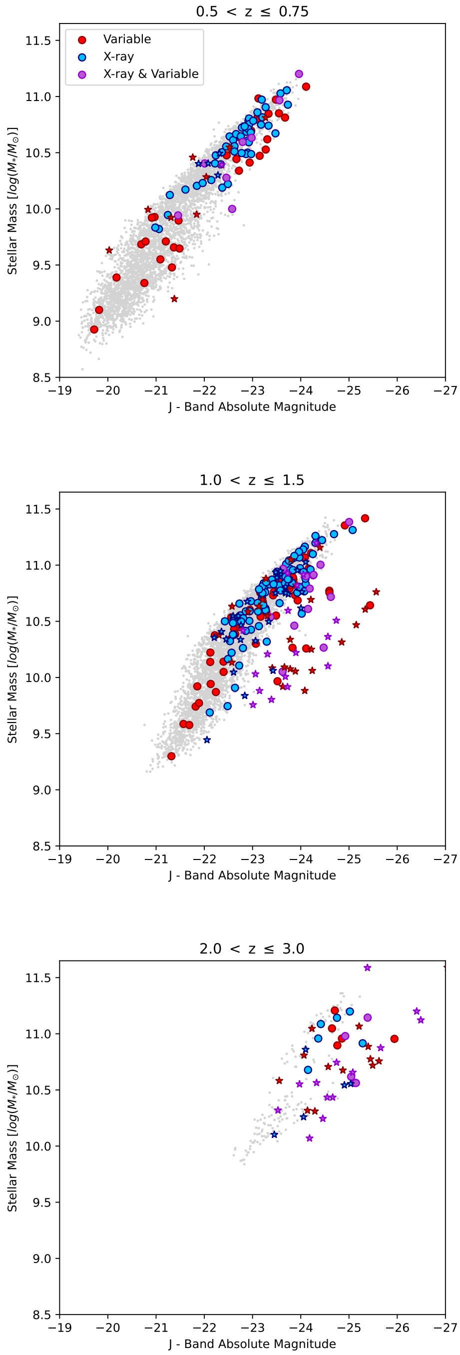

Figure 4.4: Stellar mass vs. J-band absolute magnitude for X-ray detected active galaxies (blue points), variability-detected active galaxies (red points) and dual-detected active galaxies (purple points) as a function of redshift. Inactive galaxies are plotted as grey points and all galaxies lie above the 90 per cent mass completeness limit. Corresponding coloured stars indicate an active galaxy that has a stellarity index of ≥ 90% according to the CLASS STAR parameter from SExtractor.

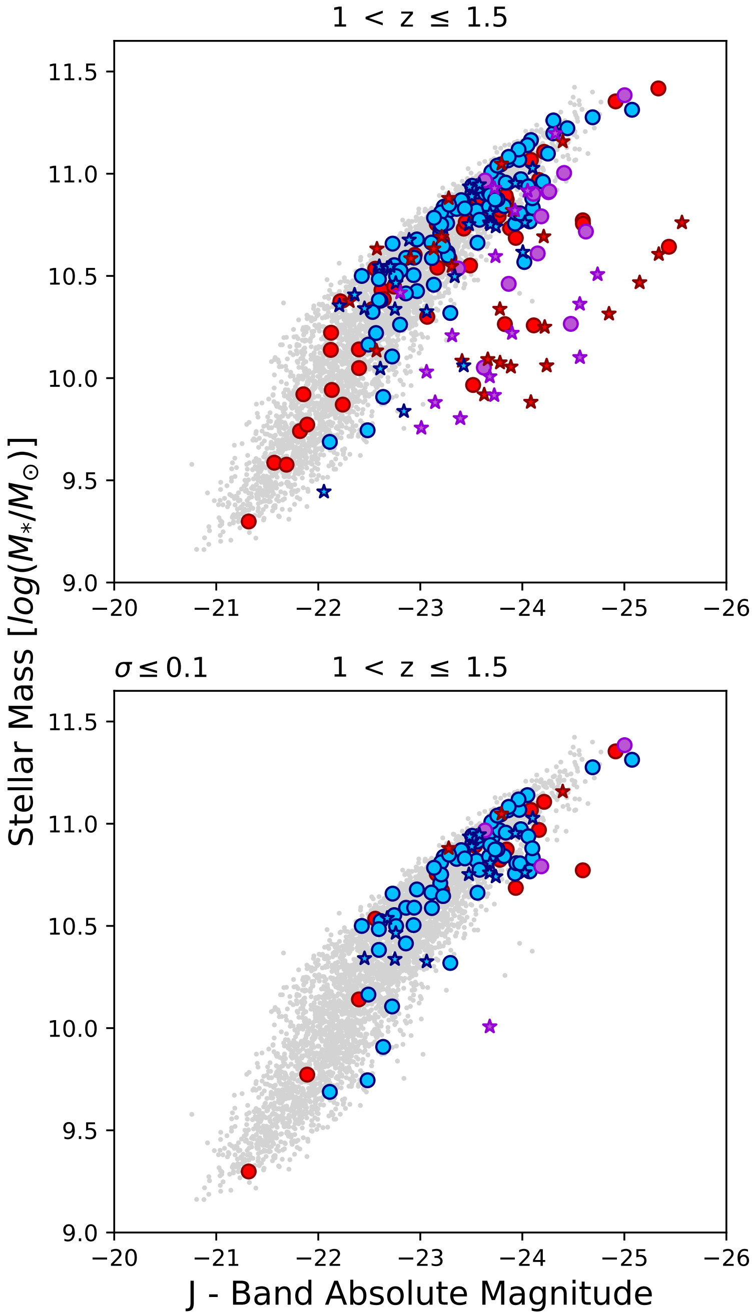

Figure 4.5: Stellar mass vs. J-band absolute magnitude for galaxies between $1 < z \leq 1.5$. Plotted are active galaxies (AGN) that are either X-ray-detected (blue points), variability-detected (red points), or dual-detected (purple points), as well as a comparison sample of inactive galaxies (grey points). Correspondingly-coloured stars indicate an active galaxy that has a stellarity index of ≥ 90% according to the CLASS STAR parameter from SExtractor. The bottom plot is as the top, but only shows active galaxies with (intrinsic) variability amplitudes of $\sigma_J \leq 0.1$. All galaxies plotted lie above the 90% mass completeness limit.

To test if these abnormally bright sources are quasars, we investigate their morphology using the K-band stellarity index from SExtractor, which (after removing galactic stars) provides a good indication that an AGN is dominating the emission from a source. From this we find that a majority of the bright sources appear point-like, which suggests the AGN emission is outshining that of the host galaxy.

These empirical trends are likely to be caused by a combination of factors. In particular, the stellar masses are obtained by fitting stellar population models, without an AGN component. If a Type-1 quasar dominates the SED, the best fit is likely to be an extremely young stellar population, yielding a very low mass-to-light ratio. As a secondary issue, the variable AGN were identified in the observed J and K bands, while observations at longer and shorter wavelengths were taken at different epochs. Therefore, as a selection effect, we might expect AGN to be brighter than average in the J and K bands, which would enhance their near-infrared luminosity relative to the stellar mass determined from the 12-band SED.

Furthermore, to investigate if a quasar is present within the identified bright, point-like sources, in Figure 4.5 we remove the objects with the largest variability amplitudes, on the assumption that the NIR light in such objects must be dominated by the AGN. Figure 4.5 shows the stellar mass vs. magnitude for galaxies with redshift $1 < z \leq 1.5$ both before and after requiring galaxies to have an intrinsic variability amplitude of $\sigma_{\rm Q} \leq 0.1$. Here we find that applying this limit primarily removes the point-like sources that are much brighter than inactive galaxies of a similar mass. In the case of objects detected via their X-ray emission, imposing this limit does not have a significant effect on the active galaxies that lie within the locus formed by inactive galaxies, but largely removes the bright, point like sources. It is therefore likely that the bright point-like active galaxies are indeed quasars, where the powerful AGN is driving significant variability and dominating the NIR light.

4.3.2 Stellar mass functions

To fairly compare the host properties of the active galaxies, we remove the quasars from the distributions to avoid significant amounts of non-stellar light impacting measurements. To do this we generate a contour that encompasses 95% of the inactive galaxies in each bin seen in Figure 4.4, and we require the active galaxies in corresponding bins

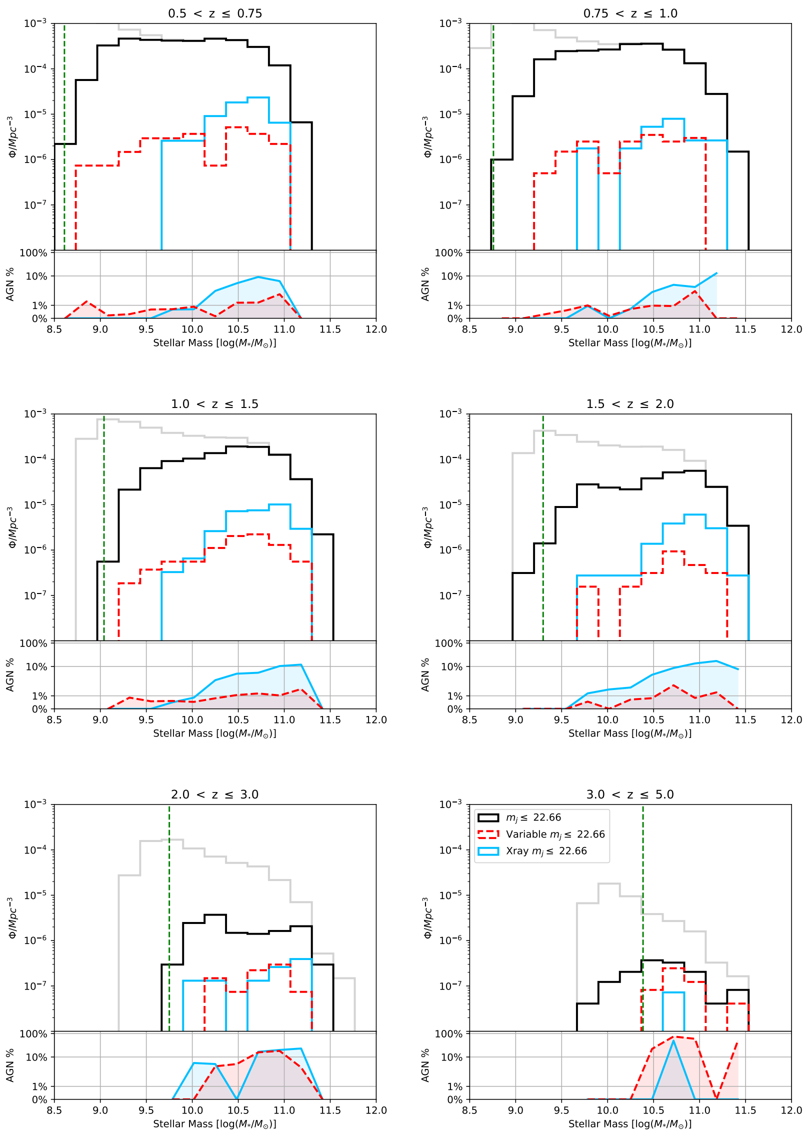

Figure 4.6: Stellar mass functions as a function of redshift. The grey histogram represents the mass distribution for all galaxies within the field except for quasar-like AGN, which have been removed. The black histogram shows the same but for galaxies with J-band apparent magnitudes $m_J \leq 22.66$ which ensures that a variability of 20% or higher will be consistently detectable. The dashed red histogram is as the black but shows only variability detected active galaxies. The solid blue histogram shows X-ray detected active galaxies, again with candidate quasars removed. X-ray detections were calculated using galaxies from the X-UDS imaging region and scaled to match the variability detected galaxies. The corresponding coloured distributions below each stellar mass function shows the percentage of AGN for that redshift bin as a function of stellar mass. The 90% mass completeness limit is denoted by the vertical dashed green line.

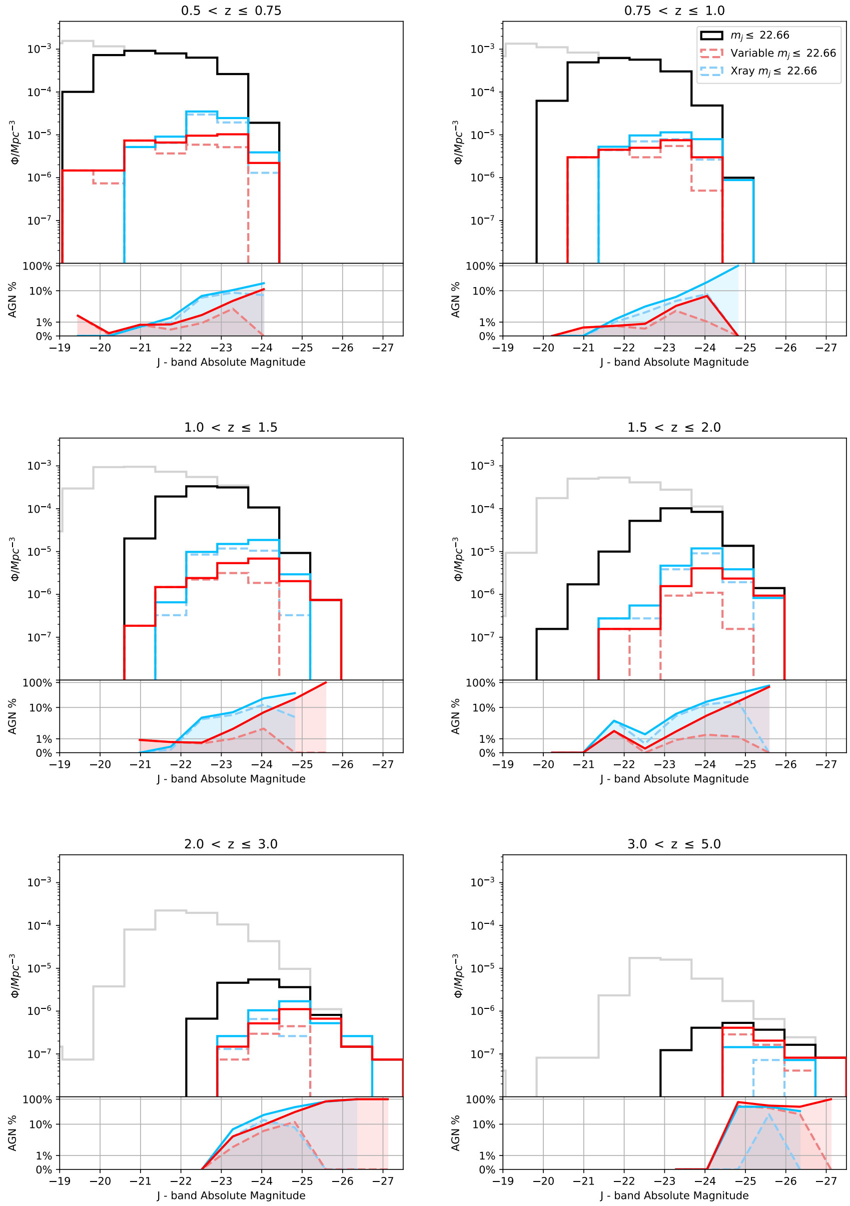

Figure 4.7: Luminosity functions as a function of redshift. The grey histogram represents the luminosity distribution for all galaxies within the field, while the black histogram shows the same but for galaxies with J-band apparent magnitudes $m_J \leq 22.66$. The solid red and blue histograms are as the black but only shows variability and X-ray detected active galaxies, respectively. Lighter coloured, dashed histograms show the active galaxy luminosity functions with quasars removed. X-ray detections were calculated using galaxies from the X-UDS imaging region and scaled to match the variability detected galaxies. The corresponding coloured distributions below each luminosity function shows the percentage of AGN for that redshift bin as a function of decreasing J-band absolute magnitude.

to lie within the contour formed by the inactive galaxies. Applying this cut to the data removes 75 (12%) of the variable AGN from the sample, 35 (5%) of the X-ray AGN and 55 (51%) of the dual-detected AGN. Using the remaining galaxies, we generate the stellar mass functions shown in Figure 4.6. Here the grey line shows the mass function for all galaxies in the data and the solid black line shows the population of galaxies with $m_J \leq 22.66$. As discussed in Section 3.4, this magnitude limit ensures that a variability of 20% or higher will be consistently detectable for all galaxies.

With the quasars removed, we find that the fraction of galaxies with X-ray detected AGN increases with increasing stellar mass of the host galaxy, whereas the detection rate of NIR variable AGN is largely flat, remaining on the order of $\sim$ 1% of galaxies regardless of the stellar mass of the host. This difference is consistent up to $z \approx 2$, where enough galaxies above the mass completeness limit are present to draw reasonable conclusions. We conclude that, across a broad redshift range, NIR variability allows for the identification of AGN in much lower mass host galaxies compared to X-ray selection.

4.3.3 Luminosity functions

In this section we investigate the luminosity functions of objects derived from the two methods of AGN detection, without applying any quasar filtering. This will provide a check on the influence of AGN light on the derived properties of these objects, which will be particularly significant in future situations where we may lack the range of spectral data and spatial resolution required to filter out quasars. In Figure 4.7, we plot the J-band absolute magnitude as a function of redshift for the detected active galaxies.

Here, we find that both methods detect much more similar distributions of objects, with the fraction of AGN increasing with luminosity whichever technique is used. This increase reflects the fact that the luminosity functions are strongly influenced by the contribution of AGN light, with brighter AGN more likely to be detected by either method. Without the auxiliary information we have employed in this work, it is not possible to reliably disentangle host galaxy and AGN properties from such data.

4.4 Conclusions

In this study, we use the long-term near-infrared variability of objects seen in the UKIDSS Ultra Deep Survey as an alternative approach to finding active galactic nuclei. We then compare the sample of AGN revealed in this way to those found using a more conventional X-ray-based method in the same field.

We find that the variability approach detects a distinct population of AGN, with an overlap of only 37 per cent between the two samples. An analysis of the X-ray-to-optical luminosity ratio finds the IR-variable AGN appear relatively X-ray quiet. Whether these AGN are intrinsically X-ray faint or heavily obscured is unclear, and will be the subject of future study.

After excluding quasar-like objects, whose AGN brightness means that we cannot reliably measure properties of the underlying host galaxy, we find that IR variability systematically detects AGN in galaxies with lower stellar masses than X-ray-detected objects. Comparing their mass functions, we find that IR-variable AGN are hosted in $\sim 1\%$ of galaxies of any mass, whereas the percentage of X-ray AGN detected strongly increases with increasing stellar mass of the host galaxy. This distinction seems to be independent of redshift out to the $z \sim 2$ probed by these data. One plausible explanation for the difference would be related to extinction: if low-mass hosts tend to systematically contain more heavily obscured nuclei, that might explain why AGN in such galaxies are more readily detected by their infrared variability than by their extincted X-ray emission. In future work we will explore the dependence of variability on redshift and hence on rest-frame waveband, to explore the implications for the origin of the AGN emission.

In seeking such physical explanations, we need to be able to reliably to separate AGN and host properties. The significance of the contribution of AGN light to distorting our understanding of their host galaxies is underlined by the rather different results we obtain by simply studying their luminosity functions, in which a higher fraction of AGN is found in more luminous objects, whichever method is used to identify them. This distinction arises from the fact that the luminosity function, particularly when including quasar-like objects, reflects the properties of the AGN as well as their hosts. Clearly, some care is needed in interpreting such composite data, and additional spectral and spatial information is vital.

These results indicate that multiple approaches to AGN detection are required to obtain a complete census of such objects. With upcoming deep, wide-field surveys such as EUCLID and LSST, which will be obtained over extended periods, long-term variability offers an important approach to identifying AGN missed by other methods, which is key to a more detailed understanding of the prevalence of these objects and their role in galaxy evolution.

Chapter 5

Investigating the origin of infrared variability in AGN

In this chapter we investigate how the properties of active galaxies vary depending on the waveband in which they are detected as being significantly variable. Following this investigation, we suggest possible explanations for these observations.

5.1 Introduction

Infrared (IR) emission has been observed in active galaxies since the late 1960's (Pacholczyk & Wisniewski 1967; Low & Kleinmann 1968), and these detections sparked interest into how the radiation is generated in this regime. As discussed in Section 1.4, there is a paucity of research into the IR variability properties of active galaxies compared to shorter wavelengths, most likely due to the time required for IR variability occur. However observations in these wavelengths have the potential to reveal much information about these systems. Before conclusions can be drawn from IR variability studies however, one must ascertain how IR emission is produced, as the production method implies different underlying physical structures within the AGN system.

Infrared emission can generally be split into three regimes, the far, mid and near-infrared (FIR, MIR, NIR), and it is likely different emission mechanisms dominate in each. In addition to observations of this radiation, the two main contenders for generating infrared radiation are thermal and non-thermal emission processes. Thermal radiation arises when the emitting particles do so because of the energy they have gained through their temperature, whereas the energy produced in non-thermal emission has no dependence on the temperature of the particles. Since non-thermal emission does not require the heating of a body, in theory a single production mechanism could generate the broadband radiation seen in active galaxies, leading to a simpler view of the AGN structure.

There have been few attempts to investigate the entirety of the IR spectrum in active galaxies, but Sanders et al. (1989) did attempt such a synthesis. These authors measured the 0.3nm to 6cm continuum of 109 quasars which included a mix of radio-quiet and radio-loud objects. They suggest that the NIR emission arises from an inner part of a dusty disk heated by the broad line region in the AGN, and that MIR - FIR radiation is due to the outer edges of the dusty disk re-radiating light emitted directly from the central source. They also found no dependence on the IR radiation with the radio power of the galaxy, concluding that non-thermal emission processes are only required for X-ray and radio emission in active galaxies.

Barvainis (1987) studied a similar wavelength range, fitting emission models to the 1μm-100μm spectrum of two radio loud quasars. Though they find the best fitting model requires thermal and non-thermal components, they state the near and MIR radiation generation is dominated by thermal processes, attributed to hot and cooler dust respectively, re-radiating light from a central non-thermal source. Following this conclusion, the authors were able to a build dust-heating model that can reproduce near and MIR spectra of active galaxies based on a ring of material heated by the central AGN radiation. This model is consistent with models produced by Rees et al. (1969), who were able to recreate the observed 2.2μm - 22μm spectra of Seyfert galaxies via a dust-heating model. By simulating dust grains heated by a nuclear source, they found they were able to recreate the observed power-law spectrum as well as predict the variability timescale for the near and MIR based on the evaporation temperatures of the dust. A ring of dusty material is required in both pieces of research for thermal emission to be viable; however an absence of this structure does not impact non-thermal models.

In contrast to the thermal scenario, other studies have concluded that near to MIR AGN radiation is produced non-thermally. Elvis et al. (1986), for example, were able to fit a single power law to the X-ray to infrared spectral energy distribution (SED) of the quasars studied in their sample. Their infrared emission extends to 10μm, and they argued that an AGN is comprised of a single, nuclear, non-thermal production component for X-rays to IR radiation, as it is unlikely that multiple interacting emission mechanisms would fit the same overall power law. Similarly, Cleary et al. (2007) ruled in favour of non-thermal emission processes when fitting both dust (thermal) and synchrotron (non-thermal) models to radio-loud quasars. They considered the mid to FIR wavelengths $\geq 15\mu$m, where they found their fits to be dominated by the non-thermal components. Due to the results of their models, they concluded that mid-infrared to radio emission was produced in the jets and lobes of active galaxies. Whilst both of these pieces of research favour non-thermal radiation scenarios, the AGN structure models they suggest are very different from each other, illustrating the uncertainty in the range of possible structures that AGN could contain.

Outside of simulations, direct observations of the near, mid and far-infrared continuum in AGN have also favoured a thermal emission scenario. One of the first reviews on the topic is presented in Rieke (1978), where the IR measurements for 53 Seyfert galaxies from ~1-10μm is collated from various sources. This review concludes that the IR is made up of re-radiated light from dust in a disk about the central engine. Likewise, in reporting on the mid to far-IR (24μm and 70μm) photometry of 20 radio-loud quasars Shi et al. (2005) found a majority of the far-infrared radiation originated from dust heated by the AGN and star formation within the active galaxy, with the AGN being the dominant heating source. Dicken et al. (2009) also studied the mid and FIR, 24μm and 70μm spectrum of 46 active galaxies. They quote the heating of circumnuclear dust as being the primary emission mechanism for the infrared radiation in the systems, as well as ruling out non-thermal synchrotron contamination as a potential source of infrared radiation in active galaxies.

Analysing photometric and spectral data has provided mixed results in determining what drives infrared emission in both thermal and non-thermal scenarios, but other approaches have also been used to characterise this radiation. If a single, non-thermal source produces the broadband emission observed in an AGN, then the NIR flux should vary on the same hour timescale observed in the X-rays. To test this hypothesis, 2.2μm variability was measured in Hunt et al. (1994) for 9 Seyfert galaxies known to be highly variable in the X-rays. Through this research, no short timescale variations typical of non-thermal emission was observed in the IR measurements, resulting in the conclusion that the NIR emission is dominated by slowly-varying reprocessed light.

Finally, Rieke & Lebofsky (1981) examined the X-ray, UV, optical and infrared continuum of NGC 4151, one of the six original Seyfert galaxies (Seyfert, 1943), where they fit multiple components to the spectrum of the galaxy to derive a comprehensive view of the nucleus. The polarisation of the NIR, 1μm - 4μm radiation was found to be negligible in this galaxy, which argues strongly against non-thermal emission, and they concluded that it was more likely that infrared emission arose from dust heated by a non-thermal source.

Though it is now accepted that AGN emission varies in flux in every band it has been observed in (Section 1.4), very few variability studies have been completed on the origin of infrared emission in active galaxies. Though Hunt et al. (1994) ruled in favour of the thermal scenario, their research was limited to a small galaxy sample with light curves that are not well sampled. Infrared variability was also measured in Clavel et al. (1989), where the far-UV, optical and infrared variability of the active galaxy Fairall 9 is studied. They found that the nature of the variability changed with wavelength, with the optical and J-band variability to be seemingly diluted by starlight, but otherwise in phase with UV variability measurements. Variations at longer wavelengths, such as the K and L-bands, however, were noticeably out of phase with measured fluctuations in the bluer bands, and this difference in behaviour between observing filters identified a possible turnover in emission mechanisms between the rest-frame J and K bands in active galaxies.

In this chapter, we investigate the properties of 601 active galactic nuclei at redshifts between $0 < z \leq 5$, selected through long-term near-infrared variability in the J (1.2μm) and K-bands (2.2μm). We compare the rest-frame features of the galaxies to each other as well as to a sample of X-ray selected AGN split by hardness ratio as a diagnostic of obscuration. From these measurements and comparisons, we determine if AGN that are significantly variable in the K-band show features consistent with emission from the thermal re-radiation of bluer light by dust, and we investigate if these same features are present in AGN selected in the J-band.

5.2 Variability dependence on wavelength

We begin by investigating how the variability amplitude of the active galaxies changes with wavelength. To answer this question, we plot the variability amplitude in the J-band (σ_J) against the K-band value (σ_K) in Figure 5.1. Here amplitudes are calculated from light curves with flux measurements taken on yearly timescales, and galaxies are split by the photometric band in which the AGN were selected as being significantly variable.

We first find that all the galaxies show a positive correlation in σ_J and σ_K, regardless of the band the AGN was selected in. However clear differences in the chromatic nature of the AGN becomes apparent when splitting the measurements by the detection band. AGN selected in the J-band show enhanced variability in the bluer, J-band compared to the K-band. This anti-correlation of variability amplitude with wavelength is in agreement with previous work in the UV (Paltani & Courvoisier, 1994) and the optical (Cid Fernandes et al. 1996, Berk et al. 2004, MacLeod et al. 2010, Zuo et al. 2012). Measurements for K-band selected AGN contrast this however, with larger fractional variability being measured in the redder K-band.

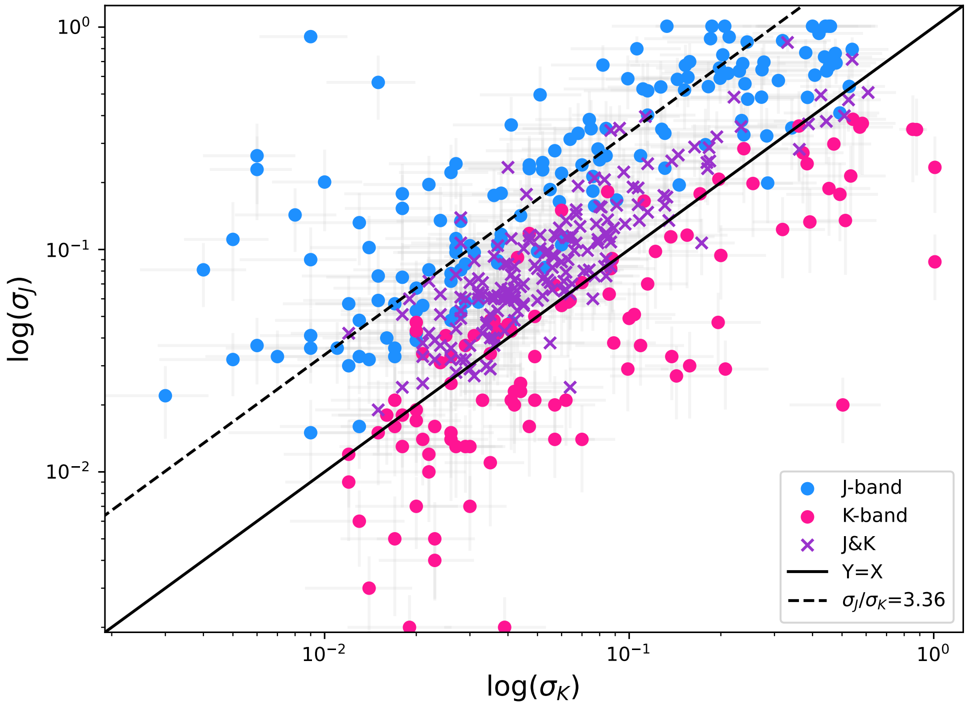

Figure 5.1: J vs K-band variability amplitude for variability detected AGN. AGN are split by detection band with blue dots showing AGN variable in the J-band only, pink dots showing K-band only variables and purple crosses denoting dual-band detected AGN. The solid black line shows unity and the black dashed line is the expect variability ratio of 3.36 based on the modeled IR variability spectrum in Meusinger et al. 2011.

The result that K and J-band selected active galaxies show opposite correlations with wavelength could be due to selection bias, as one would expect the variability amplitude to be larger in the detection band. Inspecting dual-band detected active galaxies (AGN measured as being significantly variable in both the J and K-photometric bands), also finds the sample to anti-correlate wavelength and variability amplitude, however differing detection limits in the J and K-band imaging could still bias the results seen in these galaxies. Instead, we make the same comparison for the X-ray AGN. The detection of these AGN is not dependent on variability, and as such breaks the degeneracy of the amplitude measurement with detection band, allowing for an intrinsic study of the chromatic nature of variability in AGN. Inspecting these measurements in Figure 5.2 finds X-ray AGN to largely anti-correlate wavelength and variability amplitude, in agreement with previous UV-based analysis.

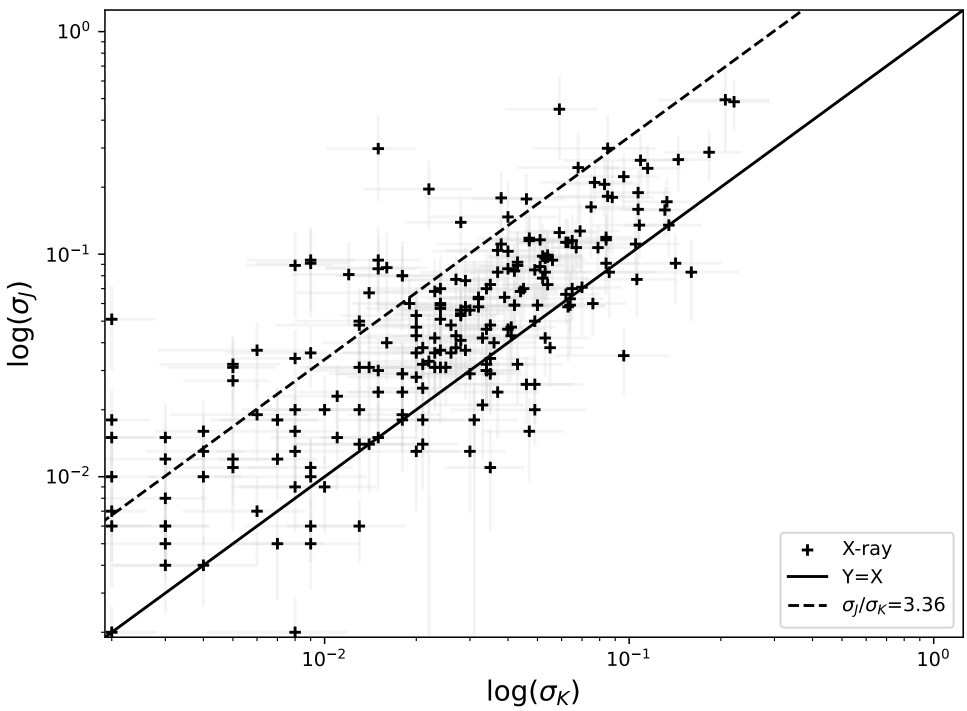

Figure 5.2: J vs K-band variability amplitude for all X-ray detected AGN. Grey lines show 1σ errors, the solid black line shows unity and the black dashed line is the expect variability ratio of 3.36 based on the modeled IR variability spectrum in Meusinger et al. 2011.

5.2.1 Infrared variability spectrum

In Meusinger et al. (2011), the AGN variability spectrum between 0.1μm - 0.8μm is found to change as

$$\sigma_\lambda \propto \lambda^{-2}, \tag{5.1}$$

where λ is the wavelength and σ_λ is the variability amplitude measured at wavelength λ. Applying this relation, we find the expected J to K amplitude ratio to be $\sigma_J/\sigma_K \approx$3.36. This value is plotted in Figures 5.1 and 5.2, and predicts that a given, unobscured AGN should be more variable in the J-band than the K-band. In Figure 5.1, the J-band detected AGN largely lie along the 3.36 line, whereas the AGN only variable in the K-band have a much lower ratio and dual-band detected AGN generally fall in the middle of these two groups. In Figure 5.2 it can be seen that the X-ray AGN show a larger spread in their amplitude ratio measurements, however the bulk of the distribution follows the dual-band detected AGN, lying between the model expected value and unity. Inspecting where the values measured in this study lie in comparison to the predicted value finds differences when splitting the variability detected AGN by detection band, with it appearing that the more significant the K-band variability is, the further the σ_J/σ_K ratio lies from the model expectation.

These results show that AGN variable in the J-band only are clearly different from AGN variable in the K-band only. The properties of the X-ray and dual-band selected samples provide evidence that these differences cannot be explained by selection bias in the AGN and as such, it is more likely that the positive correlation of σ_K and wavelength for K-band detected AGN is due to some physical processes in the system that does not occur in the J-band detected sample.

5.3 Origin of Variability in AGN

After determining that splitting the variable AGN by detection band gives opposite correlations of wavelength and variability amplitude (Section 5.2), we next aim to investigate if the underlying origin of the variability is different for a given detection band. To search for where variability is generated, we examine the rest-frame (RF) emission of the 601 variability detected active galaxies by plotting the ratio of the measured K to J-band variability amplitude vs redshift in Figure 5.3. Once again, samples are split by the photometric band they are classed as significantly variable in.

As found in Section 5.2, AGN that are variable in the J-band only best follow the simulated variability expected in AGN (Meusinger et al., 2011), showing little evolution with redshift and largely lying along the predicted ratio of $\sigma_K/\sigma_J \approx 0.3$. Additionally, dual band detected AGN have a similar flat distribution with redshift, but are consistently offset from the model value, with larger values of σ_K/σ_J for all epochs studied. In Figure 5.4 we reproduce Figure 5.3 and overlay the X-ray AGN, which have no waveband dependent selection bias in their detection. Inspecting this figure, we find the bulk of the X-ray population to follow a similar distribution to the dual-band detected AGN, with values that are positively offset from the model. However we note they do show a spread in σ_K/σ_J overall, with both large and low values over cosmic time. The AGN

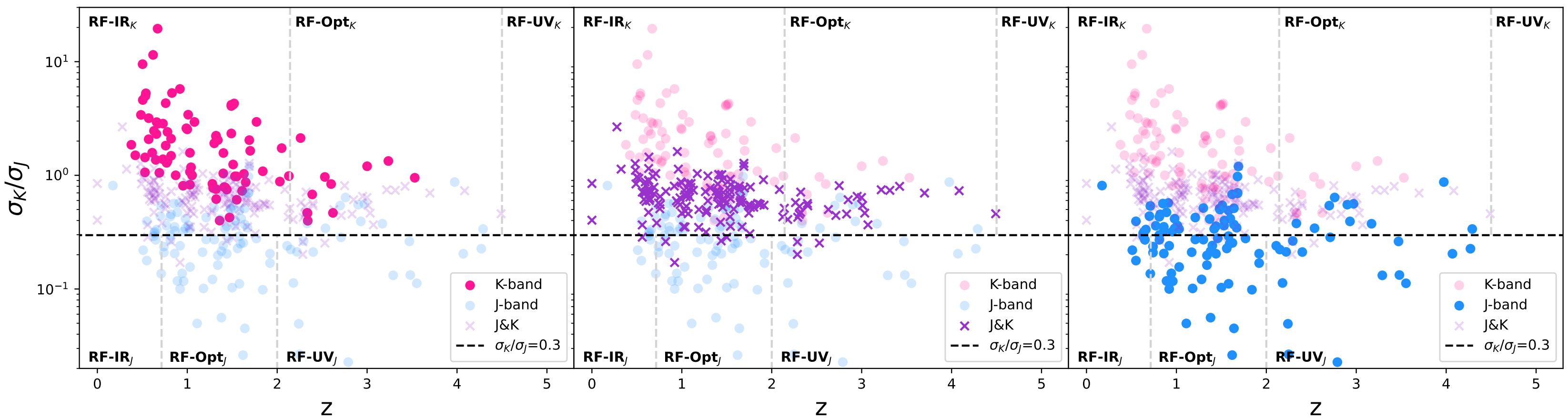

Figure 5.3: Ratio of K to J-band variability amplitude vs redshift for variability detected active galaxies. Pink dots show K-band only detect active galaxies, purple crosses show dual band detected active galaxies and blue dots show J-band only detected active galaxies. Horizontal dashed grey line shows the model variability ratio of 0.3 as calculated according to the variability spectrum in Meusinger et al. 2011. Vertical dashed light-grey lines denote the rest-frame emission ranges for the K and J-band above and below the Y=0.3 line respectively.

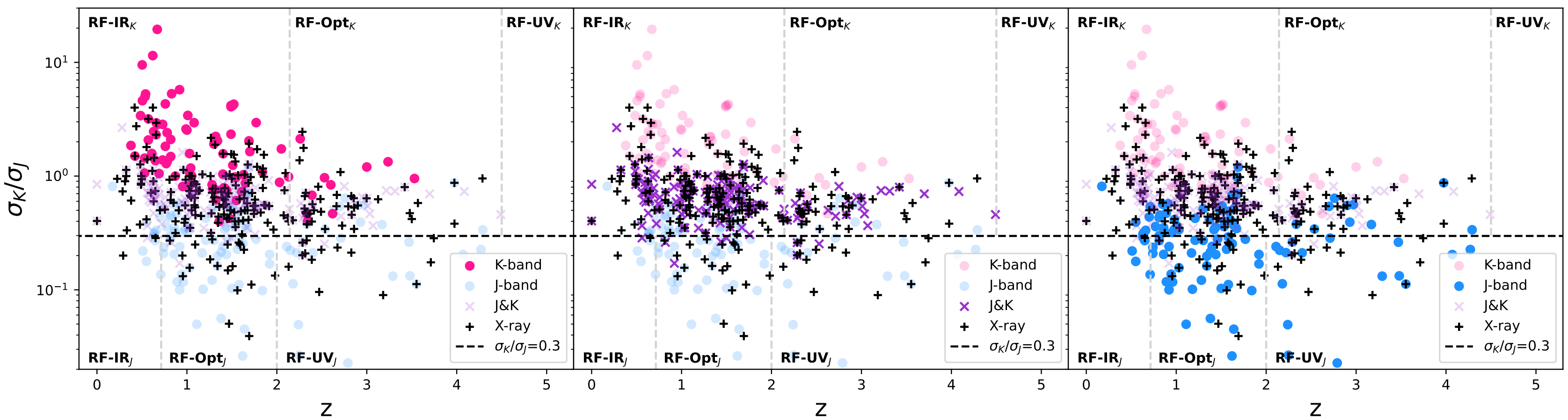

Figure 5.4: Ratio of K to J-band variability amplitude vs redshift for variability detected active galaxies. Pink dots show K-band only detect active galaxies, purple crosses show dual band detected active galaxies, blue dots show J-band only detected active galaxies and black crosses show X-ray AGN. Horizontal dashed grey line shows the model variability ratio of 0.3 as calculated according to the variability spectrum in Meusinger et al. 2011. Vertical dashed light-grey lines denote the rest-frame emission ranges for the K and J-band above and below the Y=0.3 line respectively.

variable in the K-band have the most unique behaviour of the active galaxies considered in this study. They show the highest σ_K/σ_J of any group as well as a clear decrease in the ratio with increasing redshift. Additionally, most K-band only detections are found at RF-IR redshifts where J and dual-band detections show no obvious preference for the rest-frame of the emission.

To explain the differences observed, we suggest a mix of effects. Examining the K-band variables (pink points in Figure 5.3) that are observed in the RF-infrared, the large σ_K/σ_J values observed in the galaxies could be due to lower measured values of σ_J than expected, higher measured values of σ_K than expected or a mix of both impacting the measurements. Generally, in the NIR, AGN are fainter than the emission observed from their host galaxy, but they are also bluer in colour compared to the colour of the host galaxy. Therefore, it is expected that the host galaxy would have a larger contribution to the overall measured flux for redder wavelengths, in this case the K-band, leading to lower fractional variability amplitudes in this band. In bluer (J-band) wavelengths however, the AGN would be more prominent, leading to higher fractional variability measurements in this band. Using this explanation alone, one would expect a given AGN to be more variable in the bluer J-band, which is seen in AGN detected as variable in the J band as well as dual-band detected and X-ray bright AGN, but this is the opposite of what is observed for the low redshift AGN selected by their K-band variability (Figure 5.3).

One hypothesis is that the RF-IR detected, K-band variable AGN, exist in dusty galaxies. If dust-reprocessing of light was occurring in such galaxies, emission in bluer bands would be reprocessed by the dust to longer wavelengths, enhancing σ_K values and therefore increasing the σ_K/σ_J for these galaxies. This hypothesis is supported by the behaviour of the RF-optical detected, K-band variable AGN. Examining these galaxies in Figure 5.3, we first find there are very few of them compared to the dual-band detected or J-band detected AGN, which show no preference for the rest-frame of emission and detection quantity. The lack of K-band variable detection at redshifts that corresponds to RF-optical emission would occur if a majority of AGN variable in the K-band are truly dusty, as the light from these galaxies at high redshift would be reddened to wavelengths beyond the K-band and as such they would go undetected in this study. Consequently, it is plausible that the RF-optical, K-band variable AGN we do observed are not dusty. If this assumption is correct, dust reprocessing of bluer light would not occur in these galaxies. They host AGN that are more luminous and the host galaxy would appear fainter due to the known decrease of galaxy surface brightness with redshift (e.g. Calvi et al., 2014) culminating in σ_K/σ_J being closer to the model prediction, which is what is observed. From this, we suggest dust to be a plausible explanation for the differences in variability properties observed in AGN variable in the K-band.

This explanation is in agreement with the study of Seyfert galaxy Fairall 9 by Clavel et al. (1989). They found the K-band variability of the AGN to be out of phase with UV, optical and J-band variability measures. From these results, the authors interpreted K-band emission to probe thermal re-radiation of UV and optical emission from dust in an active galaxy, whereas J-band emission originates from the accretion disk of the AGN. It therefore appears that this explanation is more generally applicable than to just this single galaxy.

5.4 Spectral energy distribution analysis

To further test whether variability in the K-band preferentially detects dust-reprocessed light from AGN, we investigate the spectral energy distributions (SEDs) of the galaxies. We also introduce a comparative sample of active galaxies selected through X-ray emission and split these galaxies based on their hardness ratio (HR), as an independent measure of obscuration. In this research we consider X-ray soft galaxies (HR<0) to be less obscured and X-ray hard galaxies (HR≥0) to be more obscured.

5.4.1 Mass Matching

For a fair comparison of the SEDs of the active galaxies detected in different ways to be made, we begin by mass matching the sub-samples of variability detected (K and J-band detected) and X-ray selected (hard and soft) active galaxies. Galaxies are required to have stellar masses within 1% of each other (Fig. 5.5), taking the samples from 180 to 74 detections in the K-band and 239 to 83 J-band detections as well as 323 to 247 X-ray hard AGN and 387 to 262 X-ray soft AGN.

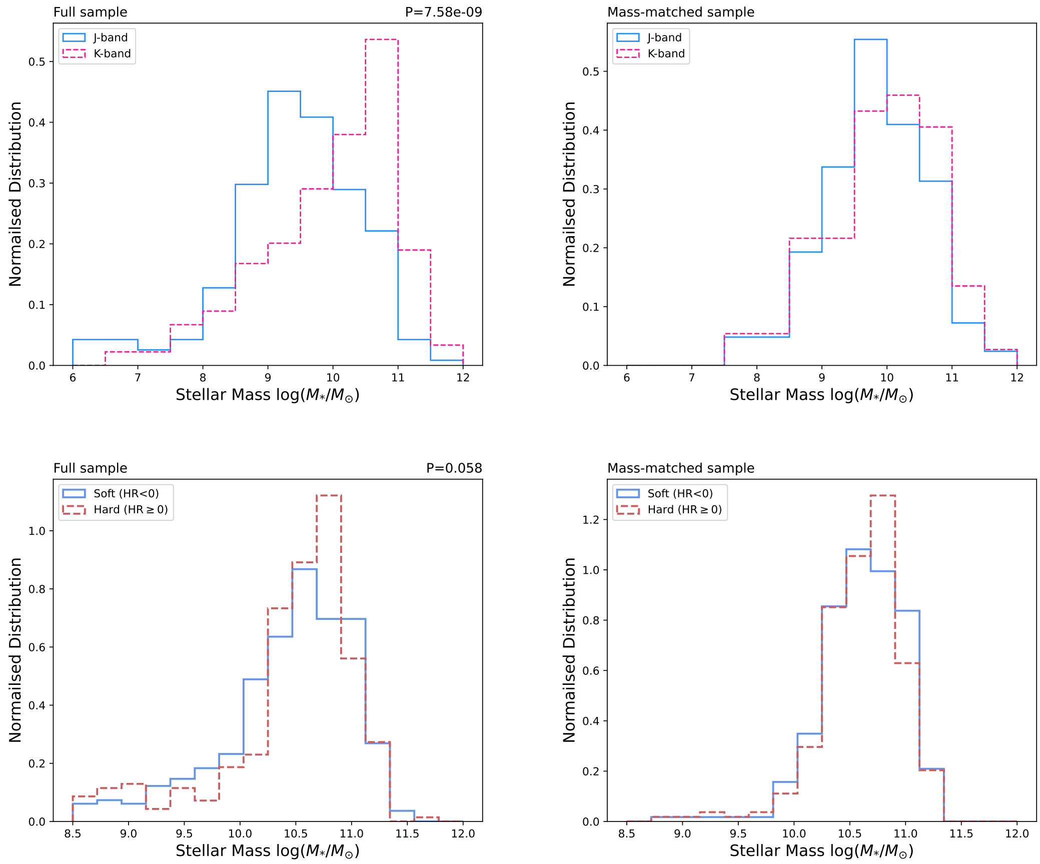

Figure 5.5: Stellar mass distributions of variability detected active galaxies split by detection band (top) and X-ray bright active galaxies split by hardness ratio (bottom). The left and right columns show the distribution prior to and after mass-matching respectively. Galaxy populations are mass matched within 1% of each other. In the top row, blue histograms shows the distribution for J-band detected active galaxies and the pink dashed histograms show the K-band detected active galaxies. In the bottom row the blue histograms shows X-ray soft active galaxies and the red dashed histograms shows the X-ray hard active galaxies.

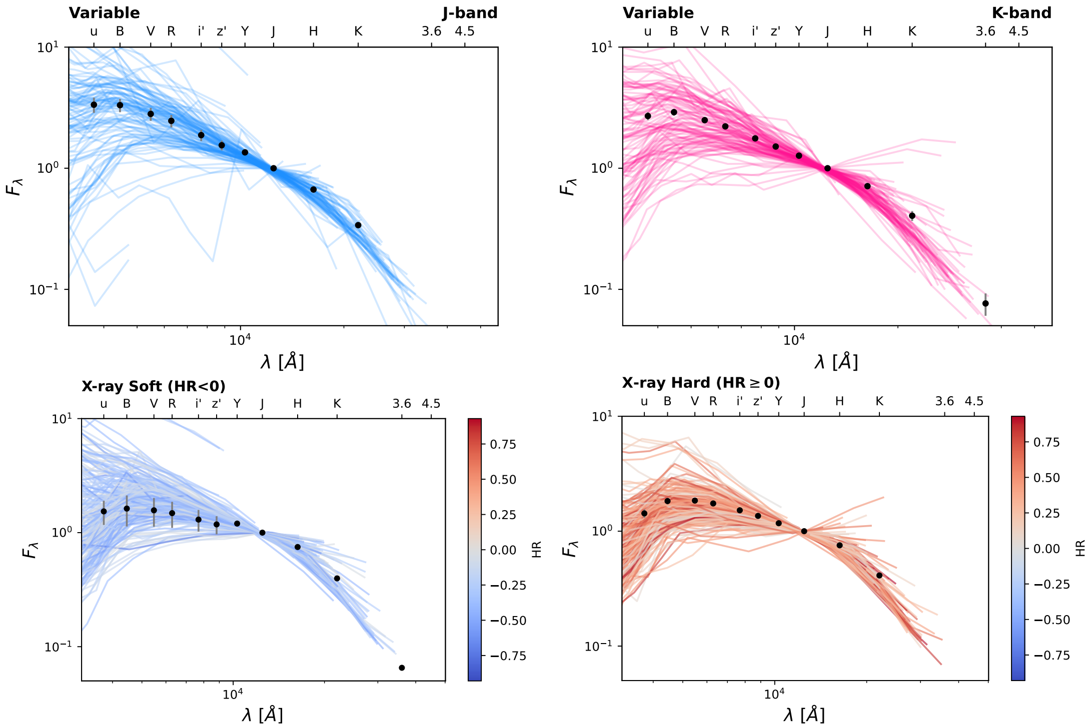

Figure 5.6: Rest-frame spectral energy distributions for the active galaxies studied in Section 5.4. In the top row, blue lines show active galaxies selected via J-band variability and pink lines show active galaxies selected in the K-band. The SEDs of X-ray detected active galaxies are split into X-ray soft (HR<0) and X-ray hard (HR≥0) samples, and colour coded by hardness ratio on the same scale. All SEDs are normalised to unity at the J-band wavelength (1.2μm) and have black points at each photometric band denoting the average flux density value at that wavelength, with the standard error on the mean being shown.

5.4.2 Calculating spectral energy distributions

To build spectral energy distributions for the galaxies (Figure 5.6), we take the 12 bands of photometry in the UDS (Chapter 2) and convert the measured AB magnitude values into flux densities (F_λ). We then shift the flux density measurements into the rest-frame based on the galaxy's redshift. For comparison, these rest-frame SEDs are then normalised to unity in the J-band, with rest-frame values of flux density calculated by interpolation at each of the 12 wavebands of the UDS photometry. These final flux density values are converted back into AB magnitudes where appropriate.

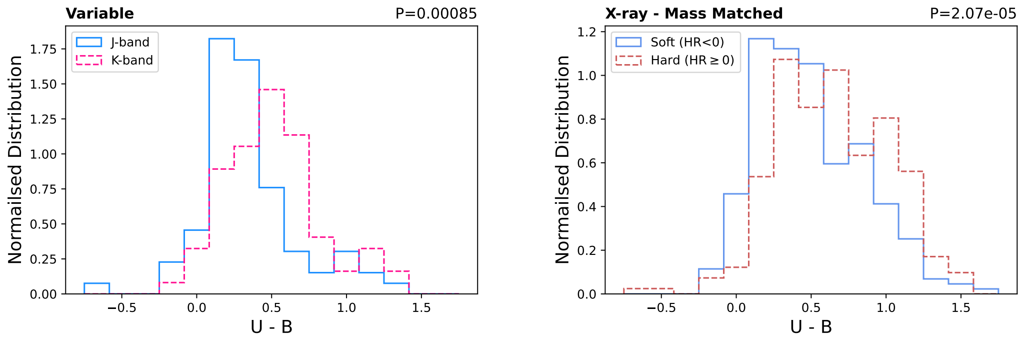

Figure 5.7: Rest frame U - B colour distribution for variability detected (left) and X-ray detected (right) active galaxies. For the variability detected sample, the blue histogram represents active galaxies selected as variable in the J-band only, and the pink dashed histogram shows galaxies selected as variable in the K-band. For the X-ray detected sample, galaxies are split based on their hardness ratio, with X-ray soft galaxies denoted by the blue histogram and X-ray hard galaxies shown as the red dashed histogram. Sub-samples in each plot are mass-matched within 1 per cent of each other. The P-values shown are from a Kolmogorov-Smirnov test between corresponding sub-samples, and confirms that the K-band selected and X-ray hard active galaxies have significantly different underlying distribution of U - B colour than the J-band selected and X-ray soft galaxies respectively.

5.4.3 SED comparison

As is apparent from Figure 5.6, we find the largest differences between SEDs in the ultraviolet, U-band. Furthermore, the different shapes of the SEDs is most apparent in the X-ray detected active galaxies, where X-ray soft galaxies show a range of U-band flux densities, but X-ray hard galaxies tend to be predominately faint in this filter. This difference can be quantified by comparing the U-B colour of the various classes of galaxy, with Figure 5.7 showing this comparison. As seen visually in the overall shape of the SEDs, the distribution of the U - B colour in the X-ray hard active galaxies is significantly redder compared to the X-ray soft active galaxies. Similar results are found for the J and K-band detected active galaxies, with the K-band detected sample having a redder U-B colour distribution compared to the J-band detected objects. For both comparisons, a Kolmogorov–Smirnov (KS) test confirms that samples are not drawn from the same underlying distribution, and we therefore conclude that variability in the infrared bands is in some physical way connected to the UV absorption of a galaxy.

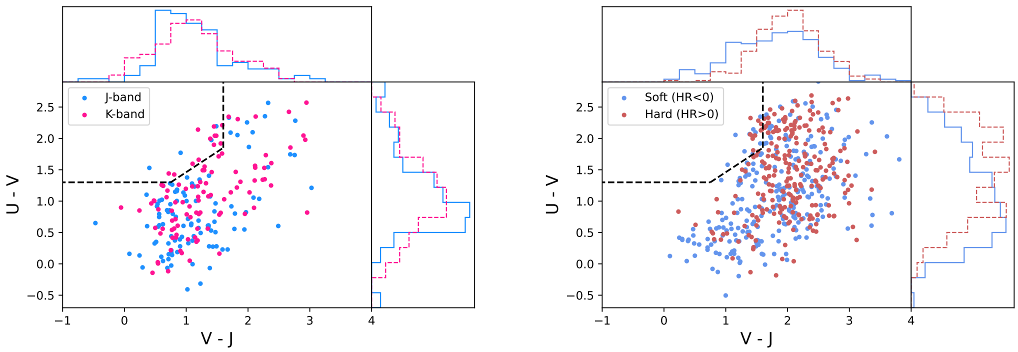

Figure 5.8: Rest-frame UVJ colour - colour diagram for mass-matched samples of variability detected (left) and X-ray detected (right) active galaxies. The black dashed line is as defined in Schreiber et al. 2015 and delineates quiescent galaxies from star-forming galaxies. Quiescent galaxies lie in the top left of the diagram. For the variability detected sample, blue points indicate J-band selected active galaxies and pink points show K-band selected active galaxies. In the X-ray detected sample, galaxies are split based on their hardness ratio, with X-ray soft galaxies shown as blue points and X-ray hard galaxies shown in red. In both plots, corresponding coloured histograms show the colour distribution.

5.5 Stellar Populations

In Section 5.4 we found that the detection band of the variable AGN is linked with the UV absorption of the active galaxy. However it is possible that differences in stellar populations drives the UV emission of the galaxies. To investigate this possibility, we plot the rest frame UVJ diagram of the galaxies in Figure 5.8. A UVJ colour-colour diagram is commonly used to separate out star-forming and quiescent galaxies (Wuyts et al., 2007), and we use the standard selection box as outlined in Williams et al. (2009) and Schreiber et al. (2015) to draw this delineation.

Inspecting this diagram, we find no evidence that the differences in UV emission in the active galaxies is due to differences in the fraction of passive galaxies between groups of active galaxies. A vast majority of all mass-matched galaxies lie within the star-forming region of the diagram, with the distributions of the matched K and J-band detected galaxies being statistically similar in both the U - V and V - J colours according to a KS test. X-ray hard galaxies however skew red in both U - V and V - J colours compared to X-ray soft galaxies, indicating dust reddening of the hard sample where red colours in U - V only would indicate a larger quenched fraction of galaxies (Williams et al., 2009). From this colour distribution we find that J and K-band variable host galaxies are generally star forming with similar amounts of dust reddening, and as such differences in star-forming and passive fractions of galaxies does not offer a plausible explanation for the relatively faint UV emission in K-band selected active galaxies.

5.6 Variability timescale

As reviewed in Section 5.1, more evidence has been found in favour of IR AGN spectra beyond $\sim 2\mu$m being generated via thermal re-radiation of optical and UV light by dust over blackbody emission from the accretion disk. We find differences in the chromatic nature of AGN variability amplitudes when splitting the active galaxies by selection band in Section 5.2, and model comparisons confirm that observed results cannot be explained by selection bias in the sample in Section 5.3. SED analysis reveals K-band variable AGN are systematically fainter in the UV compared to J-band variable AGN in Section 5.4 and a UVJ diagram confirms that the active galaxies have similar stellar populations regardless of detection method in Section 5.5. Combining these results, the properties of the K-band detected AGN seem to favour a hot dust-driven, thermal emission model over emission arising from the accretion disk, which is more consistent with the J-band detected sample.

To further test the hypothesis that K-band variability results from hot-dust emission processes, we now examine the timescale of the measured variability in the active galaxies. In addition to providing clues to the origin of the variability, quantifying the timescales on which variability takes place effectively measures the AGN power spectrum. Generally, AGN variability has been found to be dominated by long-term trends, which is commonly known as a red-noise spectrum (e.g. Lawrence et al. 1987; Uttley et al. 2014). Objects with blue-noise spectra behave in the opposite way, where variability on short timescales dominate the overall fluctuations seen in the object (as is seen, for example, in supernova events). As noted by Hunt et al. (1994), non-thermal, direct emission theory places no limit on the timescale of variability for a given wavelength. By contrast, thermal emission is dust-dependent and limited by the sublimation temperature and therefore orbital radius of the material, rendering variability on scales shorter than $\sim$1 month impossible.

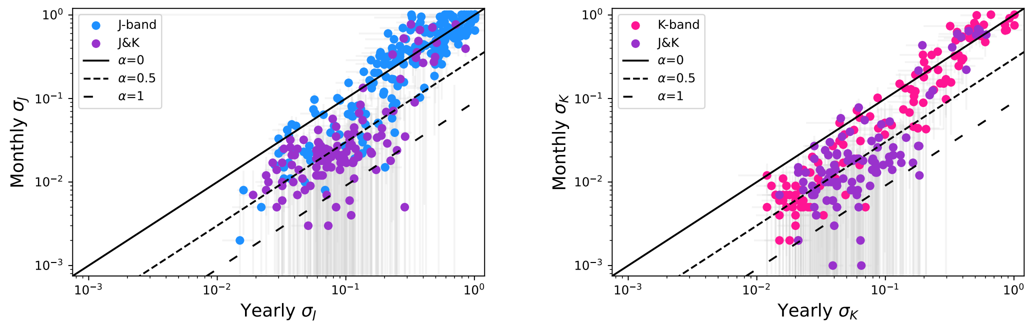

Figure 5.9: Modified, month-scale fractional variability amplitude vs year-scale variability amplitude for variability detected active galaxies. Measurements in the J-band are shown in the left plot and measurements in the K-band are shown on the right. J-band detected active galaxies are shown by blue points, K-band detected active galaxies are shown by pink points and active galaxies variable in both J and K photometric bands are shown as purple points, with light grey lines showing the errors on measurements. Several values for the spectral index, α, are over-plotted as lines on the diagram.

As described in detail in Almaini et al. (2000), the variability amplitude relates to the power spectrum as

$$\sigma^2 \propto f^{-\alpha}, \tag{5.2}$$

where σ is the AGN variability amplitude, f is the frequency in terms of variability timescale (*not* observed frequency of the light) and α is the power spectrum spectral index. Positive values of α result in a red-noise spectrum, negative values imply a blue noise spectrum and α=0 corresponds to white noise, where the variability in the object shows no dependence on timescale. To study the variability timescale of the AGN in this sample, we compare the fractional variability amplitude measured on year timescales to a modified fractional variability amplitude measured on month timescales, where year-scale/semester effects have been removed (see Section 3.5).

Inspecting Figure 5.9, we find the timescale on which variability takes place to be different for J and K-band variables. In all cases, the contribution from month timescales to the observed variability seems to correlate with the magnitude of the AGN fluctuations. AGN with the highest variability amplitudes show significant variability on both short and long timescales, with many appearing to have blue-noise spectra, but AGN with lower variability amplitudes are largely dominated by year-scale variations, consistent

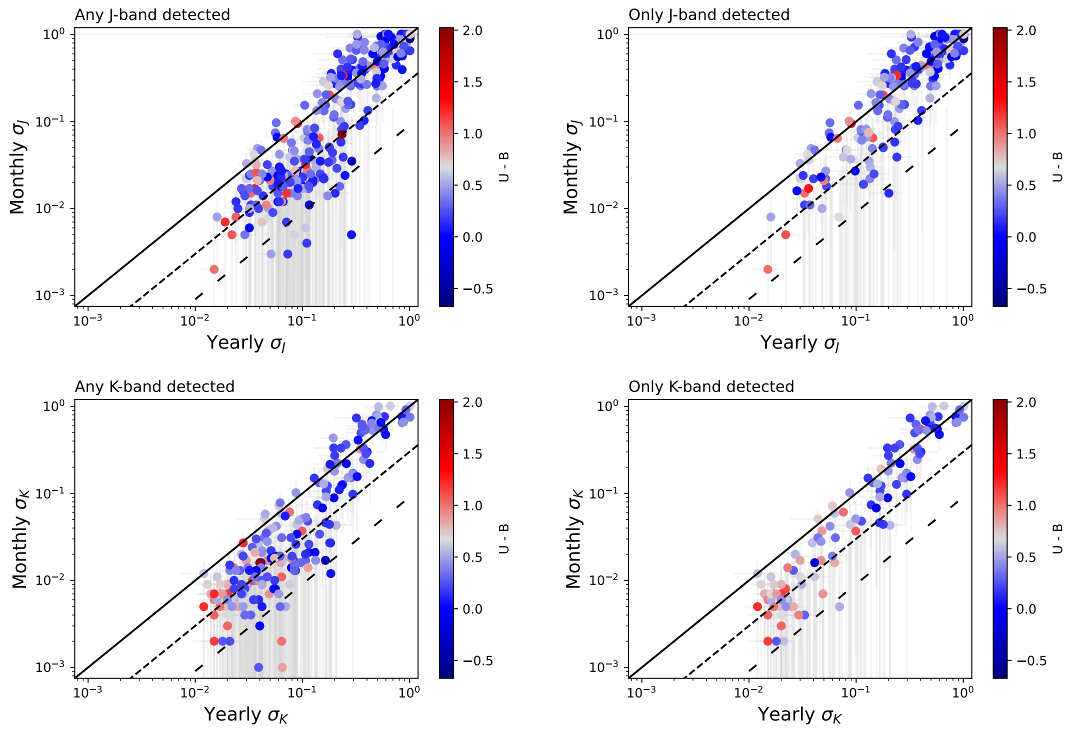

Figure 5.10: Modified, month-scale fractional variability amplitude vs semester variability amplitude for variability detected active galaxies. Measurements in the J-band are shown in the top row and measurements in the K-band are shown in the bottom row. The first column contains any galaxy detected as variable in the described photometric band and the second column shows galaxies only classed as variable in one band, with the AGN variable in both J and K-bands removed. Points are colour coded by the U - B colour and light grey lines show the errors on measurements. Black diagonal lines on the figure are the same as Figure 5.9, showing different values of the spectral index α.

with red-noise. A majority of the J-band sample lies in the high-amplitude area of the σ_{month}-σ_{year} plane, with a significant portion of AGN showing variability dominated by month-scale fluctuations. AGN variable in K-band however, show the opposite of this trend. These galaxies tend to have lower variability amplitudes, requiring several years of observations before variability can be observed. This result provides further evidence that variability in the J and K-bands are generated by different mechanisms, and the longer timescale distribution seen in the K-band implies that the flux generated in these galaxies originates from areas at larger radii than the J-band.

We also find the variability timescale distribution of the AGN links to other observed properties in the active galaxies. Taking the variability timescale comparison shown in Figure 5.9 and colour coding the points by the U - B colour seen in Figure 5.7 we produce

Figure 5.10. Here we find variability amplitude measurements anti-correlate with U - B colour in the K-band selected variable AGN. No such relationship is observed in J-band detected objects, and these results remain true when corresponding measurements from dual-band detected AGN are included. This result provides more evidence in favour of a dust-reprocessing scenario in the K-band detected objects, as higher levels of obscuration would lead to the redder colours, dilution in variability amplitude and variability skewing towards the longer timescales, as observed.

5.7 Conclusions

In this work, we investigate the properties of AGN selected using long-term near-infrared variability in the J (1.2μm) and K (2.2μm) photometric bands. We compare these active galaxies to each other as well as to a set of X-ray selected AGN, split by hardness ratio as a proxy for dust obscuration.

We first study how the measured variability amplitude (σ_λ) changes with wavelength in Figure 5.1. Here we find that in the J and dual-band detected samples, AGN are more variable in shorter wavelengths such that variability amplitude and wavelength are anti-correlated. These results are in agreement with previous optical and UV studies of AGN variability (Cid Fernandes et al. 1996, Berk et al. 2004, MacLeod et al. 2010, Zuo et al. 2012). Variability in AGN selected in the K-band however show the opposite trend; that is, the AGN are more variable in longer wavelengths, correlating variability amplitude and wavelength (Figure 5.1). To determine if these opposing results are intrinsic properties of the AGN, we investigate the nature of the variability amplitude in X-ray detected AGN (Figure 5.2). Despite begin detected in a different manner, X-ray bright AGN are found to anti-correlate variability with wavelength, providing evidence that the differences observed in the J and K-band detected AGN are not due to selection biases in the samples.

In Section 5.2.1, we investigate the AGN variability spectrum by comparing amplitude measurements split by detection band to the model spectrum presented in Meusinger et al. (2011). As shown in Figure 5.1, this model predicts that a given, unobscured AGN should be more variable in bluer bands, with the σ_J to σ_K amplitude ratio being ≈ 3.36. We find that AGN detected from J-band variability largely match this prediction, with the observed ratio in other AGN decreasing with increasing dominance of the K-band detection in the AGN. Selection bias may influence these results as it is expected that a given AGN would be more variable in the band it is detected in, but inspecting the same ratio measured in X-ray AGN (Figure 5.2) removes this issue, as detection by X-ray emission is independent of IR variability. Resulting measured variability ratios in these galaxies finds X-ray AGN to anti-correlate variability amplitude and wavelength, in agreement with dual-band detected and J-band variable AGN.

To determine why the AGN have different amplitude ratio distributions depending on the detection band, we investigated the rest-frame origin of measured variability in Figure 5.3. Here we find evidence that variability in different wavebands are generated in different ways, with J-band detections best fitting the accretion disk fluctuation model presented in Meusinger et al. (2011), having no preference for the rest-frame emission of the J-band flux as well as showing no evolution with redshift. Dual band detected AGN have similar properties, but are noticeably offset from the model-predicted σ_K/σ_J value, likely due to impact of K-band emission on the measurements. K-band detected AGN however, show significantly different features, with a majority of the galaxies originating at redshifts corresponding to RF-IR emission and σ_K/σ_J decreasing over cosmic time. These properties could be explained by dust obscuration as well as an increased prominence in the host galaxy emission at low redshift. Dusty, higher redshift objects however would have their intrinsic emission reddened beyond the K-band as well as preferentially observing more luminous AGN, reducing the relative host galaxy emission. Additionally, the minority of K-band detected AGN at RF-optical redshifts are found to have σ_K/σ_J similar to the model-predicted 0.3, which would occur if such objects were truly unobscured, AGN dominated systems. Again, bias in detection could also influence these results, however inspecting how the variability amplitude ratio evolves with cosmic time for X-ray detected galaxies in Figure 5.4 finds this sample to best follow the dual-band detected sample, implying the offsets seen in these galaxies are due to underlying properties within the systems.

We inspect the spectral energy distribution of the galaxies for signs that IR emission is due to thermal reprocessing of bluer light in the K-band detected galaxies in Section 5.4. Here, we take the sub-samples of active galaxies detected as variable in the J and K-band only, and mass-match them within 1 per cent of each other based on the measured stellar mass (Figure 5.5). In addition to this, we introduce a further, mass-matched, comparative sample of X-ray detected active galaxies, split by hardness ratio as a proxy for dust obscuration. Comparisons of the SEDs of these galaxies finds different levels of UV emission (Figure 5.6), with K-band detected active galaxies appearing redder in the U - B colour compared to J-band detections (Figure 5.7). Analogous results are found in the X-ray galaxies, which are an independent dataset due to their detection method and therefore do not suffer selection bias issues that may influence the variability detected sample. X-ray hard active galaxies having a redder U - B distribution compared to the X-ray soft galaxies. UVJ measurements also confirm these differences are not due to different passive fractions within the sub-samples of galaxies (Figure 5.8).

In Section 5.6 we investigate the variability timescale to see if dust obscuration is a likely explanation for the differing properties of the samples. We compare the year-scale variability amplitude to a modified month-scale variability amplitude, where semester/year effects have been removed (Figure 5.9). From this comparison, we find the J-band variable AGN tend to have larger variability amplitudes with significant variability being seen on both short and long timescales, an effect that is expected if variability in these objects arises from accretion disk fluctuations that propagate out through the system. In the K-band however, variability amplitudes are generally much lower, with fluctuations largely occurring on year-timescales. This behaviour supports the idea that K-band variability is generated further out from the core of the AGN compared to variability seen in J-band variable AGN.

Finally, Connecting the variability timescales to observed properties of the SEDs in Figure 5.10, an anti-correlation in amplitude and U - B colour is found in the K-band sample, but no correlation between UV colour and amplitude is observed in the J-detections, with equivalent measurements from dual-band variable AGN following the same trends. Likewise, these results are consistent with a dust-reprocessing scenario for the K-band variable AGN, where higher levels of dust contamination absorbs more UV light, diluting variability amplitudes in the process.

Overall, we conclude that splitting active galaxies found using long-term, near-infrared variability, by the detection band finds active galaxies with systematically different properties. We confirm that the correlation of variability amplitude and wavelength is opposite for J-band detected and K-band detected AGN and we find K-band variable active galaxies to be consistently fainter in the UV compared to galaxies variable in the J-band. The observed properties of K-band detected active galaxies suggest the IR spectrum is dominated by thermal emission from hot dust over other radiation processes. These results are consistent with the findings of Clavel et al. (1989), and therefore if the NIR spectrum of AGN can be attributed to a combination of hot dust and blackbody emission processes, hot dust reprocessing begins to dominate over accretion disk emission between the rest-frame J and rest-frame K-band.

Chapter 6

Nature vs nurture: The host galaxy and environmental properties of active galactic nuclei

6.1 Introduction

Throughout this thesis we have found that the properties of active galaxies are dependant on the detection method (Chapter 4) and AGN have different properties depending on the band they are significantly variable in (Chapter 5). What is not yet clear is what underlying driving force causes these differences. As stated in Section [Reference section of intro with BH - HG relations], observations of inactive galaxies have found many correlations between the properties of galactic black holes and their host galaxy, implying that the evolution of the two are linked. However, to be able to describe the evolution of active galaxies and how they differ from those of normal galaxies, a complete understanding of the both the AGN and host galaxy must be obtained.

In trying to understand active galaxies, much work has been done into separating out AGN and host galaxy emission in active galaxy observations. Detailed spectral fitting has proven to be a successful approach, with the technique being able to successfully determine the stellar properties (e.g. mass, age, star formation rate) in active galaxies (Kauffmann et al. 2003; Aird et al. 2012; Hainline et al. 2012; Mountrichas et al. 2022;

Georgantopoulos et al. 2023), calculate reliable AGN and dust-corrected magnitudes for host galaxies (Bongiorno et al. 2012; Rosario et al. 2015) as well as providing information on AGN luminosities and accretions rates (e.g López et al., 2023). However detailed spectral information is commonly needed for SED analysis to be effective and this approach does not provide physical properties such as galaxy morphology or size, which may be key to understanding the AGN process. Though detailed information on galaxy properties can be gained from SED analysis, other approaches must be used to determine morphological and environmental characteristics, especially if the goal is to efficiently detect active galaxies in a survey or ascertain possible triggering mechanisms for the phenomenon.

One of the defining characteristics of active galaxies is how they appear different compared to regular (inactive) galaxies, due to the impact of AGN emission on observations. As such, extensive research has been done to be able to understand the host galaxies of active systems, as this can give insight into why differences are found in active galaxies when they are grouped by detection mechanism. Previous research has determined host galaxy properties by fitting multi-component models to science imaging. Inskip et al. 2010, for example, used this method and found AGN hosts to predominantly be bulge-dominated systems, with ~50% of the galaxies showing disturbed structures indicative of mergers or interactions. Investigating an optically variable sample in Zhong et al. 2022, no preference for host morphology was found in the active galaxies, but the merger signature rate increased with SFR and AGN luminosity, implying the same gas and dust fuels both phenomena. Griffith & Stern 2010 found AGN detected by different methods have different host morphologies, with radio-loud AGN tending to be in early type galaxies but X-ray bright and MIR selected AGN showing a slight preference for disk type galaxies comparatively. Whilst these results give insight to the distribution of active galaxy morphology as well as touch on differences within different types of active galaxies, they do not contextualise these results in relation to how similar inactive galaxies behave in the wider Universe.

Gabor et al. 2009 and Fan et al. 2014 completed similar work in fitting 2D models to images of active galaxies, however these studies differ from those presented in Inskip et al. 2010, Zhong et al. 2022 or Griffith & Stern 2010 as both studies include a matched control group as a comparative sample. Here both authors report similar results, finding no enhancement of merger signatures in active systems relative to the controls, and conclude that major interactions are not a likely triggering mechanism for active galaxies. Likewise, Hewlett et al. 2017 finds that an overall comparison of active and control galaxies finds both groups to have similar merger rates for a given luminosity bin, however they do note that this is not consistent across cosmic time. The high redshift, active sample appear ~4 times more likely to be in mergers compared to control galaxies at similar redshifts, and this difference disappears once lower redshifts are probed resulting in the conclusion that mergers are a noticeable but non-dominant AGN fuelling mechanism. These results show that the possible conditions and fuelling mechanisms that trigger AGN activity is far from confirmed, and whilst AGN hosts themselves can have a range of morphologies, it is not known if this is an effect of AGN feedback in the galaxies, or the environment the galaxies exist in.

Research into the environment of active galaxies has found mixed results however, with many studies finding active galaxies to reside in overdense regions of the Universe compared to general field galaxies (Kauffmann et al. 2004; Hutchings et al. 2009; Falder et al. 2010), with the opposite being found to be true for active galaxies in cluster environments (Gisler 1978; Dressler et al. 1985; Popesso & Biviano 2006; Pimbblet et al. 2013; Rodríguez et al. 2022) possibly due to ram pressure striping induced strangulation, gas being too hot to collapse or high velocity dispersion meaning mergers are unlikely to occur. This is further complicated by studies finding no link to the incidence of active galaxy emission and environment at all (e.g. Miller et al., 2003), calling into question the extent that non-secular processes have on the triggering of AGN.

Furthermore, it is not only where active galaxies reside that must be considered when studying their environments but also the impact that AGN themselves have on their surroundings. AGN emission theory postulates that the radiation from active galactic nuclei could have profound effects on the local and global environment, with this feedback potentially resulting in enhanced star formation (Rosario et al. 2013; Zhong et al. 2022; Molina et al. 2023; Ferrara et al. 2023), the quenching of star formation (Hopkins et al. 2006; Schawinski et al. 2007; Fabian 2012; Lammers et al. 2023), or by having no impact of star formation rates at all (Aird et al. 2012; Bongiorno et al. 2012; Hainline et al. 2012; Ramasawmy et al. 2019). These studies serve to illustrate how little is confirmed about the interaction of AGN emission on the host galaxy and vice versa, and under what conditions these interactions occur.

In this research, we investigate to what extent AGN emission impacts galaxy observations within a given wide field survey. We compared the environment and physical parameters of X-ray bright and variability detected active galaxies to a set of control galaxies matched in stellar mass, redshift and effective radius. We also compare the properties of active galaxies selected by different techniques to each other to determine if the parameters of active galaxies change depending on the selection method employed. In addition to this we present preliminary work comparing the host galaxy properties of X-ray detected AGN to that of a matched set of inactive, control galaxies such that the properties of the galaxies AGN exist in can be studied.

6.2 Data and sample selection

In this research, we use both ground-based and space-based imaging of the Ultra Deep Field. In addition to the ground based data the UDS provides (see Chapter 2 for full details) we introduce the Cosmic Assembly Near-Infrared Deep Extragalactic Legacy Survey (CANDELS) survey. This survey was obtained using the Hubble Space Telescope and covers a smaller section of the wider, ground based UDS field with higher resolution imaging.

6.2.1 UKIDSS UDS field

For ground-based, UDS imaging, the active galaxies consist of the 601 variability detected AGN and 710 X-ray bright AGN found in Section 3.1. The variability detected active galaxies are found using the method described in Elmer et al. (2020), where significant variability in NIR light curves are identified based on a χ^2 analysis. X-ray bright active galaxies are selected based on matching the Chandra X-ray catalogue to UDS DR11 data.

We also select a set of inactive galaxies matched to the features of active galaxies to function as a control sample. We first remove any active galaxy from the UDS DR11, leaving 112,935 inactive galaxies to sample from. We then match these inactive galaxies to the active galaxies based on stellar mass (M_*), effective radius R_e and redshift z. For a given active galaxy, an inactive galaxy must have a stellar masses within 5% ($M_*^{control}$ $\pm$ 5%M_*^{active}), radius within 10% ($R_e^{control}$ $\pm$ 10%R_e^{active}) and redshift within 5% (1+z) ($z_{control}$ $\pm$ 5%(1+z_{active})) that of the active galaxy to be selected as a control in this study.

Applying this finds 4,336 control galaxies for the variability detected active galaxies and 4,614 control galaxies for the X-ray selected active galaxies. This criteria was selected as it ensures control galaxies have broadly similar properties to the active galaxies, whilst also allowing for a larger sample of controls compared to the active population such that any overall trends identified are intrinsic properties of the population and erroneous results due to noise are largely washed out.

6.2.2 CANDELS field

In addition to the ground-based UDS imaging, we have access to HST space-based imaging of a section of the Ultra Deep Field. The Cosmic Assembly Near-Infrared Deep Extragalactic Legacy Survey (CANDELS) survey consists of five fields:

- The Great Observatories Origins Deep Survey (GOODS)-North field
- The Great Observatories Origins Deep Survey (GOODS)-South field
- Cosmological Evolution Survey (COSMOS)
- Extended Groth Strip (EGS)
- The Ultra Deep Survey (UDS),

with a point source limiting magnitude of H = 27.7mag. Here we make use of the CANDELS UDS field, which covers a small area of the wider UKIDSS UDS field via the Hubble Space Telescope's Wide Field Camera 3 infrared channel (WFC3/IR) and WFC3 ultraviolet/optical channel, as well as The Advanced Camera for Surveys (ACS) (Grogin et al. 2011; Koekemoer et al. 2011). The CANDELS catalogue consists of 35,932 extended sources, which is matched to the *'best galaxies'* subset of the UDS DR11 (Section 2.1) where we recover 18,014 sources for use in this study.

When using imaging from this more limited area, samples of AGN drop from 601 to 48 variability detected AGN and 710 to 203 X-ray detected AGN. Again, controls for this sample were determined by matching inactive galaxies to active galaxies on stellar mass, radius and redshift; however we relax the selection criteria to: stellar mass within 10% ($M_*^{control} \pm 10\% M_*^{active}$), radius within 20% ($R_e^{control} \pm 20\% R_e^{active}$) and redshift within 20% (1+z) ($z_{control}$ ± 20%(1+z_{active})) that of the active galaxy to be selected as a control galaxy. This ensures a reasonable sample of comparison galaxies given the smaller imaging area. This results in 488 control galaxies matched to the 48 variability detected active galaxies, and the control sample for the 203 X-ray detected active galaxies contains 1,655 inactive galaxies.

6.3 Determining host galaxy parameters

In this research, we aim to investigate how AGN selected by different methods differ observationally from similar inactive galaxies. To do this we use magnitude measurements and structural parameters for ground-based UKIDSS UDS imaging which was measured in Almaini et al. 2017 using the GALAPAGOS (Barden et al., 2012) software. Details of the same data being measured on CANDELS HST imaging can be found in Maltby et al. 2018 and van der Wel et al. 2012, both of which used GALFIT. All studies fit Sérsic profiles to data, with Almaini et al. 2017 using ground based IR imaging taken in the K-band, Maltby et al. 2018 using optical imaging (I and V-band) and van der Wel et al. 2012 using J and K-band infrared imaging.

To be able to separate out AGN and host galaxy light in active galaxies such that host parameters can be determined, we use GALFITM (Häußler et al., 2013), which is a variant of the 2D fitting algorithm GALFIT (Peng et al. 2002; Peng et al. 2010) developed as part of the Measuring Galaxy Morphology (MEGAMORPH) project. GALFIT calculates a best-fit model to the surface brightness of a given galaxy by minimising the χ^2 of the fit, and GALFITM extends this functionality, allowing for the fitting of multiple science images in different wavebands simultaneously. Here we fit a Sérsic (Sersic, 1968) + Point Spread Function (PSF) models to HST ACS and WFC3 images in the V, I, J and H-bands. Empirical PSFs are used, with a full explanation of how they were constructed being found in Maltby et al. (2018). To summarise this process however, ~150 stars in the CANDELS-UDS region were isolated and 4×4”^{2} postage stamps of these stars were cut from the science images of the field. These images were normalised in flux and then stacked according to the median value. This process is repeated for all four of the WFC3 and ACS bands, with a final PSF being constructed for each corresponding filter.

Sérsic models are then convolved with a point spread function and compared to the original surface brightness distribution of the science image. Parameters from the Sérsic profile include:

- Effective radius in image pixels along the semi-major axis (R_e)
- Sérsic index (n)
- Axis ratio (semi-minor axis/semi-major axis; b/a)
- Position angle
- Apparent Magnitude

with the PSF model returning a magnitude. Both a combined Sérsic + PSF and singular Sérsic model are fit to all galaxies within this study; we explore how the inclusion of a PSF component in the fitting affects the measured results in active and inactive galaxies in the following sections.

6.4 Calculating environmental density

We also explore the wider environment of the galaxies in our sample to uncover if active galaxies reside in systematically different environments compared to inactive galaxies. As a measure of environment, aperture number densities for galaxies within the UDS are calculated using the technique described in Lani et al. 2013. For each galaxy, a cylindrical volume was constructed based on a 250kpc radius and a ±0.5Gyr "depth", which is characteristic of the typical errors in photometric redshift. Within this volume, the number of neighbouring galaxies with apparent K-band magnitudes below K = 25 (AB) were counted; this value was then normalised according to the expectation assuming a uniform distribution of galaxies, taking into account masking and the edges of the field, to give the value of relative density. This density, ρ_{250}, is the environmental density measure we make use of in this analysis, with values greater than one indicating an over-dense region and values less than one indicating an under-dense region (Taylor et al., 2023).

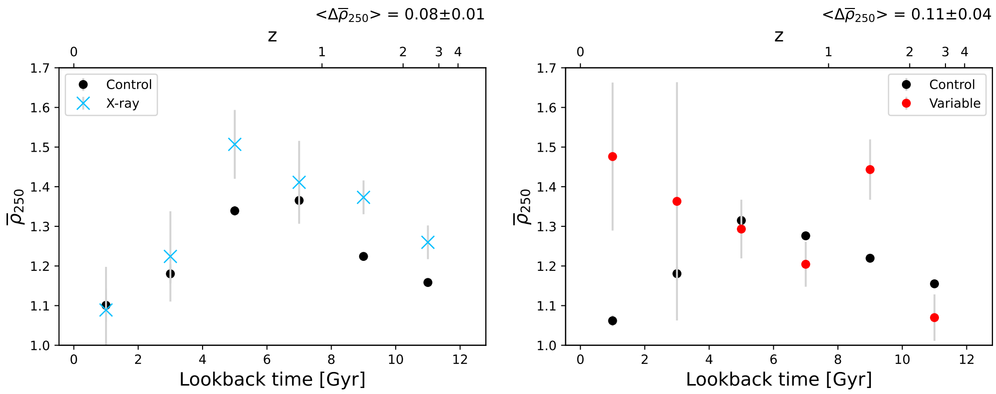

Figure 6.1: Average aperture number density ($\overline{\rho}_{250}$) vs look back time for X-ray detected active galaxies (left) and variability detected active galaxies (right). X-ray bright active galaxies are denoted by blue crosses, variability detected active galaxies are shown as red points and corresponding matched control galaxies are shown as black points. Galaxies are averaged in bins of 2Gyrs, with error bars in grey representing the standard error on the mean. Look back times are calculated based on the measured redshift and the cosmology quoted in the Introduction (Chapter 1) and corresponding redshifts are shown on the top x-axis of the plot. <$\Delta\overline{\rho}_{250}$> denotes the difference in the overall mean ρ_{250} for all epochs between the active galaxies and their corresponding control galaxies.

6.5 Results

6.5.1 Environment

To investigate if and how observations of active galaxies differ from inactive galaxies, we first examine the large scale properties by studying the environment the galaxies reside in. In Figure 6.1 we plot the aperture number density vs look back time for the X-ray bright and variability-detected active galaxies and corresponding matched control galaxies. Inspecting this figure, we find both X-ray bright and variability detected active galaxies are found in different environments compared to their matched control galaxies. In the X-ray sample, active and control galaxies follow similar distributions across cosmic time, but active galaxies are consistently found in denser environments compared to the control galaxies for all epochs studied. Active and control galaxies in the variability detected sample however show no obvious similarities in the evolution of their environment. Instead, the mean environmental density of the variability-detected galaxies decreases linearly with increasing look back time, whereas the matched control sample shows an evolution akin to the X-ray detected sample, with the average environmental density

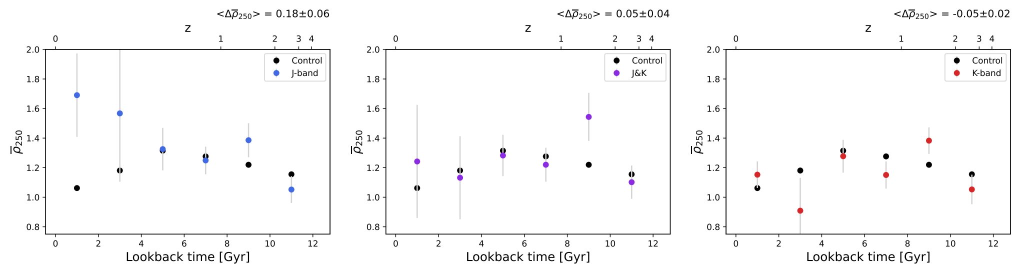

Figure 6.2: Average aperture number density ($\overline{\rho}_{250}$) vs look back time for variability detected active galaxies, split by detected band, and control galaxies. Active galaxies classed as significantly variable in the J-band are shown on the left as blue points, dual-band detected active galaxies are shown in the centre plot as purple points and active galaxies variable in the K-band only are shown on the right with red points. Control galaxies are matched to the overall variable population and are the same in all three subplots, denoted as black points. Galaxies are averaged in bins of 2Gyrs, with error bars being the standard error on the mean. Look back times are calculated based on redshift and corresponding redshifts are show on the top x-axis of the plot. $<\Delta\overline{\rho}_{250}>$ denotes the difference in the overall mean ρ_{250} for all epochs between the active galaxies and their corresponding control galaxies.

increasing until ~5Gyrs and then decreasing beyond this value.

As we found AGN properties to be dependant on detection method (Chapter 4), we look to further investigate the environmental evolution of the variability-detected active galaxies, as these have shown further differences depending on detection band (Chapter 5). We again plot the aperture number density versus look back time for the variable galaxies, but we now split the active galaxies into groups based on the band they were found to be significantly variable in. Exploring this in Figure 6.2, we first find that the overall shape of the distribution seen in Figure 6.1 is dominated by the AGN variable in the J-band only. This group shows the same linear decrease of environmental density with look back time and is the only sample where galaxies are in much higher density environments compared to the controls in the lowest look back bins. The evolution of the environment in dual-band detected and K-band variable active galaxies, by contrast, are much more similar to the control galaxies. On average, the dual-band detected galaxies are in slightly denser environments and the K-band detected galaxies are found in slightly under-dense regions, however both groups show large overlaps with the control galaxies across cosmic time. Combining these results with those found for the overall populations, we confirm that AGN found using different methods show clear differences in the regions of space they reside in. However active galaxies as a whole seem to

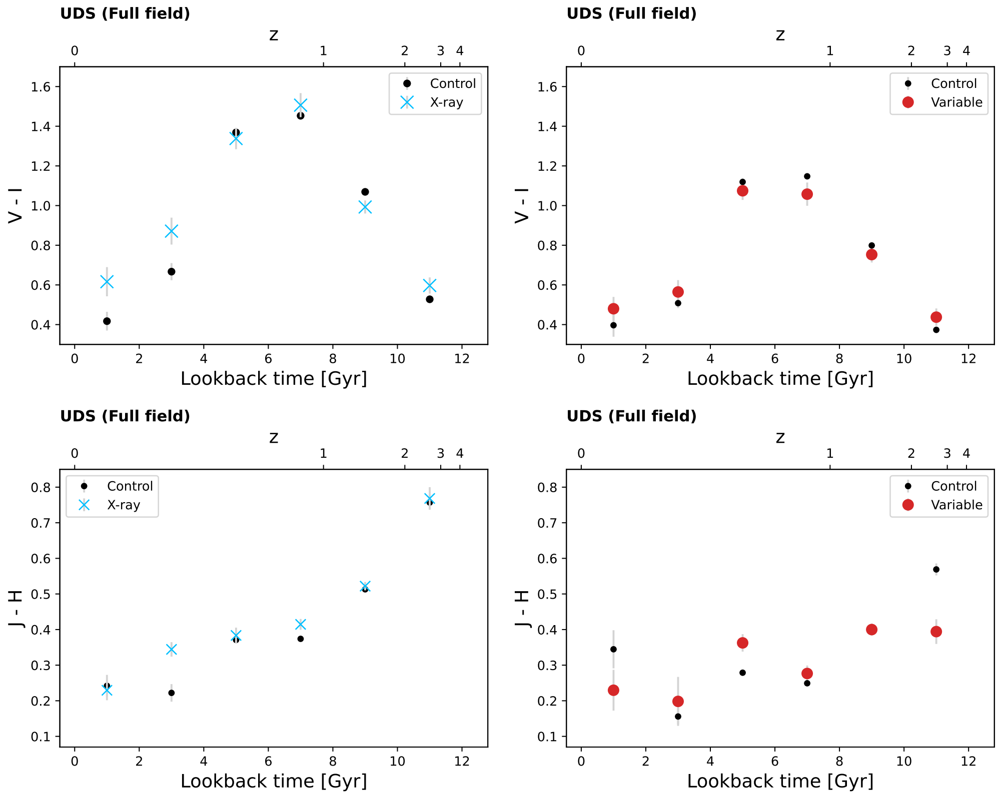

Figure 6.3: Optical V - I (top) and infrared J - H (bottom) colour vs look back time for active galaxies and their matched control galaxies. The left column shows X-ray detected AGN as blue crosses and the right column shows variability detected active galaxies as red points. In both groups corresponding control galaxies are black points. Galaxies in these samples are drawn from the full, ground-based UDS field and measured magnitudes are apparent magnitudes. Galaxy colours are averaged in bins of 2Gyrs with error bars being the standard error on the mean. Look back times are calculated based on the redshift, and corresponding redshifts are shown on the top x-axis of the plots.

be found in a wide range of environments implying no singular global conditions are required to trigger AGN activity.

6.5.2 Infrared and optical colour comparisons

Having studied the wider environments of active galaxies, we next inspect the features of the galaxies themselves. One interesting property to study is if AGN emission has a significant impact on the colours of active galaxies. Using magnitude measurements of the active galaxies as a whole, we plot the optical V - I and infrared J - H colour as a function of cosmic time in Figure 6.3. Interestingly, we find that both X-ray bright and variability-detected active galaxies appear to have similar colours compared to control galaxies, with this holding for all epochs studied. The only notable difference is seen when comparing X-ray detected samples to variability detected samples, where the variability-detected group generally show a less extreme colour evolution, however this changes when active galaxies are split into subgroups.

To see if active galaxies as a global population have comparable colours to inactive galaxies, we further investigate the colour evolution of the samples by splitting the galaxies into subgroups. X-ray detected galaxies are measured in the full band (0.5-10keV) and are split based on hardness ratio into X-ray soft (HR<0) and X-ray hard (HR≥0) galaxies, and variability detected galaxies are split based on J and K-band variability. Plotting the optical and infrared colours of these galaxies against look back time in Figure 6.4, differences appear in the samples, with the colours of the subgroups being consistently offset from each other. X-ray hard galaxies are consistently redder than X-ray soft galaxies, and K-band variable galaxies appear redder in both optical and infrared colours compared to their J-band variable counterparts. This result remains largely consistent throughout cosmic time and provides further evidence in support of K-band variable AGN residing in dusty galaxies, as explored in Chapter 5.

To further investigate the individual properties of the active galaxies, we move on to compare the colour evolution with morphology. In Figure 6.5, we plot the optical V - I and infrared J - H colour vs the Sérsic index n for the active and control galaxies. Examining first the optical colours, we find that the active X-ray sample are consistently bluer compared to their matched control sample for all morphologies studied. In addition to this, they show no significant change in colour from disk- to bulge-dominated systems, whereas the control sample becomes slightly redder as the bulge component becomes more significant in the galaxy morphology. In contrast to this, the optical colour of the active variable sample shows significant evolution with morphology. Here comparisons of disk-dominated systems finds active and control galaxies have near identical colours; however as the morphology changes towards bulge dominated systems, the colours diverge, with active galaxies becoming much bluer compared to controls which remains largely static. Measurements of infrared colours are far less consistent however, with variability detected galaxies appearing much bluer than X-ray bright active galaxies overall, but both groups having a larger scatter in their colour evolution with morphology compared to their respective control sets.

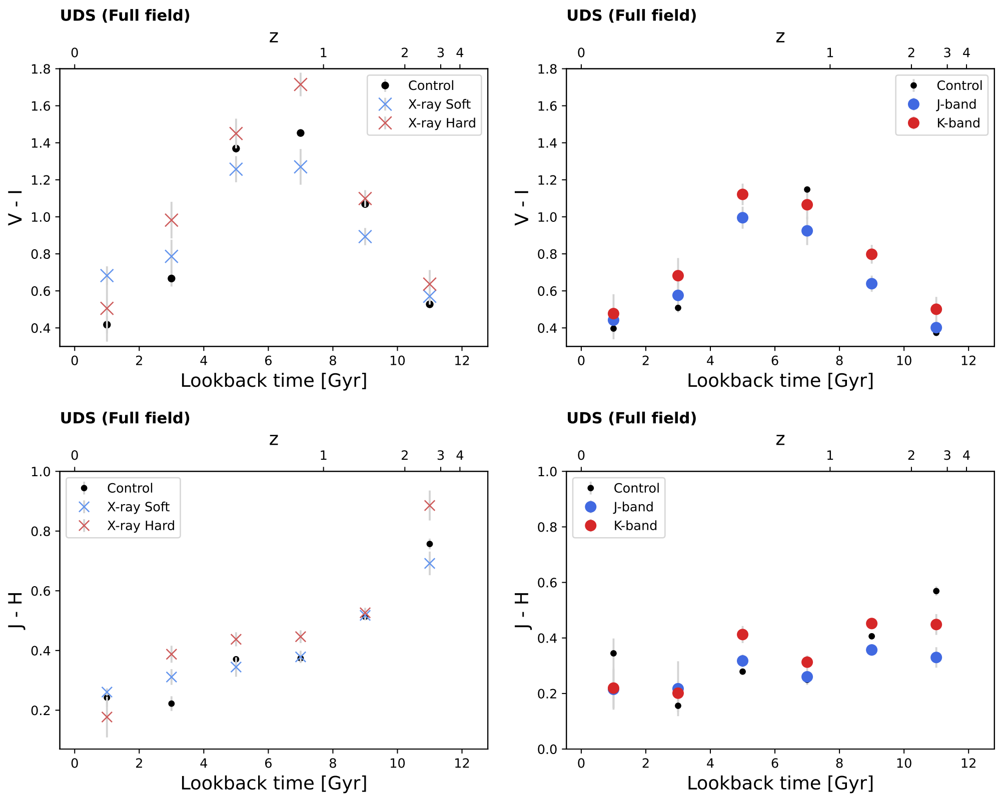

Figure 6.4: Optical *V* - *I* (top) and infrared *J* - *H* (bottom) colour vs look back time for active galaxies and their matched control galaxies. Galaxies in these samples are drawn from the full, ground-based UDS field and measured magnitudes are apparent magnitudes. X-ray bright samples are shown as crosses are and split based on hardness ratio, with X-ray soft (HR<0) in blue and X-ray hard (HR≥0) in red. Significantly variable galaxies are denoted by coloured points, with any active galaxy variable in the *J*-band in blue and any active galaxy variable in the *K*-band in red. In both samples control galaxies are matched to the overall active populations and are denoted as black points. Galaxy colours are averaged in bins of 2Gyrs with error bars being the standard error on the mean. Look back times are calculated based on the redshift, and corresponding redshifts are shown on the top x-axis of the plots.

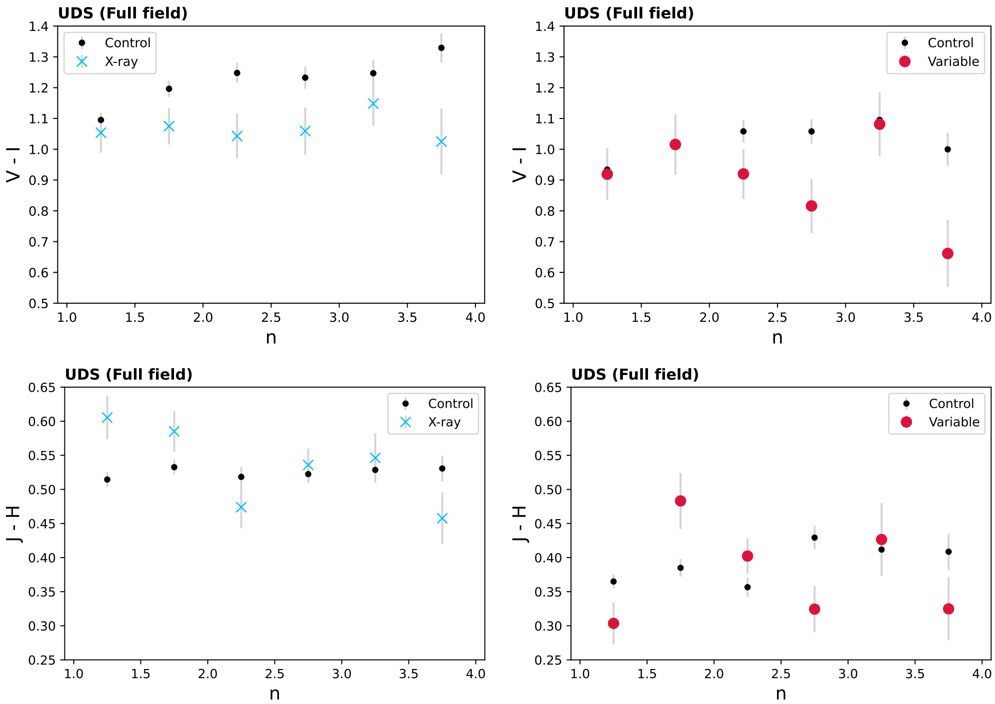

Figure 6.5: Optical V - I (top) and infrared J - H (bottom) colour vs Sérsic index for active galaxies and matched control galaxies. The left column shows X-ray detected AGN as blue crosses and the right column has variability detected active galaxies as red points. In both groups corresponding control galaxies are black points. Galaxies in this sample are drawn from the full, ground-based UDS field and measured magnitudes are apparent magnitudes. Galaxy colours are averaged in bins of 0.5 with error bars being the standard error on the mean.

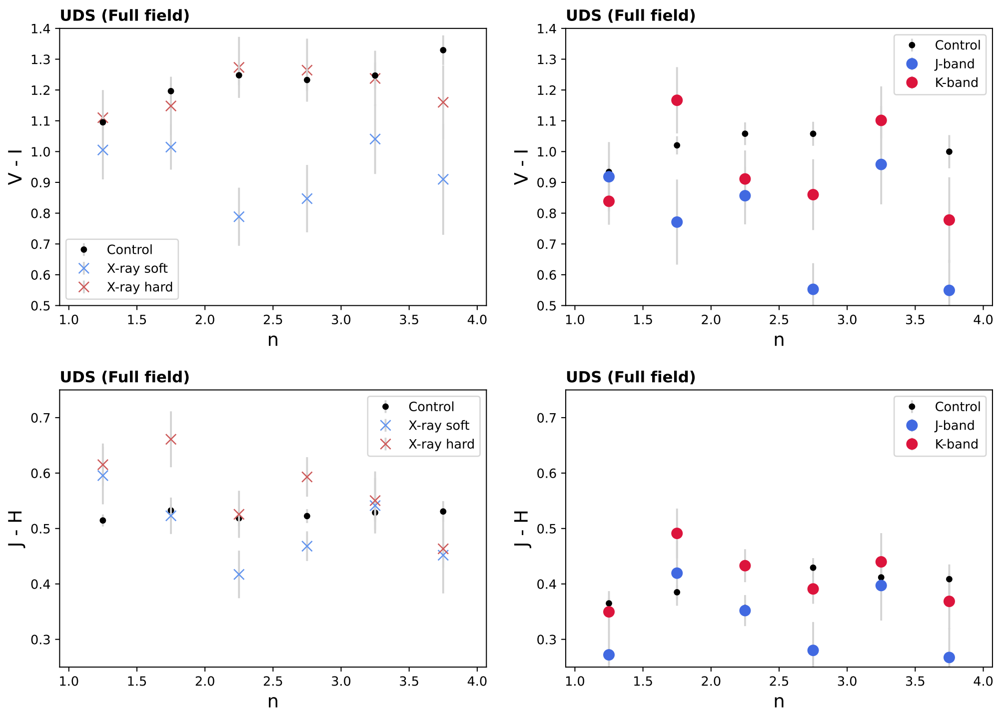

Figure 6.6: Optical V - I (top) and infrared J - H (bottom) colour vs Sérsic index for active galaxies and their matched control galaxies. Galaxies in these samples are drawn from the full, ground-based UDS field and measured magnitudes are apparent magnitudes. X-ray bright samples are shown as crosses are and split based on hardness ratio, with X-ray soft (HR<0) in blue and X-ray hard (HRgeq0) in red. Significantly variable galaxies are denoted by coloured circles, with any active galaxy variable in the J-band in blue and any active galaxy variable in the K-band in red. In both samples control galaxies are matched to the overall active populations and are denoted as black points. Galaxy colours are averaged in Sérsic index bins of 0.5, with error bars being the standard error on the mean.

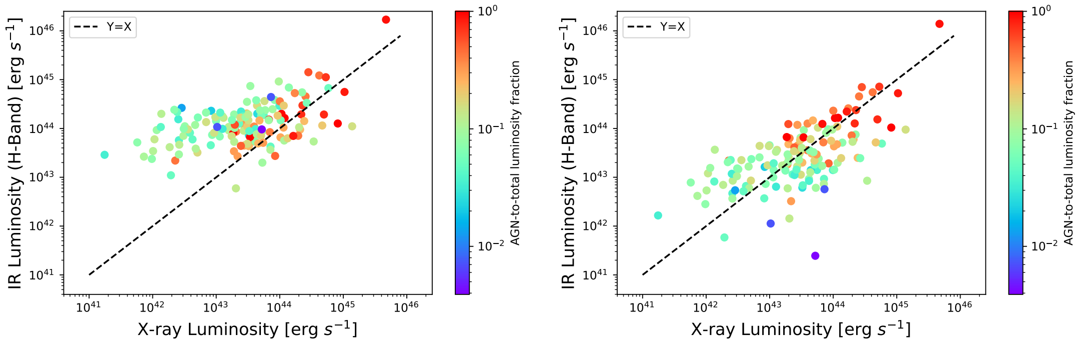

Figure 6.7: H-band infrared luminosity vs full band (0.5-10keV) X-ray luminosity for the X-ray detected active galaxies found within the CANDELS-UDS imaging region. In the left plot the infrared luminosity is based on a single Sérsic fit to the galaxy image, in the right plot the infrared luminosity is calculated from the magnitude returned from the PSF component in a combined Sérsic + PSF fit to the active galaxies. In both plots the X-ray luminosity is drawn from the Chandra X-ray catalogue (see Chapter 2). Points are colour coded according to the fraction of the total luminosity of the object attributed to the PSF component in the two component Sérsic + PSF fit. The black dashed line traces unity.

Following the differences found when investigating how the colours of active galaxies change with morphology, we once again create further subgroups for analysis by categorising the galaxies by X-ray hardness ratio and variability band. This is shown in Figure 6.6, which shows that in all cases, for a given morphology X-ray hard galaxies are redder than X-ray soft galaxies, and K-band variable galaxies are redder than J-band variable galaxies. When comparing these colours to control galaxies however, we find mixed results. In the optical, X-ray-soft active galaxies are significantly bluer than the matched control galaxies, whereas colours of X-ray-hard galaxies are very similar to that of controls at all morphologies. In all other cases, colours of active groups largely overlap with the colours of the control samples, with the offset between X-ray hard and soft and J and K variable subgroups remaining consistent but no significant trends with morphology being noticeable.

6.5.3 Two component Sérsic + PSF fits

In Section 6.5.2, we studied the conditions and extent by which observations of active galaxies differ to those of inactive galaxies. However, to be able to gather accurate

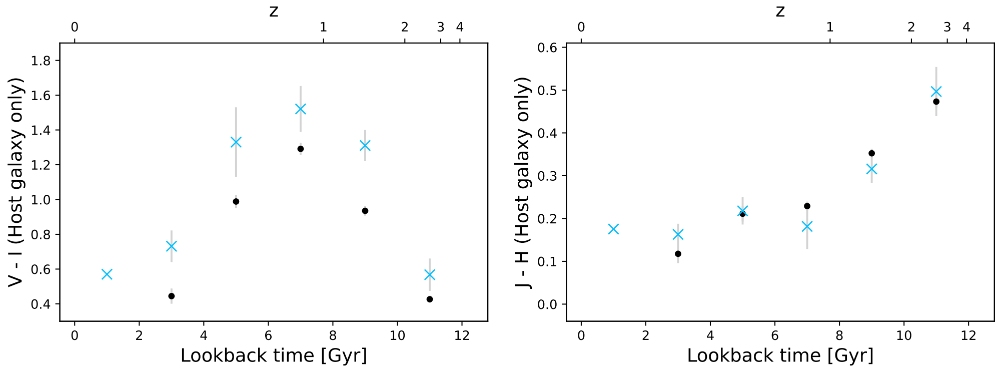

Figure 6.8: Optical V - I (left) and infrared J - H (right) colour vs look back time for the X-ray detected active galaxies and matched control galaxies in the CANDELS-UDS imaging region. X-ray bright active galaxies are denoted by blue crosses and corresponding matched control galaxies are shown as black points. Galaxies are averaged in bins of 2Gyrs with error bars being the standard error on the mean. Look back times are calculated based on the redshift, and corresponding redshifts are shown on the top x-axis of the plots. Magnitudes are apparent magnitudes and are drawn from the Sérsic component in a combined two component Sérsic + PSF fit to the active galaxies.

properties of the galaxies AGN exist in, AGN and host galaxy emission must be separated out. To remove AGN contamination on host galaxy emission, we perform a two component fit to active galaxy imaging, where a PSF component is included to account for AGN radiation and a standard Sérsic profile is used to calculate host parameters.

To measure the host galaxy parameters, we use CANDELS-UDS optical and infrared imaging (Section 6.2.2) of a subsection of the wider UKIDSS UDS field. To determine the effectiveness of this approach, we examine how the X-ray luminosity compares to the infrared luminosity in Figure 6.7. According to AGN emission theory, a majority of the X-rays originate from the AGN in a given active galaxy. The SED of active galaxies is also largely flat between X-ray and infrared emission, and as such one would expect approximately equal IR luminosities and X-ray luminosities. Examining Figure 6.7, we find that a two component fit is required to accurately model the emission from active galaxies. A single Sérsic fit proves to be insufficient, and this is most apparent in galaxies where the AGN counts for $\lesssim$25% of the total emission. In such galaxies, modelling the combined AGN and host galaxy emission via a single Sérsic profile results in an overestimation of the AGN radiation, however including a PSF component as a model for point-source AGN emission allows for the AGN emission to be separated out and credibly fitted in the analysis, causing measured luminosities to drop to more sensible

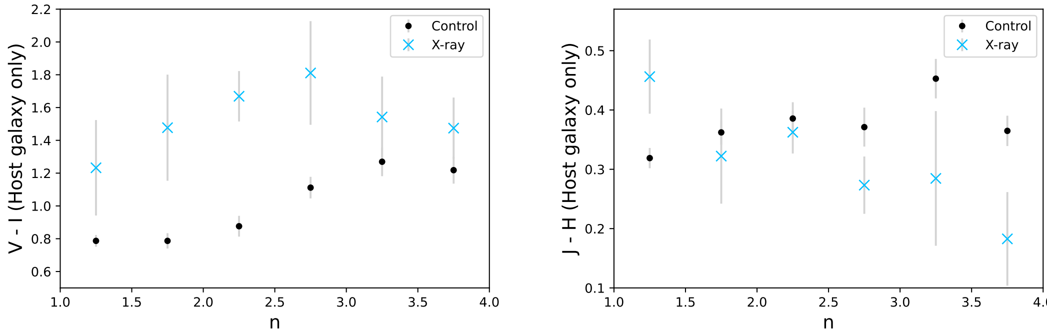

Figure 6.9: Optical *V* - *I* (left) and infrared *J* - *H* (right) colour vs Sérsic index for the active galaxies and matched control galaxies in the CANDELS-UDS imaging region. X-ray bright active galaxies are denoted by blue crosses and matched control galaxies are shown as black points. Galaxies are averaged in bins of 0.5 with error bars being the standard error on the mean. Magnitudes are apparent magnitudes and both magnitudes and Sérsic index are drawn from the Sérsic component in a combined two component Sérsic + PSF fit to the active galaxy images.

values. Using a two component Sérsic + PSF fit to the active galaxies also allows for the fraction that the host galaxy and AGN contribute to the overall observed flux to be determined. Inspecting this, we find that the brighter the galaxy, the more the AGN emission dominates in the total emission of the galaxy.

6.5.4 Host galaxy comparisons

We have found evidence that AGN emission can be separated out from host galaxy light in active galaxies (Section6.5.3). Using the output of the two component fitting to active galaxies, we compare the optical and infrared colours of the AGN host galaxies to a matched control set of inactive galaxies over cosmic time (Figure 6.8). Examining how the host colours change over cosmic time, we find the optical colour of X-ray AGN host galaxies are significantly redder than that of the control galaxies at a given epoch. Comparisons of the infrared colour however does not find significant differences in the overall colour of active and control galaxies. This result is in contrast to the same measure made in Figure 6.3, where a singular Sérsic model was fit to the data. Where overall measures of active galaxies have similar colours compared to matched controls, the host galaxies of AGN are systematically redder in colour for all look back bins measured.

Finally we examine the host colours as a function of morphology in Figure 6.9. We note that both optical and infrared colours of X-ray host galaxies show significant differences compared with the control galaxies. In the optical, X-ray hosts are consistently redder than control galaxies for all morphologies measured, which is in contrast to the overall comparison calculated on ground based data (Figure 6.5), where single Sérsic fits found X-ray galaxies to be bluer than control galaxies at a given Sérsic index. In the infrared, we see an evolution of the colour with morphology. Where control galaxies are redder with increasing Sérsic index, AGN host galaxies are shown to be bluer in bulge-dominated systems. Again this is shown to be significantly different compared to measures of the overall active galaxy system (Figure 6.5) where infrared colours showed no strong trends compared to inactive galaxies.

6.6 Conclusions

In this research we investigate how observations of active galaxies differ from those of inactive galaxies and whether these differences are associated with the the AGN environment or host galaxy. We first match active galaxies to inactive galaxies on stellar mass, radius and redshift to form a control group, and by taking the same measurements on active and control galaxies we find a mix of differences in both active galaxy environment and host properties, some of which may be dependant on the AGN detection method.

We first find that AGN exist in different environments when splitting active galaxies by detection method. X-ray bright active galaxies are preferentially found in denser environments compared to matched inactive galaxies, but otherwise show a similar evolution of environment over cosmic time. Inspecting this same property for variability detected active galaxies however, finds they have a different cosmic evolution with environment compared to matched control galaxies. Here the environments density of the active galaxies decreases linearly with look back time, diverging to denser environments when considering the shortest look back bins. These results imply that the triggering of X-ray bright AGN may be more closely linked to the wider environment of the active galaxies compared to variability-detected active galaxies.

In order to assess how the properties of active galaxies differ to those of inactive galaxies, we took a comparison of the optical and infrared colour evolution of the active and control groups. No significant differences between optical or infrared colours of either active group or their control galaxies were found, however we do note that variability detected galaxies show a less extreme colour variation over time compared to X-ray detected samples. Significant differences can be found however when splitting the galaxies into different subgroups based on hardness ratio and variability detection band. In this case, we find X-ray hard galaxies to be redder at all epochs compared to X-ray soft galaxies and K-band variable galaxies to be redder than J-band variable galaxies, which provides evidence in support of the hypothesis that K-band variability probes dusty galaxies.

Further analysis shows that the colour evolution of active galaxies behaves different depending on the detection method used for the AGN. In the X-ray detected sample, for a given morphology, X-ray bright active galaxies are consistently bluer than control galaxies in the optical colour. When considering the variability detected galaxies, a colour evolution with galactic shape is found instead of consistent differences. Here optical measurements find the variable AGN are much bluer in bulge dominated galaxies, whereas colours are indistinguishable from controls in disk-type systems. Morphological comparisons in the infrared however are much less clear with both groups showing large overlaps with controls for various systems, however we do note that the infrared colours of the variable AGN are much bluer than that of the X-ray groups overall. Splitting this comparison into the subgroups find a clear distinction that X-ray soft and J-band variables are consistently bluer than X-ray hard and K-band variable galaxies and this holds for all colour combinations studied.

From comparing observational properties of active galaxies as a whole to control galaxies, we conclude that, given a large dataset of galaxies, active galaxies do indeed appear different compared to matched control galaxies. This is most noticeable in the environments of active galaxies, which are different in both density and evolution compared to normal galaxies. In addition to this, active galaxies show different colour distributions at a fixed morphology. Though both X-ray and variable active populations tend to have similar colours to controls at a given epoch, sub-samples of galaxies show separate colour distributions as a function of both morphology and look back time, supporting the idea that K-band variability probes AGN in dusty systems.

Finally, we presented preliminary research into the host properties of X-ray detected AGN. This work was restricted to the X-ray sample, as the number of variability detected active galaxies that had the high resolution imaging required for this technique to work was too small for robust conclusions to be drawn. To inspect the host properties of active galaxies, a combined two component, Sérsic + PSF profile of the galaxies was taken such that the host could be decomposed from the AGN. This two component analysis was largely successful on X-ray bright active galaxies, where comparisons of the infrared and X-ray luminosity improve significantly, becoming well correlated with the addition of a PSF component when fitting. Interestingly, host properties were found to differ significantly from controls galaxies, with mean optical colours appearing redder than controls at a given epoch as well as a specific Sérsic index range. These preliminary results illustrate the need for AGN-host galaxy decomposition in determining accurate properties for the host galaxies AGN exist in, as well as allowing for if and how these may change depending on how a given AGN is detected.

Chapter 7

Conclusions and Future Work

7.1 Conclusions

7.2 Future work

- Investigate the host galaxies of AGN in more detail, specifically possible explanations for why the hosts of X-ray AGN get bluer with increasing Sèrsic index
- Look at the host properties of the variable AGN in general, hopefully should be doable with high resolution imaging like JWST provides.
  - Investigate how the AGN properties change with variability amplitude
  - Especially look at if/how the host of variable AGN change depending on the band the AGN was found to be variable in. If K-band variables are dusty for example, you may expect them to be red in colour.
- Different types of active galaxies found in different environments, look into this more and see if they link to possible triggering mechanisms
- Some kind of spectra fitting to the SED from X-rays to Mid or Far-infrared (using additional imaging from JWST) and even radio if it is available would be interesting to do on the active galaxies. Compare and contrast between types

Bibliography

Aird, J., Coil, A. L., Moustakas, J., et al. 2012, The Astrophysical Journal, 746, 90, doi: 10.1088/0004-637X/746/1/90

Alloin, D. M. D. M., Johnson, R., & Lira, P., eds. 2006, Physics of active galactic nuclei at all scales No. 693 (Berlin: Springer)

Almaini, O., Lawrence, A., Shanks, T., et al. 2000, Monthly Notices of the Royal Astronomical Society, 315, 325, doi: 10.1046/j.1365-8711.2000.03385.x

Almaini, O., Wild, V., Maltby, D. T., et al. 2017, Monthly Notices of the Royal Astronomical Society, 472, 1401, doi: 10.1093/mnras/stx1957

Antonucci, R. 1993, Annual Review of Astronomy and Astrophysics, 31, 473, doi: 10.1146/annurev.aa.31.090193.002353

Avni, Y., & Tananbaum, H. 1986, The Astrophysical Journal, 305, 83, doi: 10.1086/164230

Baade, W., & Minkowski, R. 1954, The Astrophysical Journal, 119, 215, doi: 10.1086/145813

Barden, M., Häußler, B., Peng, C. Y., McIntosh, D. H., & Guo, Y. 2012, Monthly Notices of the Royal Astronomical Society, 422, 449, doi: 10.1111/j.1365-2966.2012.20619.x

Barvainis, R. 1987, The Astrophysical Journal, 320, 537, doi: 10.1086/165571

Beckmann, V., & Shrader, C. 2013, in Proceedings of An INTEGRAL view of the high-energy sky (the first 10 years) - 9th INTEGRAL Workshop and celebration of the 10th anniversary of the launch — PoS(INTEGRAL 2012), Vol. 176 (SISSA Medialab), 069, doi: 10.22323/1.176.0069

Berk, D. E. V., Wilhite, B. C., Kron, R. G., et al. 2004, The Astrophysical Journal, 601, 692, doi: 10.1086/380563

Best, P. N., von der Linden, A., Kauffmann, G., Heckman, T. M., & Kaiser, C. R.

2007, Monthly Notices of the Royal Astronomical Society, 379, 894, doi: 10.1111/j.1365-2966.2007.11937.x

Bianchi, S., Mainieri, V., & Padovani, P. 2022, in Handbook of X-ray and Gamma-ray Astrophysics, ed. C. Bambi & A. Santangelo (Singapore: Springer Nature), 1–32, doi: 10.1007/978-981-16-4544-0_113-1

Bongiorno, A., Merloni, A., Brusa, M., et al. 2012, Monthly Notices of the Royal Astronomical Society, 427, 3103, doi: 10.1111/j.1365-2966.2012.22089.x

Bradshaw, E. J., Almaini, O., Hartley, W. G., et al. 2013, Monthly Notices of the Royal Astronomical Society, 433, 194, doi: 10.1093/mnras/stt715

Brammer, G. B., Dokkum, P. G. v., & Coppi, P. 2008, The Astrophysical Journal, 686, 1503, doi: 10.1086/591786

Bruzual, G., & Charlot, S. 2003, Monthly Notices of the Royal Astronomical Society, 344, 1000, doi: 10.1046/j.1365-8711.2003.06897.x

Cackett, E. M., Bentz, M. C., & Kara, E. 2021, iScience, 24, 102557, doi: 10.1016/j.isci.2021.102557

Calvi, V., Stiavelli, M., Bradley, L., Pizzella, A., & Kim, S. 2014, The Astrophysical Journal, 796, 102, doi: 10.1088/0004-637X/796/2/102

Casali, M., Adamson, A., Oliveira, C. A. d., et al. 2007, Astronomy & Astrophysics, 467, 777, doi: 10.1051/0004-6361:20066514

Chabrier, G. 2003, Publications of the Astronomical Society of the Pacific, 115, 763, doi: 10.1086/376392

Cid Fernandes, R., Aretxaga, I., & Terlevich, R. 1996, Monthly Notices of the Royal Astronomical Society, 282, 1191, doi: 10.1093/mnras/282.4.1191

Civano, F., Elvis, M., Brusa, M., et al. 2012, The Astrophysical Journal Supplement Series, 201, 30, doi: 10.1088/0067-0049/201/2/30

Clavel, J., Wamsteker, W., & Glass, I. S. 1989, The Astrophysical Journal, 337, 236, doi: 10.1086/167100

Cleary, K., Lawrence, C. R., Marshall, J. A., Hao, L., & Meier, D. 2007, The Astrophysical Journal, 660, 117, doi: 10.1086/511969

Collaboration, E. H. T., Akiyama, K., Alberdi, A., et al. 2022, The Astrophysical Journal Letters, 930, L12, doi: 10.3847/2041-8213/ac6674

Collaboration, T. E. H. T., Akiyama, K., Alberdi, A., et al. 2019, The Astrophysical Journal Letters, 875, L1, doi: 10.3847/2041-8213/ab0ec7

Collier, S., & Peterson, B. M. 2001, The Astrophysical Journal, 555, 775, doi: 10.1086/321517

Curtis, H. D. 1988, Publications of the Astronomical Society of the Pacific, 100, 6, doi: 10.1086/132128

Cutri, R. M., Wisniewski, W. Z., Rieke, G. H., & Lebofsky, M. J. 1985, The Astrophysical Journal, 296, 423, doi: 10.1086/163461

Dayal, P., Volonteri, M., Choudhury, T. R., et al. 2020, Monthly Notices of the Royal Astronomical Society, 495, 3065, doi: 10.1093/mnras/staa1138

Dermer, C. D., & Giebels, B. 2016, Comptes Rendus. Physique, 17, 594, doi: 10.1016/j.crhy.2016.04.004

Dicken, D., Tadhunter, C., Axon, D., et al. 2009, The Astrophysical Journal, 694, 268, doi: 10.1088/0004-637X/694/1/268

Dressler, A., Thompson, I. B., & Shectman, S. A. 1985, The Astrophysical Journal, 288, 481, doi: 10.1086/162813

Edelson, R. A., & Malkan, M. A. 1987, The Astrophysical Journal, 323, 516, doi: 10.1086/165848

Eide, M. B., Ciardi, B., Graziani, L., et al. 2020, Monthly Notices of the Royal Astronomical Society, 498, 6083, doi: 10.1093/mnras/staa2774

Einstein, A. 1916, Annalen der Physik, 354, 769, doi: 10.1002/andp.19163540702

Einstein, A., Minkowski, H. H., Saha, M., & Bose, S. 1920, The principle of relativity; original papers ([Calcutta] The University of Calcutta). http://archive.org/details/principleofrelat00eins

Elmer, E., Almaini, O., Merrifield, M., et al. 2020, Monthly Notices of the Royal Astronomical Society, 493, 3026, doi: 10.1093/mnras/staa381

Elmer, E., Merrifield, M., Almaini, O., Hartley, W. G., & Maltby, D. T. 2021, Monthly Notices of the Royal Astronomical Society: Letters, 503, L47, doi: 10.1093/mnrasl/slab023

Elvis, M., Green, R. F., Bechtold, J., et al. 1986, The Astrophysical Journal, 310, 291, doi: 10.1086/164683

Fabian, A. C. 2012, Annual Review of Astronomy and Astrophysics, 50, 455, doi: 10.1146/annurev-astro-081811-125521

Falder, J. T., Stevens, J. A., Jarvis, M. J., et al. 2010, Monthly Notices of the Royal Astronomical Society, 405, 347, doi: 10.1111/j.1365-2966.2010.16444.x

Fan, L., Fang, G., Chen, Y., et al. 2014, The Astrophysical Journal Letters, 784, L9, doi: 10.1088/2041-8205/784/1/L9

Fath, E. A. 1909, Lick Observatory Bulletin, 149, 71, doi: 10.5479/ADS/bib/1909LicOB.5.71F

Ferrara, A., Zana, T., Gallerani, S., & Sommovigo, L. 2023, Monthly Notices of the Royal Astronomical Society, 520, 3089, doi: 10.1093/mnras/stad299

Finkelstein, D. 1958, Physical Review, 110, 965, doi: 10.1103/PhysRev.110.965

Fitch, W. S., Pacholczyk, A. G., & Weymann, R. J. 1967, The Astrophysical Journal, 150, L67, doi: 10.1086/180095

Furusawa, H., Kosugi, G., Akiyama, M., et al. 2008, The Astrophysical Journal Supplement Series, 176, 1, doi: 10.1086/527321

Gabor, J. M., Impey, C. D., Jahnke, K., et al. 2009, The Astrophysical Journal, 691, 705, doi: 10.1088/0004-637X/691/1/705

Genzel, R., Eisenhauer, F., & Gillessen, S. 2010, Reviews of Modern Physics, 82, 3121, doi: 10.1103/RevModPhys.82.3121

Georgantopoulos, I., Pouliasis, E., Mountrichas, G., et al. 2023, Astronomy & Astrophysics, 673, A67, doi: 10.1051/0004-6361/202244875

Ghez, A. M., Klein, B. L., Morris, M., & Becklin, E. E. 1998, The Astrophysical Journal, 509, 678, doi: 10.1086/306528

Gisler, G. R. 1978, Monthly Notices of the Royal Astronomical Society, 183, 633, doi: 10.1093/mnras/183.4.633

Green, A. R., McHardy, I. M., & Lehto, H. J. 1993, Monthly Notices of the Royal Astronomical Society, 265, 664, doi: 10.1093/mnras/265.3.664

Griffith, R. L., & Stern, D. 2010, The Astronomical Journal, 140, 533, doi: 10.1088/0004-6256/140/2/533

Grogin, N. A., Conselice, C. J., Chatzichristou, E., et al. 2005, The Astrophysical Journal, 627, L97, doi: 10.1086/432256

Grogin, N. A., Kocevski, D. D., Faber, S. M., et al. 2011, The Astrophysical Journal Supplement Series, 197, 35, doi: 10.1088/0067-0049/197/2/35

Hafez, I. 2010, phd, James Cook University, doi: 10.25903/6xsf-aa64

Hainline, K. N., Shapley, A. E., Greene, J. E., et al. 2012, The Astrophysical Journal, 760, 74, doi: 10.1088/0004-637X/760/1/74

Harrison, C. 2014, Doctoral, Durham University. http://etheses.dur.ac.uk/10744/

Herrero, A., Kudritzki, R. P., Gabler, R., Vilchez, J. M., & Gabler, A. 1995, Astronomy and Astrophysics, 297, 556. https://ui.adsabs.harvard.edu/abs/1995A&A...297..556H

Hewlett, T., Villforth, C., Wild, V., et al. 2017, Monthly Notices of the Royal Astronomical Society, 470, 755, doi: 10.1093/mnras/stx997

Hickox, R. C., & Alexander, D. M. 2018, Annual Review of Astronomy and Astrophysics, 56, 625, doi: 10.1146/annurev-astro-081817-051803

Hopkins, P. F., Hernquist, L., Cox, T. J., et al. 2006, The Astrophysical Journal Supplement Series, 163, 1, doi: 10.1086/499298

Hubble, E. 1929, Proceedings of the National Academy of Sciences, 15, 168, doi: 10.1073/pnas.15.3.168

Hubble, E. P. 1925, The Astrophysical Journal, 62, 409, doi: 10.1086/142943

—. 1926, The Astrophysical Journal, 64, 321, doi: 10.1086/143018

Humason, M. L. 1932, Publications of the Astronomical Society of the Pacific, 44, 267, doi: 10.1086/124242

Hunt, L. K., Zhekov, S., Salvati, M., Mannucci, F., & Stanga, R. M. 1994, Astronomy and Astrophysics, 292, 67. https://ui.adsabs.harvard.edu/abs/1994A&A...292...67H

Hutchings, J. B., Scholz, P., & Bianchi, L. 2009, The Astronomical Journal, 137, 3533, doi: 10.1088/0004-6256/137/3/3533

Häußler, B., Bamford, S. P., Vika, M., et al. 2013, Monthly Notices of the Royal Astronomical Society, 430, 330, doi: 10.1093/mnras/sts633

information@eso.org. 1999, The Hubble tuning fork - classification of galaxies. https://www.spacetelescope.org/images/heic9902o/

Inskip, K. J., Tadhunter, C. N., Morganti, R., et al. 2010, Monthly Notices of the Royal Astronomical Society, 407, 1739, doi: 10.1111/j.1365-2966.2010.17002.x

Jarvis, M. J., Bonfield, D. G., Bruce, V. A., et al. 2013, Monthly Notices of the Royal Astronomical Society, 428, 1281, doi: 10.1093/mnras/sts118

Kauffmann, G., White, S. D. M., Heckman, T. M., et al. 2004, Monthly Notices of the Royal Astronomical Society, 353, 713, doi: 10.1111/j.1365-2966.2004.08117.x

Kauffmann, G., Heckman, T. M., Tremonti, C., et al. 2003, Monthly Notices of the Royal Astronomical Society, 346, 1055, doi: 10.1111/j.1365-2966.2003.07154.x

Kocevski, D. D., Hasinger, G., Brightman, M., et al. 2018, The Astrophysical Journal Supplement Series, 236, 48, doi: 10.3847/1538-4365/aab9b4

Koekemoer, A. M., Faber, S. M., Ferguson, H. C., et al. 2011, The Astrophysical Journal Supplement Series, 197, 36, doi: 10.1088/0067-0049/197/2/36

Kormendy, J., & Richstone, D. 1995, Annual Review of Astronomy and Astrophysics, 33, 581, doi: 10.1146/annurev.aa.33.090195.003053

Kouzuma, S., & Yamaoka, H. 2012, The Astrophysical Journal, 747, 14, doi: 10.1088/0004-637X/747/1/14

Lammers, C., Iyer, K. G., Ibarra-Medel, H., et al. 2023, The Astrophysical Journal, 953, 26, doi: 10.3847/1538-4357/acdd57

Lani, C., Almaini, O., Hartley, W. G., et al. 2013, Monthly Notices of the Royal Astronomical Society, 435, 207, doi: 10.1093/mnras/stt1275

Lawrence, A., Watson, M. G., Pounds, K. A., & Elvis, M. 1987, Nature, 325, 694, doi: 10.1038/325694a0

Lawrence, A., Warren, S. J., Almaini, O., et al. 2007, Monthly Notices of the Royal Astronomical Society, 379, 1599, doi: 10.1111/j.1365-2966.2007.12040.x

LIGO Scientific Collaboration and Virgo Collaboration, Abbott, B., Abbott, R., et al. 2016, Physical Review Letters, 116, 061102, doi: 10.1103/PhysRevLett.116.061102

Lira, P., Arévalo, P., Uttley, P., McHardy, I., & Breedt, E. 2011, Monthly Notices of the Royal Astronomical Society, 415, 1290, doi: 10.1111/j.1365-2966.2011.18774.x

Lira, P., Arévalo, P., Uttley, P., McHardy, I. M. M., & Videla, L. 2015, Monthly Notices of the Royal Astronomical Society, 454, 368, doi: 10.1093/mnras/stv1945

Low, J., & Kleinmann, D. E. 1968, The Astronomical Journal, 73, 868, doi: 10.1086/110722

Lyu, J., Alberts, S., Rieke, G. H., & Rujopakarn, W. 2022, The Astrophysical Journal, 941, 191, doi: 10.3847/1538-4357/ac9e5d

López, I. E., Brusa, M., Bonoli, S., et al. 2023, Astronomy & Astrophysics, 672, A137, doi: 10.1051/0004-6361/202245168

MacLeod, C. L., Ivezić, , Kochanek, C. S., et al. 2010, The Astrophysical Journal, 721, 1014, doi: 10.1088/0004-637X/721/2/1014

Madejski, G. G., & Sikora, M. 2016, Annual Review of Astronomy and Astrophysics, 54, 725, doi: 10.1146/annurev-astro-081913-040044

Maltby, D. T., Almaini, O., Wild, V., et al. 2018, Monthly Notices of the Royal Astronomical Society, 480, 381, doi: 10.1093/mnras/sty1794

—. 2016, Monthly Notices of the Royal Astronomical Society: Letters, 459, L114, doi: 10.1093/mnrasl/slw057

McLure, R. J., Pearce, H. J., Dunlop, J. S., et al. 2013, Monthly Notices of the Royal Astronomical Society, 428, 1088, doi: 10.1093/mnras/sts092

McLure, R. J., Pentericci, L., Cimatti, A., et al. 2018, Monthly Notices of the Royal Astronomical Society, 479, 25, doi: 10.1093/mnras/sty1213

Meusinger, H., Hinze, A., & Hoon, A. d. 2011, Astronomy & Astrophysics, 525, A37, doi: 10.1051/0004-6361/201015520

Michell, J. 1997, Philosophical Transactions of the Royal Society of London, 74, 35, doi: 10.1098/rstl.1784.0008

Miller, C. J., Nichol, R. C., Gómez, P. L., Hopkins, A. M., & Bernardi, M. 2003, The Astrophysical Journal, 597, 142, doi: 10.1086/378383

Molina, J., Ho, L. C., Wang, R., et al. 2023, The Astrophysical Journal, 944, 30, doi: 10.3847/1538-4357/acaa9b

Mountrichas, G., Buat, V., Yang, G., et al. 2022, Astronomy & Astrophysics, 667, A145, doi: 10.1051/0004-6361/202244495

Netzer, H. 2013, The Physics and Evolution of Active Galactic Nuclei (New York, UNITED STATES: Cambridge University Press). http://ebookcentral.proquest.com/lib/nottingham/detail.action?docID=1113069

Neugebauer, G., Soifer, B. T., Matthews, K., & Elias, J. H. 1989, The Astronomical Journal, 97, 957, doi: 10.1086/115040

Pacholczyk, A. G., & Wisniewski, W. Z. 1967, The Astrophysical Journal, 147, 394, doi: 10.1086/149020

Padovani, P., Alexander, D. M., Assef, R. J., et al. 2017, The Astronomy and Astrophysics Review, 25, 2, doi: 10.1007/s00159-017-0102-9

Paltani, S., & Courvoisier, T. J. L. 1994, Astronomy and Astrophysics, 291, 74. https://ui.adsabs.harvard.edu/abs/1994A&A...291...74P

Panagiotou, C., Papadakis, I., Kara, E., Kammoun, E., & Dovčiak, M. 2022, A physical model for the UV/optical power spectra of AGN, arXiv, doi: 10.48550/arXiv.2207.04917

Peng, C. Y., Ho, L. C., Impey, C. D., & Rix, H.-W. 2002, The Astronomical Journal, 124, 266, doi: 10.1086/340952

—. 2010, The Astronomical Journal, 139, 2097, doi: 10.1088/0004-6256/139/6/2097

Pentericci, L., McLure, R. J., Garilli, B., et al. 2018, Astronomy & Astrophysics, 616, A174, doi: 10.1051/0004-6361/201833047

Pierce, C. M., Lotz, J. M., Primack, J. R., et al. 2010, Monthly Notices of the Royal Astronomical Society, 405, 718, doi: 10.1111/j.1365-2966.2010.16502.x

Pimbblet, K. A., Shabala, S. S., Haines, C. P., Fraser-McKelvie, A., & Floyd, D. J. E. 2013, Monthly Notices of the Royal Astronomical Society, 429, 1827, doi: 10.1093/mnras/sts470

Popesso, P., & Biviano, A. 2006, Astronomy & Astrophysics, 460, L23, doi: 10.1051/0004-6361:20066269

Pouliasis, E., Georgantopoulos, I., Bonanos, A. Z., et al. 2019, Monthly Notices of the Royal Astronomical Society, 487, 4285, doi: 10.1093/mnras/stz1483

Pozzetti, L., Bolzonella, M., Zucca, E., et al. 2010, Astronomy & Astrophysics, 523, A13, doi: 10.1051/0004-6361/200913020

Ramasawmy, J., Stevens, J., Martin, G., & Geach, J. E. 2019, Monthly Notices of the Royal Astronomical Society, 486, 4320, doi: 10.1093/mnras/stz1093

Rees, M. J. 1984, Annual Review of Astronomy and Astrophysics, 22, 471, doi: 10.1146/annurev.aa.22.090184.002351

Rees, M. J., Silk, J. I., Werner, M. W., & Wickramasinghe, N. C. 1969, Nature, 223, 788, doi: 10.1038/223788a0

Rieke, G. H. 1978, The Astrophysical Journal, 226, 550, doi: 10.1086/156639

Rieke, G. H., & Lebofsky, M. J. 1981, The Astrophysical Journal, 250, 87, doi: 10.1086/159350

Rindler, W. 1956, Monthly Notices of the Royal Astronomical Society, 116, 662, doi: 10.1093/mnras/116.6.662

Rodríguez, I. M., Georgakakis, A., Shankar, F., et al. 2022, Cosmic evolution of the incidence of Active Galactic Nuclei in massive clusters: Simulations versus observations, arXiv, doi: 10.48550/arXiv.2211.00032

Rosario, D. J., Santini, P., Lutz, D., et al. 2013, The Astrophysical Journal, 771, 63, doi: 10.1088/0004-637X/771/1/63

Rosario, D. J., McIntosh, D. H., Wel, A. v. d., et al. 2015, Astronomy & Astrophysics, 573, A85, doi: 10.1051/0004-6361/201423782

Salpeter, E. E. 1964, The Astrophysical Journal, 140, 796, doi: 10.1086/147973

Sandage, A. 1961, The Hubble Atlas of Galaxies. https://ui.adsabs.harvard.edu/abs/1961hag..book.....S

Sanders, D. B., Phinney, E. S., Neugebauer, G., Soifer, B. T., & Matthews, K. 1989, The Astrophysical Journal, 347, 29, doi: 10.1086/168094

Schawinski, K., Thomas, D., Sarzi, M., et al. 2007, Monthly Notices of the Royal Astronomical Society, 382, 1415, doi: 10.1111/j.1365-2966.2007.12487.x

Schmidt, M. 1963, Nature, 197, 1040, doi: 10.1038/1971040a0

Schreiber, C., Pannella, M., Elbaz, D., et al. 2015, Astronomy & Astrophysics, 575, A74, doi: 10.1051/0004-6361/201425017

Schwarzschild, K. 1916, Abh. Konigl. Preuss. Akad. Wissenschaften Jahre 1906,92, Berlin,1907, 1916, 189. https://ui.adsabs.harvard.edu/abs/1916AbhKP1916..189S

—. 1999, On the gravitational field of a mass point according to Einstein's theory, arXiv, doi: 10.48550/arXiv.physics/9905030

Sersic, J. L. 1968, Atlas de Galaxias Australes. https://ui.adsabs.harvard.edu/abs/1968adga.book.....S

Seyfert, C. K. 1943, The Astrophysical Journal, 97, 28, doi: 10.1086/144488

Shi, Y., Rieke, G. H., Hines, D. C., et al. 2005, The Astrophysical Journal, 629, 88, doi: 10.1086/431344

Simpson, C., Westoby, P., Arumugam, V., et al. 2013, Monthly Notices of the Royal Astronomical Society, 433, 2647, doi: 10.1093/mnras/stt940

Slipher, V. M. 1913, Lowell Observatory Bulletin, 2, 56. https://ui.adsabs.harvard.edu/abs/1913LowOB...2...56S

Smith, H. J., & Hoffleit, D. 1963, Nature, 198, 650, doi: 10.1038/198650a0

Son, S., Kim, M., & Ho, L. C. 2022, The Astrophysical Journal, 927, 107, doi: 10.3847/1538-4357/ac4dfc

Steffen, A. T., Strateva, I., Brandt, W. N., et al. 2006, The Astronomical Journal, 131, 2826, doi: 10.1086/503627

Suh, H., Civano, F., Hasinger, G., et al. 2019, The Astrophysical Journal, 872, 168, doi: 10.3847/1538-4357/ab01fb

Sutherland, W., & Saunders, W. 1992, Monthly Notices of the Royal Astronomical Society, 259, 413, doi: 10.1093/mnras/259.3.413

Sánchez, P., Lira, P., Cartier, R., et al. 2017, The Astrophysical Journal, 849, 110, doi: 10.3847/1538-4357/aa9188

Tananbaum, H., Avni, Y., Branduardi, G., et al. 1979, The Astrophysical Journal, 234, L9, doi: 10.1086/183100

Taylor, E., Almaini, O., Merrifield, M., et al. 2023, Monthly Notices of the Royal Astronomical Society, 522, 2297, doi: 10.1093/mnras/stad1098

Trevese, D., Boutsia, K., Vagnetti, F., Cappellaro, E., & Puccetti, S. 2008, Astronomy & Astrophysics, 488, 73, doi: 10.1051/0004-6361:200809884

Uttley, P., Cackett, E. M., Fabian, A. C., Kara, E., & Wilkins, D. R. 2014, The Astronomy and Astrophysics Review, 22, 72, doi: 10.1007/s00159-014-0072-0

van der Wel, A., Bell, E. F., Häussler, B., et al. 2012, The Astrophysical Journal Supplement Series, 203, 24, doi: 10.1088/0067-0049/203/2/24

Volonteri, M., & Gnedin, N. Y. 2009, The Astrophysical Journal, 703, 2113, doi: 10.1088/0004-637X/703/2/2113

Webster, B. L., & Murdin, P. 1972, Nature, 235, 37, doi: 10.1038/235037a0

Williams, R. J., Quadri, R. F., Franx, M., Dokkum, P. v., & Labbé, I. 2009, The Astrophysical Journal, 691, 1879, doi: 10.1088/0004-637X/691/2/1879

Wuyts, S., Labbé, I., Franx, M., et al. 2007, The Astrophysical Journal, 655, 51, doi: 10.1086/509708

Zhong, Y., Inoue, A. K., Yamanaka, S., & Yamada, T. 2022, The Astrophysical Journal, 925, 157, doi: 10.3847/1538-4357/ac3edb

Zuo, W., Wu, X.-B., Liu, Y.-Q., & Jiao, C.-L. 2012, The Astrophysical Journal, 758, 104, doi: 10.1088/0004-637X/758/2/104